

1                   **Supplementary Materials for**

2  
3                   **"Warm afterglow from the Toarcian Oceanic Anoxic Event drives the success of**  
4                   **deep-adapted brachiopods"**

5  
6       Ullmann, C.V.\*, Boyle, R., Duarte, L.V., Hesselbo, S.P., Kasemann, S., Klein, T., Lenton, T.,  
7                   Piazza, V., Aberhan, M.

8  
9       \*c.v.ullmann@gmx.net

10  
11           **Contents:**

- 12           Geological background  
13           Analytical methods  
14           Assessment of fossil preservation  
15           Geochemical assessment of shell preservation  
16           Palaeoenvironmental significance of data  
17           Modelling  
18           SI References

19

20 **Geological background**

21 We studied the Toarcian succession of the NW Tethyan shelf at two representative  
22 localities in the surroundings of the Iberian Massif. These are the Barranco de la Cañada  
23 section ( $40^{\circ}23'53.4''N$   $1^{\circ}30'07.4''W$ ) near Albarracín in the Iberian Basin, Spain, and the  
24 composite sections of Fonte Coberta ( $40^{\circ}03'36.5''N$   $8^{\circ}27'33.4''W$ ) and Rabaçal  
25 ( $40^{\circ}03'08.0''N$   $8^{\circ}27'30.5''W$ ) near Coimbra in the Lusitanian Basin, Portugal<sup>1-4</sup>. Both  
26 sections are fossiliferous, with brachiopods and bivalves being the dominant  
27 macrobenthic groups, are well constrained biostratigraphically, and record fairly  
28 continuous sedimentation without any obvious hiatuses.

29 Barranco de la Cañada is located in the Iberian Range, a NW trending fold- and thrust-belt  
30 in east-central Spain that, in the early Mesozoic, represented a system of shallow marine  
31 platforms connected to other European epicontinental basins northward and the Tethyan  
32 Ocean in the southeast<sup>5</sup>. The Toarcian succession is represented by the Turmiel  
33 Formation which marks a progressive Toarcian deepening of the platform until the mid-  
34 Toarcian Bifrons Zone<sup>6,7</sup>. The ca. 27-m-thick sampled interval ranges from the  
35 Pliensbachian/Toarcian boundary to the lower Bifrons Zone (middle Toarcian) and is  
36 biostratigraphically constrained by ammonites, brachiopods, and foraminifers<sup>7,8</sup>. It  
37 consists of rhythmic alternations of limestones and marlstones. The partly argillaceous  
38 limestones primarily comprise wackestones, mudstones, and floatstones indicative of  
39 low-energy conditions. Only very few packstone and rudstone beds suggest brief  
40 episodes of higher water energy. Deposition took place in a mid-ramp setting mostly  
41 below storm wave base at an estimated water depth of 40–70 m<sup>7,9</sup>, with the occasional  
42 higher energy limestone variants being interpreted as distal storm flow beds<sup>10</sup>. In terms  
43 of sequence stratigraphy (summarized in Refs. 5,7,9,11) the studied interval is part of a  
44 second-order transgressive-regressive cycle (LJ-3 in Ref 5) ranging from the  
45 Pliensbachian Davoei Zone to the middle Toarcian Variabilis Zone. The transgressive  
46 phase occurred in three distinct pulses, of which the second (LJ3-2) and parts of the third  
47 (LJ3-3) cycle fall within the study interval. LJ3-2 starts in the early Tenuicostatum Zone  
48 with maximum flooding in the lower Semicelatum Subzone, whereas LJ3-3 starts in the  
49 lower Serpentinum Zone with maximum transgression in the Bifrons Zone<sup>5</sup>.

50 At Fonte Coberta/Rabaçal, Portugal, the ca. 28-m-thick studied succession from the  
51 Pliensbachian/Toarcian boundary (base of the Polymorphum Zone = Tenuicostatum  
52 Zone of the Submediterranean Province) to the middle of the Levisoni Zone (=

53 Serpentinum Zone) comprises three members of the São Gião Formation<sup>12,13</sup>.  
54 Biostratigraphic control is provided by ammonites (e.g. Refs. 13,14), nannofossils<sup>15</sup>, and  
55 dinoflagellates<sup>16</sup>. Similar to Barranco de la Cañada, the section is composed of an  
56 alternation of marlstones and partly argillaceous limestones (mudstones and  
57 wackestones). This hemipelagic sequence was deposited on a low-energy, middle to  
58 distal homoclinal ramp below storm wave base, at an estimated water depth of 80–120  
59 m<sup>5,17</sup>, i.e. in a slightly deeper water setting than the sediments at Barranco de la Cañada.  
60 In terms of sequence stratigraphy, the base of the Polymorphum Zone marks the basal  
61 Toarcian transgression, an isochronous event within the Lusitanian Basin<sup>18,19</sup>. The first  
62 lithological member (Marly limestones with *Leptaena* Fauna) is interpreted as a  
63 transgressive systems tract with low sedimentation rates. The second member (Thin  
64 nodular limestones Member) and the third member (Marls and marly limestones with  
65 *Hildaites* and *Hildoceras*) represent two phases of the same sequence, with the former  
66 being interpreted as low-stand systems tract related to tectonic activity<sup>20</sup> in the basin,  
67 and the latter as a transgressive systems tract. A somewhat different view was presented  
68 by Gahr (2005)<sup>9</sup>, who argued for three different depositional sequences instead of two,  
69 with the second member being at least partly related to the basal Toarcian transgression.  
70 A conspicuous feature of both sections is the absence of black shales which commonly  
71 characterize the Toarcian Oceanic Anoxic Event elsewhere (e.g., Refs. 21–24). In contrast,  
72 the total organic carbon content is generally low<sup>25,26</sup>, while body fossils and/or  
73 ichnofossils occur continuously throughout the sections<sup>4,7,27</sup>. Accordingly, the marine  
74 habitats at both localities were characterized by well oxygenated conditions throughout  
75 the early to middle Toarcian time interval<sup>4,7</sup>. Also the ichnofauna, while undergoing  
76 important changes, never vanishes entirely suggesting that bottom water oxygenation  
77 was never insufficient to sustain benthic life for extended periods of time<sup>3,28</sup>.

78

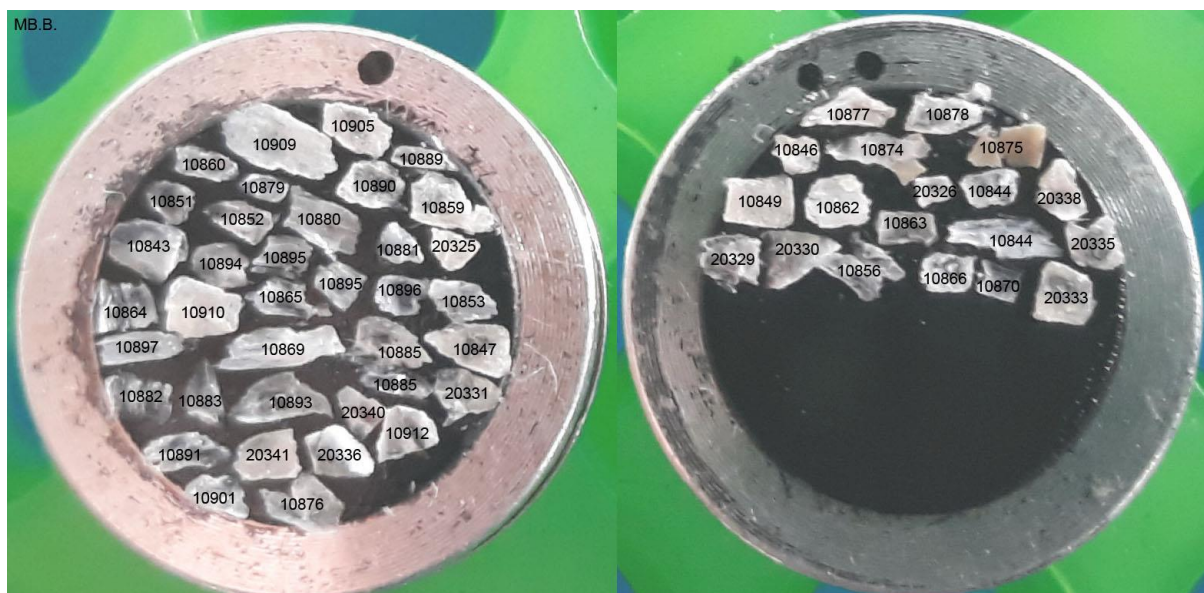
79 **Analytical methods**

80 Fossil specimens were collected from sedimentary strata in Barranco de la Cañada and  
81 Fonte Coberta/Rabaçal and identified to species level (**Table S1**). A subset of these fossils  
82 was selected for geochemical analysis

83

84 **Scanning Electron Microscope (SEM)**

85 Calcite splinters of ca 1 mm width were extracted from the fossils and placed on SEM  
86 stubs (**Figs S1,2**). The stub was carbon coated and SEM observations carried out under  
87 high vacuum. Images were taken using an FEI Quanta 650 Field Emission Gun Scanning  
88 Electron Microscope (FEG SEM) at the University of Exeter, Penryn Campus, Environment  
89 and Sustainability Institute at 15 kV and typical working distance between 10 and 11 mm.



90

91 **Figure S1:** SEM stubs with fossil fragments from Fonte Coberta / Rabaçal. Numbers correspond to  
92 collection numbers of the Museum für Naturkunde Berlin (Germany), see below. The diameter of the stubs  
93 is 12 mm.

94

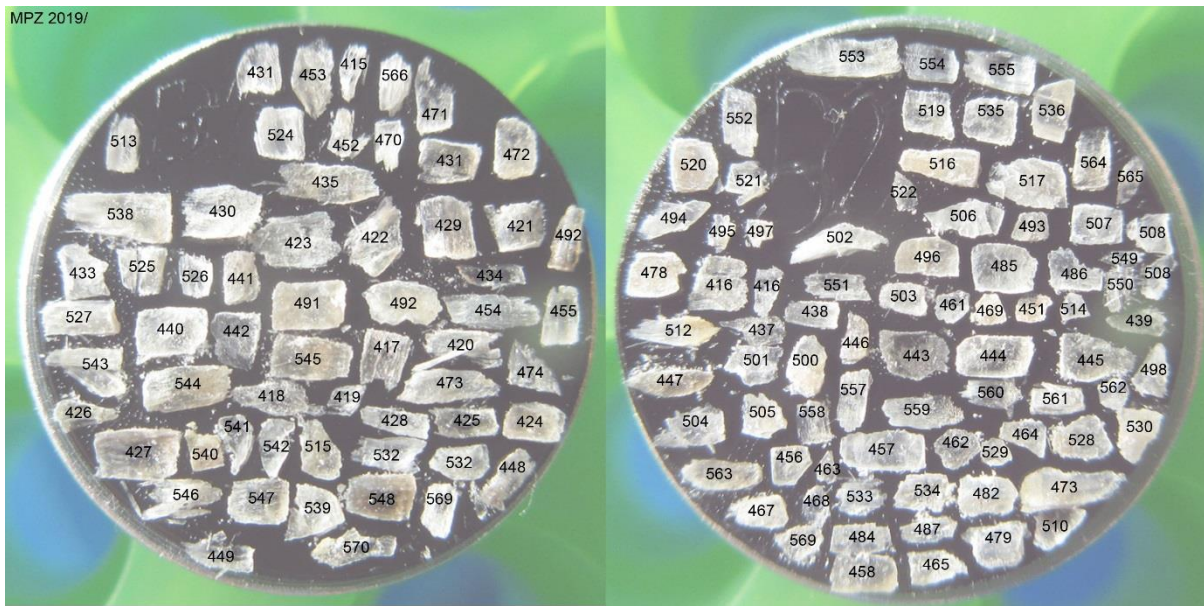


**Figure S2:** SEM stubs with fossil fragments from the Barranco de la Cañada section. Numbers correspond to collection numbers of the Museu de Ciencias Naturales, Zaragoza (Spain), see below. The diameter of the stubs is 12 mm.

95

96

97

98

99

## 100 **Fossil preparation**

101 Fossil material from Fonte Coberta / Rabaçal is archived at the Museum für Naturkunde,  
 102 Berlin, Germany (samples MB.B.10843-10912 for brachiopods and MB.B.20325-20346  
 103 for bivalves). Shell fragments from Barranco de la Cañada are stored at the Museu de  
 104 Ciencias Naturales, Zaragoza, Spain (samples MPZ 2019/415-571; Ref. 29).

105

106 For all fossil shells the surface was cleaned from sediments and altered rinds, and for  
 107 brachiopods the primary shell layer was removed if present using a preparation needle,  
 108 scalpel or hand-held drill with diamond coated drill bit. Visually best-preserved material  
 109 was targeted and specimens where only clearly altered shell material was present not  
 110 sampled. For most fossil specimens, shell material was extracted as sheaths of multiple  
 111 shell layers with a preparation needle. Where this was not possible due to the dense  
 112 nature of the material (mostly for some specimens of *Gryphaea*), samples were taken with  
 113 a scalpel or hand-held drill using a diamond coated drill bit of ca 1 mm diameter. Sample  
 114 sizes ranged from 0.9 to 14 mg (typically 1 – 3 mg) for fossils.

115 For each stratigraphic interval apart from levels C12 and BC22 for Barranco de la Cañada  
 116 and 22 horizons for Fonte Coberta / Rabaçal a sample of bulk rock was extracted with a  
 117 hand-held drill from the bulk rock matrix of a suitable fossil specimen. Sample sizes  
 118 ranged from 7 to 31 mg (typically 15 to 30 mg). Where present, sparitic calcite cements

119 filling or partially filling brachiopod fossils were sampled as well. Sample sizes ranged  
120 from 3 to 29 mg (typically 5 to 15 mg).

121 All 550 samples (4 belemnite samples, 130 bivalve samples, 359 brachiopod samples, 41  
122 bulk rock and 16 cement samples) for Barranco de la Cañada and 135 samples for Fonte  
123 Coberta / Rabaçal were collected and stored in 2 mL sample vials for later processing and  
124 archiving of surplus material for possible replicate measurements or future specialist  
125 analysis.

126

127 ***Element/Ca ratio determination***

128 A fraction of each sample amounting to 220 to 820 µg (typically 330 to 550 µg) was  
129 weighed into 15 mL centrifuge tubes using a Micro Balance at a precision of 1µg. The  
130 centrifuge tubes were then weighed at 10 µg precision using either a model semi-  
131 microbalance. 2% v/v nitric acid prepared from 18.2 MΩ water and 67% concentrated  
132 nitric acid was added from an FEP wash bottle to dissolve the fossil calcite at a ratio of ca  
133 15 mL per mg resulting in a dilution to ca 25 µg/g Ca. After dilution the tubes were  
134 weighed again with the same semi-microbalance to allow for the computation of precise  
135 dilution factors.

136 The samples were analysed for element/Ca ratios using an Agilent 5110 VDV Inductively  
137 Coupled Optical Emission Spectrometer (ICP-OES) with Seaspray U-series glass nebulizer  
138 and double pass cyclonic spray chamber. Sample and standard transfer was automated  
139 by an Agilent SPS4 autosampler.

140 Analysis was done in batches of 120 samples subdivided into blocks of 30 samples  
141 bracketed by calibrations and subdivided into sets of 10 samples by quality control  
142 solutions (BCQC & BCQ2) and international reference materials (JLs-1 limestone<sup>30</sup>; UN  
143 AK carbonate<sup>31</sup>). This protocol resulted in 5 calibrations, 12 analyses of JLs-1, 8 analyses  
144 of UN AK, and 4 analyses of BCQC or BCQ2 per batch of 120 samples.

145 Three synthetic calibration solutions were prepared from certified 1,000 µg/g single  
146 element plasma standards. A uniform Ca concentration of 25 µg/g was opted for to match  
147 the matrix of the fossil samples. For all other elements contents were variable to cover  
148 the expected range of element/Ca ratios. The calibration solutions were prepared  
149 gravimetrically by incremental addition of single element standards into a 1 L bottle and  
150 differential weighing using a Semi-microbalance with 10 µg precision up to a weight of  
151 120 g and 100 µg precision up to a weight of 230 g. The final weight of the calibration

152 solutions after filling up to 1 L with 25 v/v nitric acid was determined using an top loader  
153 balance with precision of 0.01 g. Comparability of the weighing results was ensured by  
154 weighing the empty bottles on either balance which gave indistinguishable results. For  
155 Ca concentrations a two-point calibration with calibration blank and three solutions of  
156 near equivalent Ca concentration resulted. For all other analytes, a linear four point  
157 calibration with a calibration blank and three calibration solutions with different  
158 concentrations was made. Covered calibration ranges are 0 to 33.4 mmol/mol for Mg/Ca,  
159 0 to 3.66 mmol/mol for Sr/Ca, 0 to 5.81 mmol/mol for Fe/Ca, 0 to 2.93 mmol/mol for  
160 Mn/Ca, 0 to 13.1 mmol/mol for P/Ca, and 0 to 12.7 mmol/mol for S/Ca ratios.  
161 Analysed wavelengths are 317.933 nm and 422.673 nm for Ca, 279.553 nm, 280.270 nm  
162 and 285.213 nm for Mg, 407.771 nm and 421.552 nm for Sr, 238.204 nm and 259.94 nm  
163 for Fe, 257.610 nm and 259.372 nm for Mn, 213.618 nm for P and 181.972 nm for S.  
164 Signals were quantified synchronously for all wavelengths in 12 blocks of 5s each  
165 resulting in signal integration over 60s per measurement. Optimum wavelengths for  
166 Mg/Ca and Sr/Ca results were chosen to maximize repeatability of the QC and standard  
167 solutions during data reduction. Results for both analysed wavelengths for Fe and Mn  
168 were pooled to improve signal to noise ratios.  
169 Typical quantification limits of the method measured as 6 standard deviations of the  
170 baseline variability are 2 ng/g for Ca, 0.3 ng/g for Mg, 0.02 ng/g for Sr, 0.5 ng/g for Fe, 0.2  
171 ng/g for Mn, 10 ng/g for P and 20 ng/g for S. Resulting effective quantification limits for  
172 element/Ca ratios in the carbonate are 0.02 mmol/mol for Mg/Ca, 0.4 µmol/mol For  
173 Sr/Ca, 0.02 mmol/mol for Fe/Ca, 0.006 mmol/mol for Mn/Ca, 0.5 mmol/mol for P/Ca and  
174 1 mmol/mol for S/Ca ratios.  
175 Reproducibility over six analytical sessions for Barranco de la Cañada was controlled by  
176 72 measurements of Jls-1, 48 measurements of UN AK and 24 measurements of BCQC.  
177 Over two analytical sessions for materials from Fonte Coberta / Rabaçal 24 aliquots of  
178 Jls-1, 16 aliquots of UN AK and 8 aliquots of BCQ2 were measured. Reproducibility  
179 depends on absolute analyte concentrations and is controlled by integration time when  
180 concentrations are low and random noise when concentrations are high. Consequently,  
181 element/Ca ratios which were higher than 100 times the quantification limit reproduced  
182 within 1 % (2 sd) for all reference materials. Largest 2 sd uncertainties for element/Ca  
183 ratios of reference materials where element/Ca ratios are below 100 times the  
184 quantification limit are 0.05 mmol/mol for Mg/Ca, 0.005 mmol/mol for Sr/Ca, 0.002

185 mmol/mol for Mn/Ca, 0.06 mmol/mol for Fe/Ca, 0.28 mmol/mol for S/Ca, and 0.17  
186 mmol/mol for P/Ca. Analytical results for all measured standard solutions are listed in  
187 **Table S2**.

188 Internal consistency of the measurements was ascertained by the quality control solution  
189 (BCQC and BCQ2) which was prepared in the same way as the calibration solutions but  
190 was not used for signal quantification. Relative bias of the analytical results for this  
191 quality control solution was smaller than 1 % for all analytes (**Table S2**).

192 Stock solutions for Jls-1 and UN AK were prepared from 0.5 L 1,000 µg/g stock solutions  
193 generated by the dissolution of ca 1.25 g of either of these standards using 2% v/v nitric  
194 acid. Due to minor non-carbonate fractions in both standards that were not dissolved in  
195 the nitric acid the results for some of the elements are therefore slightly biased. For the  
196 standards measured alongside samples from Barranco de la Cañada averages ( $\pm 2\text{sd}$ ) for  
197 Jls-1 ( $n = 72$ ) are Mg/Ca:  $15.37 \pm 0.07$ ; Sr/Ca:  $0.341 \pm 0.005$ ; Fe/Ca:  $0.14 \pm 0.01$   
198 mmol/mol; Mn/Ca:  $0.032 \pm 0.001$  mmol/mol; P/Ca:  $0.41 \pm 0.17$  mmol/mol; S/Ca:  $0.43 \pm$   
199  $0.22$  mmol/mol. Averages ( $\pm 2\text{sd}$ ) for UN AK ( $n = 48$ ) are Mg/Ca:  $2.47 \pm 0.02$  mmol/mol;  
200 Sr/Ca:  $3.01 \pm 0.01$  mmol/mol; Fe/Ca:  $1.11 \pm 0.06$  mmol/mol; Mn/Ca:  $0.043 \pm 0.001$   
201 mmol/mol; P/Ca:  $0.39 \pm 0.17$  mmol/mol; S/Ca:  $1.73 \pm 0.18$  mmol/mol.

202 Stock solutions for the samples from Fonte Coberta / Rabaçal were prepared from a  
203 differing standard batch and therefore give slightly differing results from the data  
204 obtained for Barranco de la Cañada. Averages ( $\pm 2\text{sd}$ ) for Jls-1 ( $n = 24$ ) are Mg/Ca:  $15.4$   
205  $\pm 0.1$ ; Sr/Ca:  $0.342 \pm 0.002$ ; Fe/Ca:  $0.155 \pm 0.004$  mmol/mol; Mn/Ca:  $0.032 \pm 0.002$   
206 mmol/mol; P/Ca:  $0.43 \pm 0.09$  mmol/mol; S/Ca:  $0.50 \pm 0.28$  mmol/mol. Averages ( $\pm 2\text{sd}$ )  
207 for UN AK ( $n = 16$ ) are Mg/Ca:  $2.64 \pm 0.05$  mmol/mol; Sr/Ca:  $3.04 \pm 0.02$  mmol/mol;  
208 Fe/Ca:  $1.366 \pm 0.007$  mmol/mol; Mn/Ca:  $0.045 \pm 0.002$  mmol/mol; P/Ca:  $0.40 \pm 0.15$   
209 mmol/mol; S/Ca:  $1.82 \pm 0.21$  mmol/mol.

210 Absolute Ca concentrations calculated for fossils reproduced to better than 0.6 wt% (2  
211 sd) for all brachiopod genera from Barranco de la Cañada for which at least 30 samples  
212 were taken (2 outliers). This variability is equivalent to an average of 5 to 8 µg sample  
213 material and is therefore thought to be mostly controlled by weighing imprecision of the  
214 micro balance and signal noise of the ICP-OES.

215 Possible external errors of element/Ca determinations and Ca concentrations relate to  
216 the uncertainty of element concentrations in certified 1,000 µg/g single element solutions  
217 taken for preparation of the calibration solutions. 95 % confidence intervals stated on the

218 certificates of analysis were 0.6 % of the analyte concentration or better for all studied  
219 elements.

220

221 ***C and O isotope ratio measurements***

222 685 samples were analysed for  $\delta^{13}\text{C}$  and  $\delta^{18}\text{O}$  values as well as carbonate content using a  
223 SerCon 20-22 Gas Source Isotope Ratio Mass Spectrometer (GS-IRMS) in continuous flow  
224 mode at the University of Exeter Penryn Campus, Environment and Sustainability  
225 Institute.

226 Typically 450 to 600  $\mu\text{g}$  of fossil material, bulk rock powder or calcite cement weighed to  
227 1  $\mu\text{g}$  precision in randomized order using a model Micro Balance and were transferred  
228 into 4.5 ml borosilicate Labco Exetainers®. Batches of 80 samples were analysed  
229 together with 22 aliquots of the in-house standard CAR (Carrara Marble,  $\delta^{13}\text{C} = +2.10 \text{ ‰}$   
230 V-PDB;  $\delta^{18}\text{O} = -2.03 \text{ ‰}$  V-PDB) and 8 aliquots of the in-house standard NCA (Namibia  
231 Carbonatite,  $\delta^{13}\text{C} = -5.63 \text{ ‰}$  V-PDB;  $\delta^{18}\text{O} = -21.90 \text{ ‰}$  V-PDB). These standards were  
232 previously calibrated against the international standards NBS-18, CO-8 and LSVEC as well  
233 as in-house standards of Freie Universität Berlin (CAM, Carrara Marble; LM, Laaser  
234 Marble) and University of Copenhagen (LEO, Carrara Marble). 450 to 550  $\mu\text{g}$  of carbonate  
235 powder weighed to 1  $\mu\text{g}$  precision were used for 17 aliquots of CAR and all aliquots of  
236 NCA in each batch. The remaining 5 aliquots of CAR ranged from ca. 200  $\mu\text{g}$  to ca. 1,000  
237  $\mu\text{g}$  and were used to define a calibration curve of sample weight versus signal yield, which  
238 is used to estimate carbonate concentrations of the bulk powders.

239 All samples were held at 70°C and flushed with He for 80 s before manual injection of c.  
240 100  $\mu\text{L}$  of nominally anhydrous phosphoric acid. Samples from Barranco de la Cañada  
241 were measured alternating with a reference gas which yielded typical peak areas of 201  
242 nAs for mass 44, equivalent to the signal from 551  $\mu\text{g}$  of calcite. Samples from Fonte  
243 Coberta / Rabaçal were analysed after replacement of the source filament of the 20-22  
244 GS-IRMS, change of Helium pressure control installations and CO<sub>2</sub> reference gas, resulting  
245 in slightly lower reference gas intensities of 192 nAs for mass 44, equivalent to the signal  
246 from 501  $\mu\text{g}$  of calcite. For samples from Barranco de la Cañada signal yield of the in-  
247 house reference NCA ( $n = 56$ ) was  $97.1 \pm 1.7 \text{ } (2 \text{ sd})$  versus the in-house reference CAR.  
248 For samples from Fonte Coberta / Rabaçal NCA ( $n = 24$ ) signal intensity was  $97.5 \pm 0.9 \text{ } \%$   
249 ( $2 \text{ sd}$ ) versus CAR. External errors of carbonate content estimations relate to the  
250 uncertainty of the carbonate content in CAR which was assumed to be pure CaCO<sub>3</sub> (44.0

251 wt% CO<sub>2</sub>). Minimal non-carbonate impurities, as well as minor adsorbed water on the  
252 powdered standard material could have biased the measurements.

253 Isotopic drift of the instrument reaching up to ca. 0.3 ‰ during an analytical session was  
254 controlled with both, the raw isotopic ratios of the reference gas and CAR and subtracted  
255 from the data using a polynomial fit to the raw data for CAR. Shift and compression of the  
256 isotopic scale were corrected using a two-point calibration of CAR and NCA. For Barranco  
257 de la Cañada samples, 2 sd repeatability of CAR (n = 125) was found to be 0.07 ‰ for δ<sup>13</sup>C  
258 and 0.15 ‰ for δ<sup>18</sup>O and 2 sd repeatability of NCA (n = 56) was 0.09 ‰ for δ<sup>13</sup>C and 0.35  
259 ‰ for δ<sup>18</sup>O. For Fonte Coberta / Rabaçal samples, 2 sd repeatability of CAR (n = 54) was  
260 found to be 0.06 ‰ for δ<sup>13</sup>C and 0.14 ‰ for δ<sup>18</sup>O and 2 sd repeatability of NCA (n = 24)  
261 was 0.08 ‰ for δ<sup>13</sup>C and 0.28 ‰ for δ<sup>18</sup>O.

262 All analytical result for isotopic and CaCO<sub>3</sub> concentration measurements of standard  
263 materials are listed in **Table S3**.

264

265 **Assessment of fossil preservation**

266 Excellent preservation of fossil material is a prerequisite for high fidelity  
267 palaeoenvironmental reconstructions using geochemical proxies from biogenic calcite.  
268 Brachiopods as well as oysters are widely studied<sup>32-34</sup> and their shell structure and  
269 geochemical patterns well understood so that diagenetic impacts on their calcite can be  
270 spotted confidently<sup>35</sup>. Additionally, the low magnesium calcite of rhynchonellid  
271 brachiopods and oysters is resistant against post-depositional recrystallization as  
272 compared to mineralized tissues of aragonitic or high magnesium calcite secreting  
273 organisms.

274 Reliable identification of diagenetically overprinted material using optical and chemical  
275 preservation parameters, however, is complicated. Optical assessment suffers from the  
276 fact that visual changes to the shell material are seldom uniform for an entire fossil and  
277 one can only qualitatively link optical signs of alteration to changes in chemical and  
278 isotopic parameters. Qualitative trends of diagenesis on geochemical parameters in fossil  
279 calcite are well-studied, but the local burial and exhumation history of outcropping  
280 sedimentary successions can be complicated and will define thresholds of chemical  
281 preservation markers.

282 To overcome these challenges, a comprehensive study of shell preservation employing  
283 optical (binocular microscope, SEM) and chemical (element/Ca ratios and C & O isotope  
284 ratios) techniques was employed. For Barranco de la Cañada, clearly diagenetic phases,  
285 in particular geopetal cements encountered in 15 brachiopods, as well as bulk rock  
286 samples were analysed for element/Ca and C & O isotope ratios alongside the fossil shells  
287 to control the geochemical composition of diagenetic endmembers. Geochemical patterns  
288 compatible with diagenesis observed in fossil calcite could then be matched with bulk  
289 and cement signals and suitable geochemical thresholds defining good shell preservation  
290 defined accordingly. For Fonte Coberta / Rabaçal, for which sparitic calcite was not  
291 observed in the studied specimens, only bulk rock data were used as proxy for diagenetic  
292 trends.

293

294 ***Optical assessment of shell structure preservation***

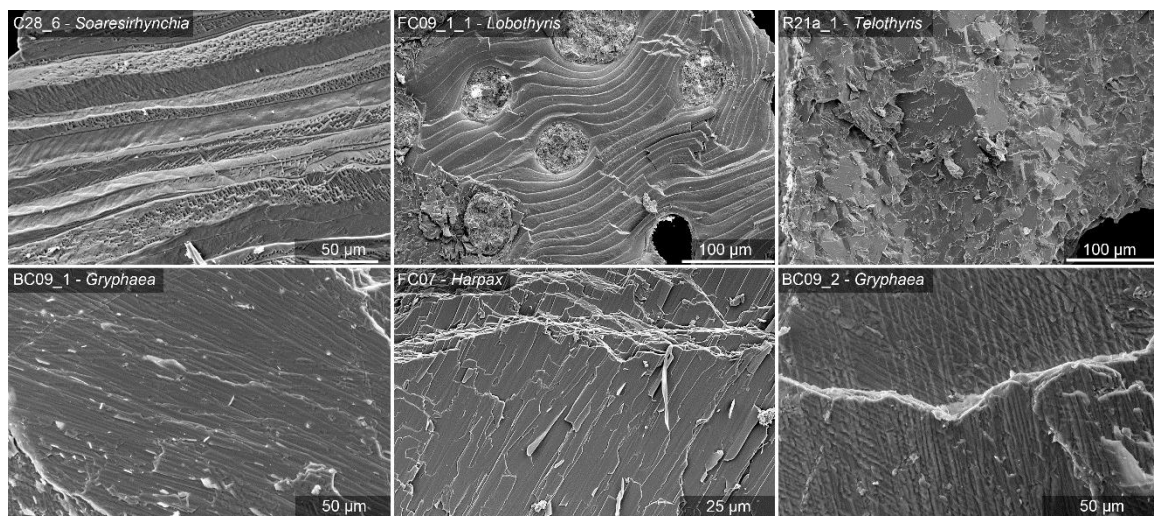
295 ***Rhynchonellid brachiopods***

296 Under the binocular microscope, secondary layer calcite of rhynchonellid brachiopods  
297 from Barranco de la Cañada looks exceptionally well preserved. The typical silky

298 reflection and slightly brownish semi-transparent colour attest to minimal  
299 recrystallization. Sample extraction with a preparation needle resulted in well-defined  
300 packages of multiples layers of shell fibres detaching along fibre surfaces, rather than  
301 disintegrated single fibres or calcite blocks with fracture surfaces oblique to the shell  
302 structures. Only on some specimens of *Soaresirhynchia* the coherence of the secondary  
303 layer calcite fibres was somewhat compromised and single fibres tended to detach from  
304 the shell and break into fragments of sugar-like appearance.

305 When observed under the SEM, many shell fibres of secondary layer calcite show  
306 surficial, pyramid shaped dissolution pits of less than 10 µm depth developed nearly  
307 exclusively on exposed surfaces of shell fibres (**Fig. S3**). These dissolution pits, where  
308 they are asymmetrical, show uniform orientation on single fibres. Morphologies and  
309 orientation of the pits change from fibre to fibre, indicating that the single-crystal  
310 character of the fibres is preserved and no pervasive re-crystallisation has taken place.  
311 Exposed surfaces of shell fibres are otherwise smooth and show no signs of fusing with  
312 adjacent fibres, and imprints of adjacent fibres as well as features of pressure solution  
313 and neomorphic calcite are absent. Terebratulid material with large cement-filled  
314 punctae as well as clearly recrystallized brachiopod calcite (**Fig. S3**) was not sampled for  
315 geochemical analysis.

316



317  
318 **Figure S3:** SEM secondary electron images of brachiopods and bivalves from the Barranco de la Cañada  
319 and Fonte Coberta / Rabaçal sections. Dissolution pits of a few micrometres depth in brachiopod shells as  
320 observed in *Soaresirhynchia* (top left) are common. Terebratulids with large, cement-filled punctae (top  
321 middle) and clearly recrystallized shell material (top right) were not processed for geochemical analyses.  
322 Shell ultrastructure preservation of bivalves (*Gryphaea*, bottom left; *Harpax*, bottom middle) is often very  
323 good. In many instances, however, imprints of surrounding shell fibres are observed (bottom right). Were  
324 these effects are pronounced, clear changes in element/Ca, C and O isotope ratios are observed (one sample

325 of *Gryphaea* specimen BC09\_2 had to be excluded from palaeoenvironmental interpretation). For  
326 stratigraphic position of imaged material, see **Table S4**.  
327

328 Brachiopod material from Fonte Coberta / Rabaçal showed the same morphological  
329 characteristics as specimens from Barranco de la Cañada. Overall, a larger fraction of  
330 specimens which were not further investigated for geochemical parameters due to  
331 spurious preservation observed already using a binocular microscope, showed  
332 diagenetic overprints, such as fusion of shell fibres and neomorphic calcite.

333 Overall, optical assessment of the shell calcite of specimens subjected to geochemical  
334 analyses did not suggest that the geochemical signatures in the material would be  
335 significantly compromised.  
336

### 337 Bivalves

338 *Gryphaea* shell material from Barranco de la Cañada appears less well preserved than  
339 brachiopod shells and a range of features indicative of diagenetic overprint were  
340 encountered during visual inspection with the binocular microscope. Fusion of shell  
341 layers and irregular surfaces indicative of incipient recrystallization, sometimes even loss  
342 of discernible shell structure were observed, but these features were seldom pervasive.  
343 Often, partially altered specimens still yielded patches of shell material with the typical  
344 stacks of thin, translucent sheaths of calcite layers that could be levered off the shell with  
345 a preparation needle. These visually best preserved areas were targeted for sampling for  
346 geochemical analysis.

347 SEM observations confirm that, compared to rhynchonellids, a larger fraction of *Gryphaea*  
348 calcite was affected by alteration. Dissolution pitting is almost absent, but neomorphic  
349 calcite is sometimes observed and surfaces of shell layers often bear the imprint of the  
350 overlying shell fibres, indicating earliest stages of fusing fibre sheaths as well as  
351 recrystallization (**Fig. S3**). Nevertheless, primary shell textures even on the micrometre  
352 scale are preserved in nearly all studied shell fragments, so that textural evidence  
353 suggests that geochemical preservation of the *Gryphaea* material should be good to very  
354 good.

355 Samples of the bivalve genus *Harpax* from Fonte Coberta / Rabaçal show ultrastructural  
356 features generally comparable to *Gryphaea* from Barranco de la Cañada (**Fig. S3**).  
357 However, as observed also for brachiopods, the preservation in general appears  
358 somewhat poorer than samples from Barranco de la Cañada as evidenced by more

359 pronounced fusion of shell layers. Consequently, data from *Harpax* are not further  
360 considered for palaeoenvironmental interpretation in this study.

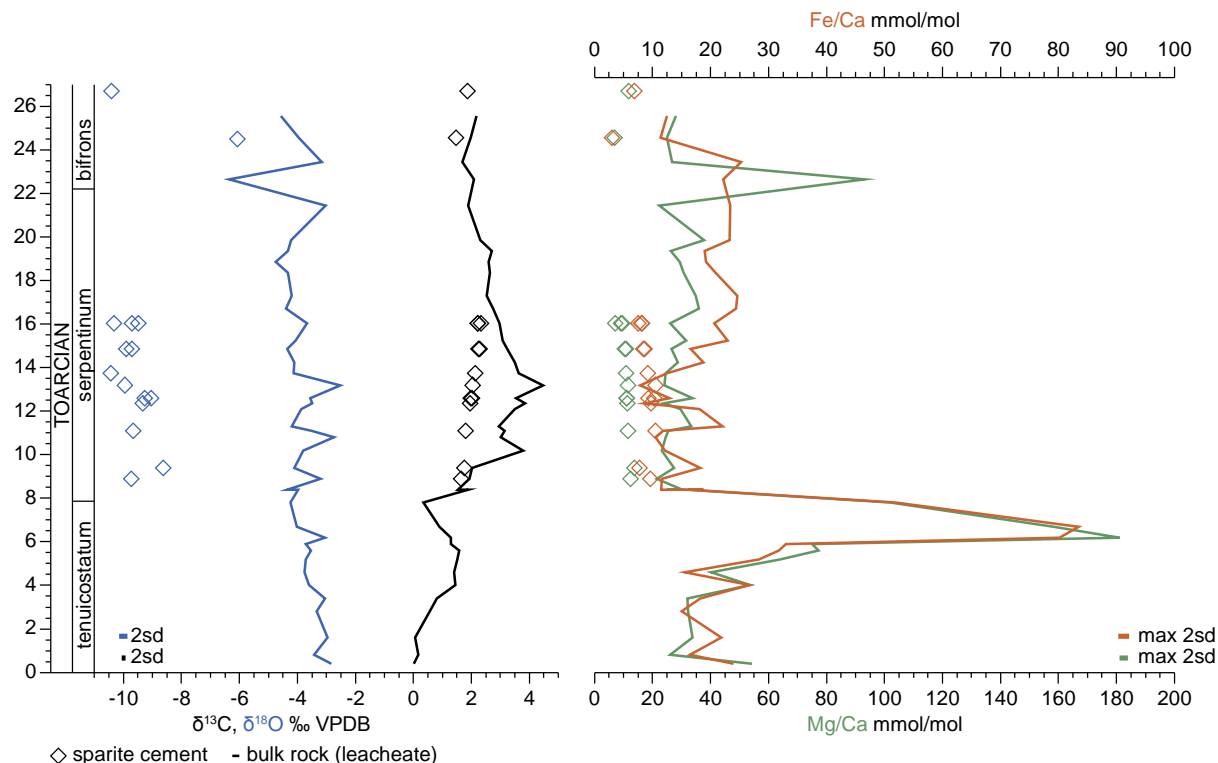
361

362 **Geochemical assessment of shell preservation**

363 **Bulk rock geochemistry Barranco de la Cañada**

364 The Toarcian sedimentary strata of the Barranco de la Cañada section from which fossils  
 365 were extracted are typically carbonate rich marls with carbonate contents of 46 to 94 %  
 366 (median 81 %, n = 42; **Table S4, Figure S4**) according to mass spectrometry results.  
 367 Carbonate contents below 70 % were only observed for four samples.

368



369

◇ sparite cement - bulk rock (leachate)

370 **Figure S4:**  $\delta^{13}\text{C}$  and  $\delta^{18}\text{O}$  values and Fe/Ca and Mg/Ca ratios of bulk rock and sparite cement samples from  
 371 the Barranco de la Cañada section.

372

373 ICP-OES measurements of the 42 bulk rock samples (**Table S4**) show that the majority of  
 374 the bulk rock matrix dissolved by the 2 v/v HNO<sub>3</sub> is low magnesium calcite with nine  
 375 measurements yielding Mg/Ca ratios greater than 50 mmol/mol. Besides sample BC18  
 376 (24.35m, top Serpentinitum Zone), Mg/Ca ratios greater than 50 mmol/mol are restricted  
 377 to the interval of samples C15 to C21+22/C25+26 (4.0 to 7.8 m, middle Tenuicostatum  
 378 Zone to basal Serpentinitum Zone). The rock leachates are relatively depleted in Sr with  
 379 Sr/Ca ranging from 0.26 to 0.71 mmol/mol (median 0.42 mmol/mol), but enriched in Mn  
 380 with Mn/Ca ratios of 0.34 to 1.07 (median 0.53 mmol/mol). Fe/Ca ratios are very high  
 381 and highly variable ranging from 7.9 to 83.4 mmol/mol (median 18.8 mmol/mol).

With respect to  $\delta^{13}\text{C}$  values, bulk rock carbonate shows a broadly similar pattern as brachiopod data (**Table S4**), but offset to lower values by 0.6 ‰ (median; range = -1.6 to +0.7 ‰).  $\delta^{18}\text{O}$  values of bulk carbonate (**Table S4**) do not follow the macrofossil pattern and become progressively more negative upsection, initially fluctuating around -3.0 ‰ V-PDB at the bottom of the section and reaching values around -4.5 ‰ V-PDB at the top. The median offset between fossil and bulk rock  $\delta^{18}\text{O}$  is -1.2 ‰ (range = -3.6 to +0.6 ‰). Assuming that diagenetic trends in the fossil carbonates led to an endmember similar to the bulk rock signature suggests that fossil calcite should be depleted in  $^{13}\text{C}$ ,  $^{18}\text{O}$  and Sr, and enriched in Mg, Mn and Fe. Due to the highly Fe-enriched nature of the rock matrix, biases on isotope ratios > 0.2 ‰ as well as biases on Sr/Ca ratios > 0.05 mmol/mol would be visible as enrichments in Fe/Ca well above 1 mmol/mol. Because of the comparatively high Mg/Ca ratios of the rock matrix, this threshold could potentially be associated with a bias in fossil Mg/Ca of 0.8 to 4.1 mmol/mol (median 1.7 mmol/mol).

395

### 396 ***Sparitic cements Barranco de la Cañada***

Geopetal cements incompletely filling voids in brachiopods are observed from samples C15+26/C28 to BC8 (8.9 to 18.05 m, basal to middle Serpentinum Zone) and samples BC20 and BC22 (26.25 and 28.4m, lower Bifrons Zone). Both intervals with geopetal cements start immediately above samples with bulk rock Mg/Ca > 50 mmol/mol (**Figure S4**). The cements (**Table S4**) in the Serpentinum zone show stratigraphic trends in Mg/Ca, covering a range from 7.2 to 13.7 mmol/mol and falling upsection as well as a well-defined increase in  $\delta^{13}\text{C}$  values from +1.6 to +2.3 ‰. Also, a weak downward trend in  $\delta^{18}\text{O}$  values which range from -8.6 to -10.4 ‰ is observed. Sr/Ca (0.22 to 0.44 mmol/mol), Mn/Ca (0.65 to 0.85 mmol/mol) and Fe/Ca (7.5 to 10.5 mmol/mol) are more stable than the hosting rock matrix and do not show clear stratigraphic trends. The sparite sample at level BC20 is geochemically distinct with particularly low Sr/Ca of 0.05 mmol/mol and low Mg/Ca of 3.0 mmol/mol, high Mn/Ca of 2.50 mmol/mol and less negative  $\delta^{18}\text{O}$  value of -6.1 ‰. Otherwise, however, the sparite samples of the Bifrons Zone are geochemically comparable to their counterparts in the Serpentinum Zone. The strong depletion in  $^{18}\text{O}$  as compared to the bulk carbonate suggests that the sparitic cements formed much later in the diagenetic sequence, either at elevated temperatures during burial or – more likely – involving meteoric fluids. Fluid migration may have been governed by lithology-controlled permeability as suggested by the high Mg/Ca ratios in

415 bulk rock leachates directly underlying both intervals of sparite occurrence. No  
416 geochemical links between sparite and surrounding rock matrix can otherwise be  
417 established suggesting limited effects of this void filling stage on geochemistry of  
418 carbonates in the section.

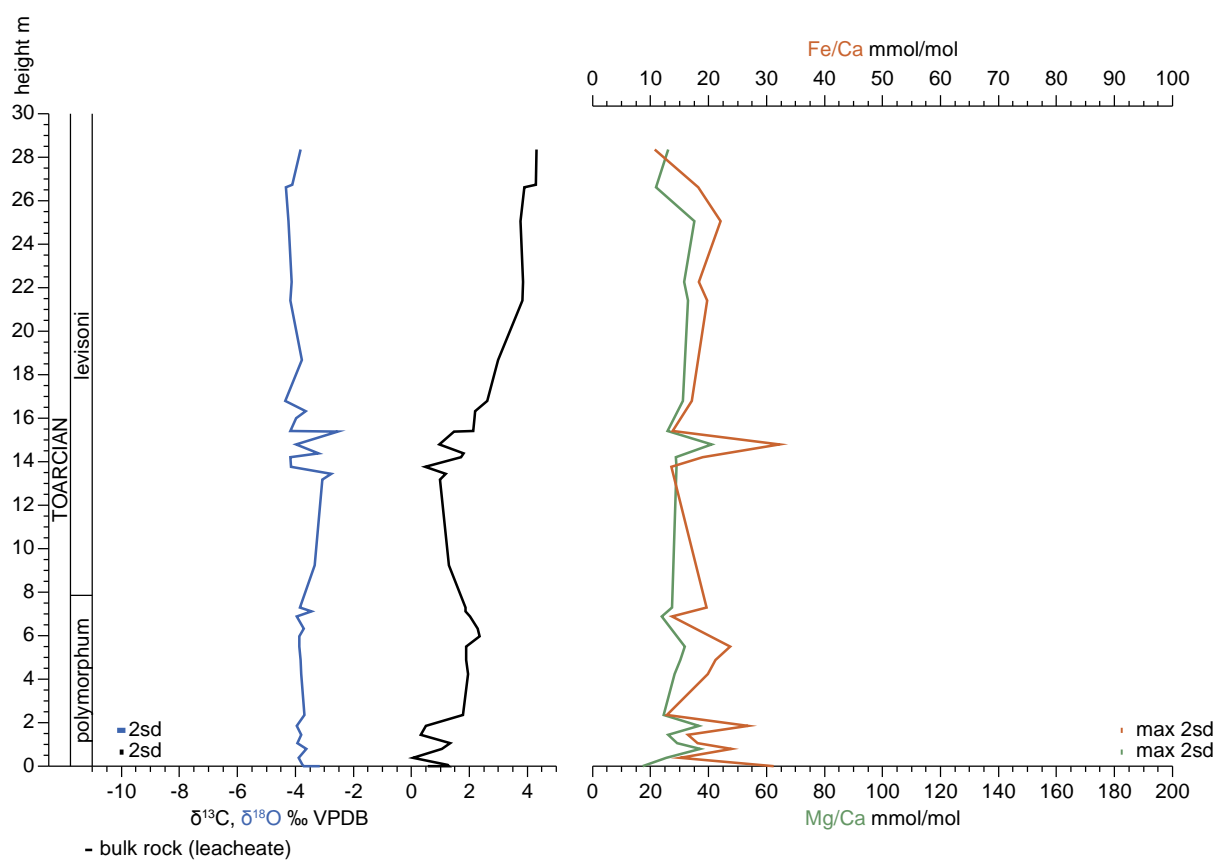
419 Partial isotopic overprint of fossil shell material approaching sparite-like  $\delta^{18}\text{O}$  values  
420 would be a clear concern. No strong correlations of  $\delta^{18}\text{O}$  values with Fe/Ca ratios with  
421 slopes (approximately 0.7 ‰ per mmol/mol) suggestive of such an alteration trend are  
422 observed in fossil material from levels where sparite is present, however. A measureable  
423 effect of sparite calcite on fossil geochemistry is therefore excluded.

424

#### 425 **Bulk rock geochemistry Fonte Coberta / Rabaçal**

426 Toarcian samples from the Fonte Coberta / Rabaçal section from which fossils were  
427 extracted are similar to those of the Barranco de la Cañada section (**Table S4, Figure S5**).  
428 The samples are carbonate rich marls with carbonate contents of 47 to 89 % (median 71  
429 ‰, n = 22) according to mass spectrometry results.

430



431

432 **Figure S5:**  $\delta^{13}\text{C}$  and  $\delta^{18}\text{O}$  values and Fe/Ca and Mg/Ca ratios of bulk rock samples from the Fonte Coberta  
433 / Rabaçal section.

434 ICP-OES measurements of the 22 bulk rock samples (**Table S4**, **Figure S5**) show that the  
435 bulk rock matrix dissolved by the 2 v/v HNO<sub>3</sub> is consistently low magnesium calcite with  
436 maximum Mg/Ca ratios reaching 41 mmol/mol in the lower *polymorphum* Zone. The rock  
437 leachates are generally slightly less Sr depleted than samples from Barranco de la Cañada  
438 with values ranging from 0.37 to 0.91 mmol/mol (median 0.55 mmol/mol). Mn/Ca ratios  
439 are comparable to Barranco de la Cañada with an observed range from 0.34 to 0.86 mmol  
440 (median 0.47 mmol/mol). As in Barranco de la Cañada Fe/Ca ratios are also high, but  
441 spikes coinciding with strong Mg enrichments are missing. Ratios of 10.8 to 32.2  
442 mmol/mol (median 18.7 mmol/mol) are found.

443 Also C and O isotope trends in the Fonte Coberta / Rabaçal section are similar to those of  
444 Barranco de la Cañada (**Table S4**, **Figs. S4,5**). Bulk rock δ<sup>13</sup>C values are typically 1 to 2  
445 ‰ less positive than brachiopod samples from the same horizon and show a pattern  
446 comparable to the brachiopod data. Conversely, δ<sup>18</sup>O values become progressively  
447 depleted in <sup>18</sup>O upsection with median values of -3.8 ‰ in the *polymorphum* Zone and -  
448 4.2 ‰ in the *levisoni* Zone.

449 The geochemical signatures in the Fonte Coberta / Rabaçal section suggest that chemical  
450 cut offs for fossil preservation similar to material from Barranco de la Cañada can be  
451 applied.

452

#### 453 ***Covariation of geochemical proxies in fossil materials indicative of alteration***

##### 454 *Barranco de la Cañada*

455 The fact that isotopic trends observed in the rhynchonellid brachiopods and *Gryphaea*  
456 are distinct from bulk rock matrix and sparitic cements (**Table S4**) indicates that  
457 preservation of palaeoenvironmental information in the fossil calcite may be good. Subtle  
458 biases relating to partial recrystallization or addition of cements may nevertheless bias  
459 the proxy data and need to be assessed by detailed investigation of co-variations of  
460 geochemical indicators of diagenesis.

461 Co-variation of Fe/Ca ratios as the most sensitive proxy for alteration at the Barranco de  
462 la Cañada section in *Gryphaea* (n = 130) is only strong with Mn/Ca ( $r^2 = 0.62$ , p < 0.001)  
463 and Mg/Ca ( $r^2 = 0.88$ , p < 0.001). For the remaining element/Ca ratios the correlation  
464 coefficients are 0.26 or lower and for C & O isotope ratios, they are 0.06 or lower,  
465 signifying that the vast majority of signal is not controlled by processes adding iron to the  
466 calcite postdepositionally. When excluding all samples with Fe/Ca ratios > 1mmol/mol,

467 the correlation coefficient of Fe/Ca with Mg/Ca reduces to 0.04 and all samples with  
468 Mg/Ca ratios > 6 mmol/mol are excluded from the dataset. An Fe/Ca threshold of 1  
469 mmol/mol for good fossil preservation as deduced also from comparison to bulk rock  
470 geochemistry is therefore deemed suitable for *Gryphaea*.

471 For rhynchonellid brachiopods ( $n = 359$ ), only the co-variation of Fe/Ca ratios with  
472 Mn/Ca ratios is strong with a correlation coefficient of  $r^2 = 0.70$ . For all other correlations,  
473 the correlation coefficient is 0.18 (Sr/Ca) or lower. Considering that the studied dataset  
474 encompasses major, global geochemical perturbations, geochemical co-variation in  
475 single stratigraphic intervals specific to brachiopod genera was also tested. Only intervals  
476 where data density was deemed high enough to produce reliable results (10 specimens  
477 of a single genus or more) were tested. As expected, for these subsets correlation  
478 coefficients of Fe/Ca with Mn/Ca were partially much higher than the entire dataset.  
479 However, in addition to this no clear pattern consistent with diagenetic trends (loss of Sr  
480 as depletion in  $^{13}\text{C}$  and  $^{18}\text{O}$  in parallel with gains in Mg, Mn and Fe) could be identified.  
481 In summary, it was concluded that minor diagenetic overprint of the material must have  
482 taken place as is evidenced by the enrichment of the shell calcite in Mn and Fe. These two  
483 elements are highly sensitive to partial diagenetic re-equilibration in the Barranco de la  
484 Cañada section, so that preservation of other geochemical proxies can robustly be  
485 controlled with Mn/Ca ratios and Fe/Ca ratios. In order to exclude altered material  
486 effectively, common limits of good preservation of 0.1 mmol/mol for Mn/Ca and 1.0  
487 mmol/mol for Fe/Ca ratios were adopted. These limits led to the exclusion of 34 of 359  
488 (9 %) brachiopod samples and 26 of 130 (20 %) *Gryphaea* samples. The larger fraction of  
489 excluded *Gryphaea* samples corroborates the optical assessment of the shell preservation  
490 that pointed at better preservation of brachiopod material. The number of excluded  
491 samples as compared to other studies on Mesozoic benthic organisms is small, however,  
492 further evidencing the overall excellent preservation of the shell material.

493

#### 494 *Fonte Coberta / Rabaçal*

495 The isotopic ratios of fossil shell materials in the Fonte Coberta / Rabaçal section are  
496 distinct from the bulk rock signal, suggesting that primary information is retained in their  
497 calcite. Strong fluctuations in particular in  $\delta^{13}\text{C}$  values relating to known environmental  
498 perturbations preclude the use of simple cross-plots of diagenesis proxies with isotope  
499 ratios to identify clearly overprinted samples. Comparison of geochemical signals within

500 single stratigraphic horizons suggests that isotopic proxies are insensitive to diagenetic  
501 overprint until Mn/Ca ratios of 0.05 and/or Fe/Ca ratios of 0.5 mmol/mol are reached.  
502 For example, samples of one individual of the genus *Cirpa* at 1.45 m height have  $\delta^{13}\text{C}$   
503 values of +3.0 to +3.3 ‰ and  $\delta^{18}\text{O}$  values of -1.1 to -1.2 ‰ apart from a single sample  
504 with  $\delta^{13}\text{C}$  value of +2.6 ‰ and  $\delta^{18}\text{O}$  values of -2.3 ‰ where Mn/Ca is 0.050 and Fe/Ca is  
505 0.57 mmol/mol. Because all but two of the fourteen samples taken from the bivalve  
506 *Harpax* cross the above preservation limits we only consider brachiopod data from Fonte  
507 Coberta / Rabaçal for palaeoenvironmental reconstruction.

508

509 **Palaeoenvironmental significance of data**

510 The reconstruction of palaeoenvironmental conditions on the basis of geochemical data  
511 requires that robust transfer functions exist for the studied parameters. In biogenic  
512 calcite geochemical signatures can be biased even in well-preserved materials by the  
513 presence of disequilibrium effects, generally known as “vital effects”<sup>36,37</sup>. Such effects  
514 associated with biological factors usually lead to the preferential incorporation of <sup>12</sup>C and  
515 <sup>16</sup>O into shell calcite and also compromise proxies based on element concentrations.

516 A pragmatic approach to minimise these challenges is to opt for fossil substrates that are  
517 thought to be least prone to vital effects. The calcite of the secondary shell layer in  
518 rhynchonellid brachiopods has been identified as a highly reliable substrate for  
519 geochemical proxies, especially when avoiding sampling from the shell hinge and  
520 specialized shell regions<sup>38</sup>. Similarly, the foliate calcite of modern oysters has been found  
521 to record environmental parameters with high fidelity<sup>34</sup>. From this point of view the fossil  
522 material chosen for study here is of the highest possible quality for investigating Early  
523 Jurassic palaeoenvironmental conditions.

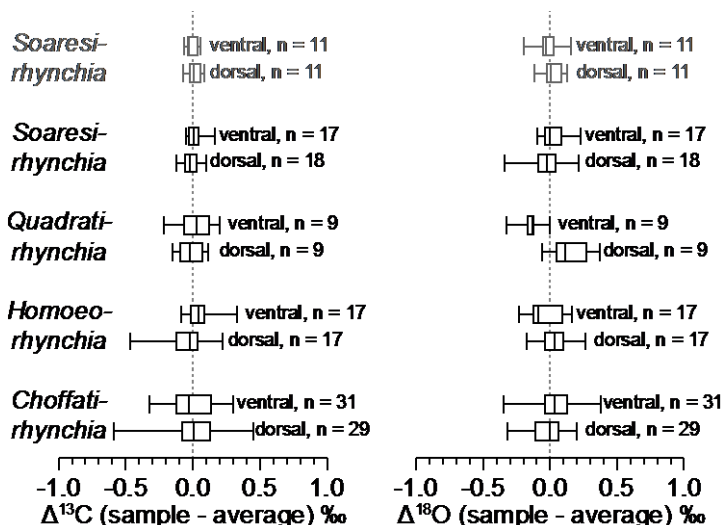
524 In order to further boost confidence in the reliability of the proxy data, potential biases  
525 relating to the chosen brachiopod genus and potential inter-specimen and intra-  
526 specimen differences, e.g. potential offsets between ventral and dorsal valves were  
527 assessed. Furthermore, isotopic data for brachiopods were compared to *Gryphaea* data  
528 to assess biases between these fossil groups.

529

530 **Intraspecimen variability of geochemical proxies**

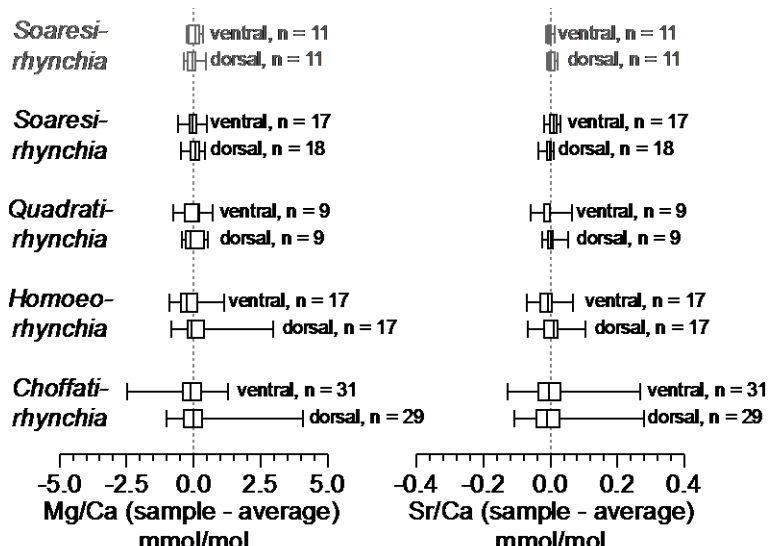
531 Geochemical compositions of ventral and dorsal valve of brachiopod specimens were  
532 only compared for genera for which at least three individuals with four samples that  
533 passed preservation criteria were available. This was the case for *Choffatirhynchia*,  
534 *Homoeorhynchia*, *Quadratirhynchia* and *Soaresirhynchia* from the Barranco de la Cañada  
535 section and *Soaresirhynchia* from the Fonte Coberta / Rabaçal section ([Fig. S6](#)).  
536 *Soaresirhynchia* specimens from the two sections were considered separately in case  
537 environmental conditions exerted a measurable control on shell geochemical proxies. For  
538 tested genera, differences in average isotope ratios range are generally negligible. Only  
539  $\delta^{18}\text{O}$  values in *Quadratirhynchia* show a minor offset of 0.2 ‰ in median values. This  
540 difference is based on nine measurements per valve only, however, and is not deemed to  
541 be large enough to warrant further consideration. The overall excellent correspondence

542 of isotopic signatures among dorsal and ventral valves of brachiopods instead is taken as  
 543 evidence that sampling spot on the specimen does not exert a bias on the isotopic data.  
 544



545 **Figure S6:** Whisker plot of differences of  $\delta^{13}\text{C}$  and  $\delta^{18}\text{O}$  values from specimen average depending on  
 546 sampled valve. Whiskers indicate the entire observed range and boxes the second and third quartile with  
 547 median. Only genera for which at least three specimens with four or more well-preserved samples were  
 548 available are presented. Isotopic differences relating to the sampled valve are generally negligible. The  
 549 dataset for *Soaresirhynchia* is split into specimens from Portugal (grey) and Spain (black).  
 550

551 Also average differences in Mg/Ca and Sr/Ca are minor with a maximum difference of  
 552 median Mg/Ca of 0.3 mmol/mol and maximum difference of median Sr/Ca of 0.02  
 553 mmol/mol in *Quadratirhynchia* (Fig. S7). Consequently, no biases related to the valve  
 554 chosen for sampling need to be considered.



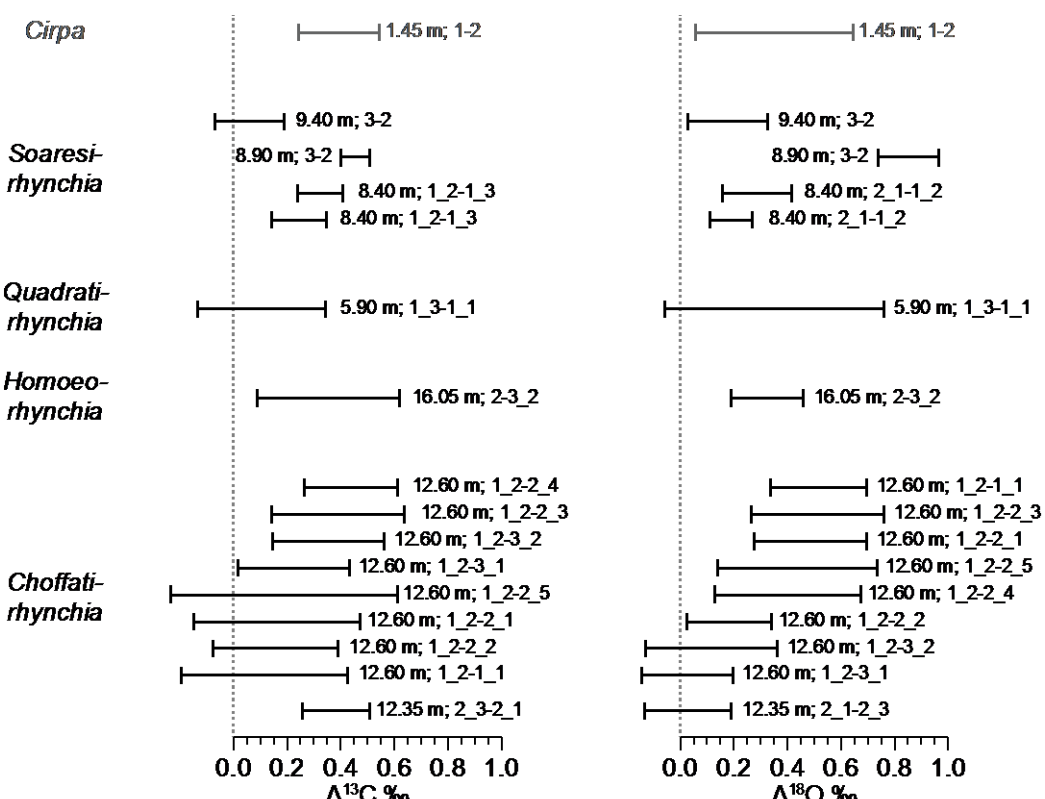
555 **Figure S7:** Whisker plot of differences of Mg/Ca and Sr/Ca ratios from specimen average depending on  
 556 sampled valve. Whiskers indicate the entire observed range and boxes the second and third quartile with  
 557 median. Only genera for which at least three specimens with four or more well-preserved samples were  
 558 available are presented. Differences relating to the sampled valve are generally negligible. The dataset for  
 559 *Soaresirhynchia* is split into specimens from Portugal (grey) and Spain (black).

560 The median isotopic variability within individuals of the various species has been  
 561 computed from specimens for which at least four samples which were deemed well-  
 562 preserved were available (**Table S5**). Median 2 sd isotopic variability is always smaller  
 563 than 0.5 ‰ for both isotopic systems, but substantially larger in *Choffatirhynchia*,  
 564 *Gibbirhynchia*, *Homoeorhynchia* and *Quadratirhynchia* than in *Cirpa*, *Nannirhynchia* and  
 565 *Soaresirhynchia*.

566

### 567 **Differences between fossils from the same stratigraphic level**

568 Differences in geochemical proxies between individual brachiopod fossils were assessed  
 569 for stratigraphic intervals for which at least two fossils yielding four well-preserved  
 570 samples each were available. This is the case for *Choffatirhynchia*, *Homoeorhynchia*,  
 571 *Quadratirhynchia* and *Soaresirhynchia* from Barranco de la Cañada and *Cirpa* from Fonte  
 572 Coberta / Rabaçal. For most of the resulting fossil couples significant (95 % confidence)  
 573 differences between average  $\delta^{13}\text{C}$  values (10 of 16) and  $\delta^{18}\text{O}$  values (12 of 16) were  
 574 observed (**Fig. S8**).



575 **Figure S8:** Isotopic differences between fossils from the same stratigraphic horizon. Error bars indicate 95  
 576 % confidence interval for the difference in average values. Where more than two specimens from a horizon  
 577 are available, all are compared to the most  $^{13}\text{C}$  and  $^{18}\text{O}$  enriched specimen respectively.  
 578

579 Isotopic differences greater than 0.5 ‰ between different specimens, however, were not  
580 observed for  $\delta^{13}\text{C}$  values and only in three instances for  $\delta^{18}\text{O}$  values (0.51, 0.52, and 0.85  
581 ‰). While stratigraphic horizons for which only one specimen or few specimens are  
582 available the computed isotopic averages are therefore less certain than were ample  
583 sample material was at hand, uncertainties relating from inter-specimen differences are  
584 not major.

585

#### 586 ***Interspecific offsets amongst brachiopods***

587 For most stratigraphic levels only one brachiopod genus was studied, but data for  
588 specimens of two brachiopod genera with four samples each are available for sample  
589 horizons BC3 (13.2 m; *Choffatirhynchia*, *Homoeorhynchia*) and BC4 (13.75 m;  
590 *Gibbirhynchia*; *Homoeorhynchia*) at Barranco de la Cañada. Differences in carbon (0.54  
591 ‰; 0.34 ‰) and oxygen (0.49 ‰; 0.14 ‰) isotope ratios between these genera is  
592 comparable to that of individuals of the same genus attesting to the reliability of the  
593 measured isotope ratios.

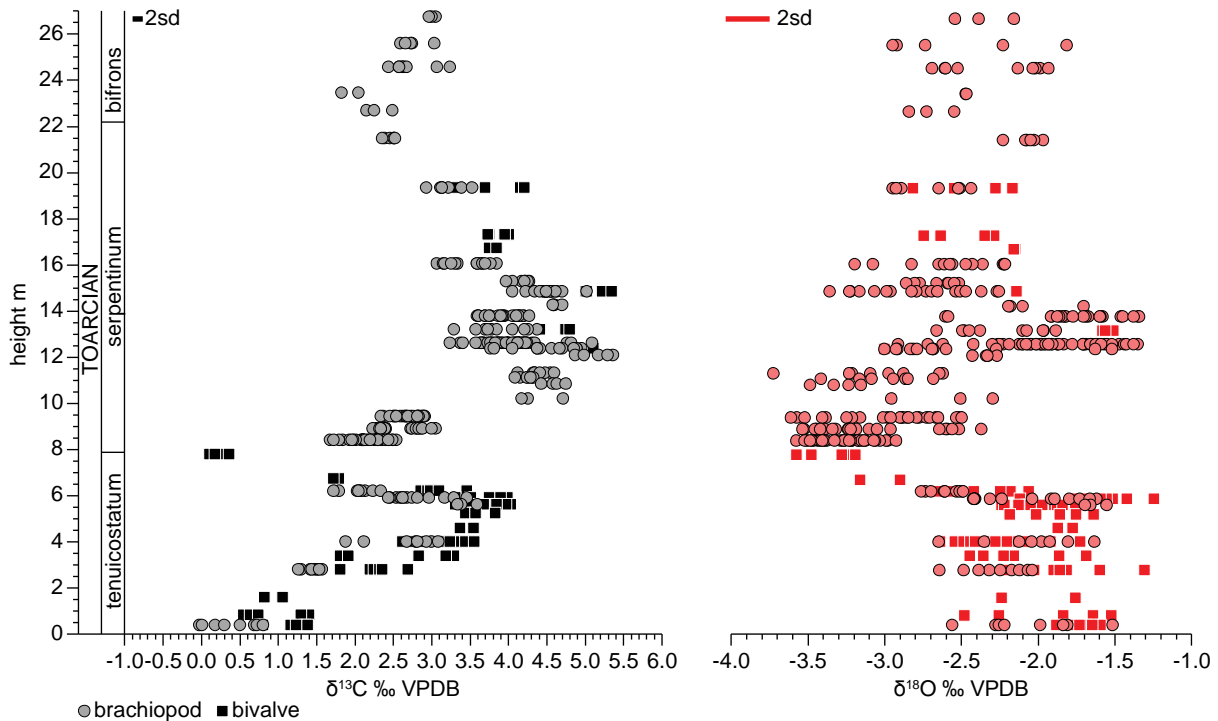
594 Regarding their chemical composition, the studied rhynchonellid taxa fall into two  
595 distinct groups (**Table S6**). The species with comparatively larger isotopic variability  
596 (*Choffatirhynchia*, *Gibbirhynchia*, *Homoeorhynchia* and *Quadratirhynchia*) are  
597 characterised by comparatively low calcite contents of 97.6 to 99.1 % versus the in-house  
598 marble standard CAR and comparatively high Mg/Ca (4.8 to 6.6 mmol/mol) and Sr/Ca  
599 (0.95 to 1.14 mmol/mol) ratios. Species with low isotopic variability (*Cirpa*,  
600 *Nannirhynchia*, *Soaresirhynchia*) on the other hand have high calcite content of 99.9 to  
601 100.3 % versus the in-house standard CAR and low Mg/Ca (1.9 to 2.6 mmol/mol) and  
602 Sr/Ca (0.51 to 0.54 mmol/mol) ratios.

603

#### 604 ***Isotopic difference between rhynchonellids and Gryphaea***

605 When comparing isotope ratios of brachiopods and bivalves from the Barranco de la  
606 Cañada section, a clear tendency of  $\delta^{13}\text{C}$  values from *Gryphaea* to be more positive than  
607 brachiopods from the same horizon is observed (**Figure S9**).

608



609

610 **Figure S9:** Carbon and oxygen isotope ratios for all individual samples from the Barranco de la Cañada  
611 section that passed screening for diagenesis.

612

613 For ten stratigraphic levels, samples for both, brachiopods and *Gryphaea*, were analysed.  
614 Comparison of the two datasets including overlaps with all rhynchonellids apart from  
615 *Soaresirhynchia* revealed a consistent offset of *Gryphaea* data towards more positive  $\delta^{13}\text{C}$   
616 values (+0.25 to +1.00 ‰), with a weighted average of +0.63 ‰. *Gryphaea* data were also  
617 found to be minimally enriched in  $^{18}\text{O}$  (-0.43 to +0.70 ‰) with a weighted average of  
618 +0.10 ‰.

619 Independent studies reporting carbon and oxygen isotope ratios for coeval Early Jurassic  
620 brachiopods and *Gryphaea* are currently unavailable. The framework for understanding  
621 C & O isotope data from rhynchonellid brachiopods is very well established, their average  
622 shell preservation is superior to that of *Gryphaea* in the Barranco de la Cañada section,  
623 and rhynchonellids contribute more than 75 % of the data of the screened dataset.  
624 Furthermore, the dataset from Fonte Coberta / Rabaçal is based solely on brachiopod  
625 samples. It was therefore decided to shift all *Gryphaea*  $\delta^{13}\text{C}$  values by -0.63 ‰ to generate  
626 a coherent dataset. The question remains how this recalculated dataset exactly matches  
627 to absolute atmospheric carbon isotope ratios during the Toarcian stage, but the  
628 correction procedure allows for relative changes in  $\delta^{13}\text{C}$  values to be studied with  
629 confidence.  $\delta^{18}\text{O}$  values of the *Gryphaea* samples were not adjusted, because the observed  
630 difference between the two fossil types of 0.10 ‰ was deemed negligible.

631

632 ***Calculation of palaeo seawater temperatures***

633 A palaeothermometer based on oxygen isotope ratios and supplemented by MgCO<sub>3</sub>  
634 concentrations has been developed using modern analogues<sup>32</sup>. We adopt this  
635 thermometer as the currently most sophisticated thermometer available for brachiopods  
636 and use it also for the *Gryphaea* data owing to the good agreement of the brachiopod and  
637 bivalve datasets. The equation presented by Brand et al. (2013)<sup>32</sup> requires an input of  
638 seawater δ<sup>18</sup>O and mol% MgCO<sub>3</sub> in the shell calcite. Due to the lack of robust knowledge  
639 of seawater δ<sup>18</sup>O we use here the value of -1 ‰ vs V-SMOW and also list  
640 palaeotemperature data derived from the equation by Anderson and Arthur (1983)<sup>39</sup> to  
641 enable maximum comparability to palaeotemperature data of Suan et al., (2008)<sup>33</sup>. The  
642 fractionation factor for oxygen isotopes between calcite and water is also to some degree  
643 influenced by the magnesium concentration of the secreted calcite<sup>40</sup>. The magnitude of  
644 this effect is approximately 0.17 ‰ per mol% MgCO<sub>3</sub>. The resulting MgCO<sub>3</sub> effect on the  
645 fractionation factor is very small (0.07 ‰ on average) due to the very low MgCO<sub>3</sub> content  
646 of the shell materials averaging 0.4 mol% MgCO<sub>3</sub>. Because of the narrow range of MgCO<sub>3</sub>  
647 concentrations in the studied shell materials palaeotemperatures are calculated for  
648 aggregated data rather than for each sample individually. The resulting potential biases  
649 are negligible, e.g., 0.07 ‰ and 0.24 °C or less between the different taxa.

650 Average palaeotemperatures for the Barranco de la Cañada section derived from Refs. 32  
651 and 39 together with average carbon and oxygen isotope ratios and ages based on the  
652 Geologic Timescale 2012<sup>41</sup> are listed in **Table S7**.

653

654 **Modelling**

655 ***Simple mass balance calculations***

656 The datapoints are separated by time intervals in the region of 0.05-0.1 Myrs, shorter than  
657 the ~100 kyr residence time of oceanic carbon<sup>42</sup> and longer than the c. 1,000 year mixing  
658 time of the ocean. Over such timescales we can make rough estimates of how much  
659 carbon is needed to drive the perturbation using simple mass-balance calculations<sup>43</sup>. We  
660 write the initial isotopic composition of exchangeable carbon in the ocean-atmosphere  
661 pool as  $\delta^{13}\text{C}_T$ , then equate the mass of this pool  $M_T$  to the sum of its organic and inorganic  
662 components  $M_T = M_{inorganic} + M_{organic}$ . We can then write the pre-perturbation  
663 isotopic mass balance as:

664 
$$\delta^{13}\text{C}_T \cdot M_T = \delta^{13}\text{C}_{organic} \cdot M_{organic} + \delta^{13}\text{C}_{inorganic} \cdot M_{inorganic} \quad (1)$$

665 The values for present day the exchangeable dissolved organic and inorganic carbon  
666 pools are  $M_{organic} = 662$  Gt C, and  $M_{inorganic} = 37,400$  Gt C<sup>44,45</sup>, which we use as a reference  
667 point for the pre-perturbation Jurassic system.

668 We write the post-perturbation composition as  $\delta^{13}\text{C}'_T$ , based on the idea that this value  
669 deviates from  $\delta^{13}\text{C}_T$  as a function of the mass  $M_x$  and isotopic composition  $\delta^{13}\text{C}_x$  of some  
670 external carbon pool (methane, large igneous province derived CO<sub>2</sub> etc) putatively  
671 responsible for the perturbation:

672 
$$\delta^{13}\text{C}'_T = \frac{\delta^{13}\text{C}_T \cdot M_T + \delta^{13}\text{C}_X \cdot M_X}{M_T + M_X}, \therefore M_X = \frac{M_T(\delta^{13}\text{C}'_T - \delta^{13}\text{C}_T)}{\delta^{13}\text{C}_X - \delta^{13}\text{C}'_T} \quad (2)$$

673 The right hand side of (2) illustrates how the more negative  $\delta^{13}\text{C}_x$  (i.e. the isotopically  
674 lighter the carbon input) the lower  $M_x$  (i.e. the less carbon is needed to explain an  
675 excursion of a given magnitude). Sources of isotopically light carbon plausibly relevant to  
676 the Toarcian include CH<sub>4</sub> released by clathrate destabilization  $\delta^{13}\text{C}_{CH_4\ hyd} = -60\text{‰}$ <sup>45,46</sup>  
677 thermogenic CH<sub>4</sub> from contact metamorphism  $-35\text{‰} \leq \delta^{13}\text{C}_{CH_4\ therm} \leq -25\text{‰}$ <sup>47</sup>,  
678 CO<sub>2</sub> derived directly from magma  $-7\text{‰} \leq \delta^{13}\text{C}_{CO_2\ magma} = -5\text{‰}$  and/or thermogenic  
679 CO<sub>2</sub> sources associated with large igneous province emplacement  $-27\text{‰} \leq$   
680  $\delta^{13}\text{C}_{CO_2\ therm} \leq 2\text{‰}$ <sup>48</sup>.

681 The carbon isotopic dataset reaches a minimum of  $\delta^{13}\text{C} = -0.36\text{‰}$  after a downward  
682 trend that begins from an inflection point at  $\delta^{13}\text{C} = 3.13\text{‰}$ . Treating this as a single  
683 negative carbon isotopic excursion (NCIE) we calculate a magnitude of  $\Delta\delta^{13}\text{C}_{data,NCIE} =$   
684  $-(3.13 - -0.36) = -3.49\text{‰}$ . This happens within an interval of  $\Delta t_{NCIE} \sim 181.98 -$   
685  $181.70 = 0.28\text{Myrs}$ <sup>41</sup>. The NCIE is followed by a large amplitude positive excursion

686  $\Delta\delta^{13}C_{data,PCIE} = 5.13 - -0.36 = 5.49\%$ , which occurs over  $\Delta t_{NCIE} \sim 181.7$  Ma – 181.3  
 687 Ma = 0.4 Myrs<sup>41</sup>.

688 Writing  $\delta^{13}C_T = \delta^{13}C_{data,pre} = 3.13$  and  $\delta^{13}C_T' = \delta^{13}C_{data,pre} + \Delta\delta^{13}C_{data,NCIE} =$   
 689 –0.36 we can solve (2) for  $M_x$  using various different values of  $\delta^{13}C_x$  corresponding to the  
 690 above sources, thus estimate the mass of different types of carbon plausibly responsible.  
 691 This produces the results depicted in **Fig. S10** (see also **Table S8**).

692 The numbers for methane are in the same range as the Beerling et al. (2002)<sup>49</sup> upper  
 693 estimate of a clathrate-derived methane induced excursion of c. 5,000 Gt C, as well as  
 694 earlier estimates<sup>44</sup>, considering a likely background pCO<sub>2</sub> of approximately 2-4 time pre-  
 695 industrial values<sup>50</sup>.

696 The dynamical modelling results referred to in the main text correspond, unless  
 697 otherwise stated, to  $\delta^{13}C_{CO_2} = \delta^{13}C_{CO_2\ magma} = -7\%$  and  $\delta^{13}C_{CH_4} = \delta^{13}C_{CH_4\ hyd} =$   
 698 –60 %. The above mass balance calculations neglect dynamical carbon sinks and are  
 699 consequently underestimates. The input fluxes and the time interval over which these  
 700 fluxes were non-zero were tuned so as to reproduce the data:

$$701 TCO_2(\text{input}) = \int_{t_{start\ CO_2}}^{t_{end\ CO_2}} F_{Toarcian}(CO_2) dt \quad (3)$$

$$702 TCH_4(\text{input}) = \int_{t_{start\ CH_4}}^{t_{end\ CH_4}} F_{Toarcian}(CH_4) dt \quad (4)$$

703 With  $F_{Toarcian}(CO_2) = 3.6 \times 10^{13} \text{ mol yr}^{-1}$  and  $F_{Toarcian}(CH_4) = 1.107 \times 10^{12} \text{ mol yr}^{-1}$   
 704 with the time of the start and end of the CO<sub>2</sub> “burn”  $t_{start\ CO_2} = 181.87$  Ma,  $t_{end\ CO_2} =$   
 705 181.74 Ma and the time of methane input  $t_{start\ CH_4} = 181.75$  Ma,  $t_{end\ CH_4} = 181.65$  Ma.

706 This gives the total time-integrated carbon inputs to the dynamical model described  
 707 below is an LIP- CO<sub>2</sub> input  $F_{Toarcian}(CO_2) \cdot (0.13 \times 10^6 \text{ yrs}) = 5.25 \times 10^{18} \text{ mol}$ , or  
 708  $F_{Toarcian}(CO_2) \cdot (0.13 \times 10^6 \text{ yrs}) \cdot \frac{12.0107}{1 \times 10^{15}} = 63146 \text{ GtC}$  as LIP-associated CO<sub>2</sub>, and  
 709  $F_{Toarcian}(CH_4) \cdot (0.01 \times 10^6 \text{ yrs}) = 1.107 \times 10^{17} \text{ mol}$  or  $F_{Toarcian}(CH_4) \cdot (0.01 \times 10^6 \text{ yrs}) \cdot$   
 710  $\frac{12.0107}{1 \times 10^{15}} = 1329 \text{ GtC}$  as clathrate methane.

711 A coarse estimate of how much carbon would be required in order to explain the  
 712 observed PCIE can be derived by modifying (1) to describe the removal of mass  $M_X$ , i.e.

$$713 \delta^{13}C_T'(M_T - M_X) = \delta^{13}C_T \cdot M_T - \delta^{13}C_X \cdot M_X, \text{ thus } M_X = \frac{M_T(\delta^{13}C_T' - \delta^{13}C_T)}{(\delta^{13}C_T' - \delta^{13}C_X)}. \text{ Writing}$$

714  $\delta^{13}C_X = \delta^{13}C_{organic}$ , then equating the pre- and post- perturbation isotopic compositions  
 715 to  $\delta^{13}C_T = -0.36$ , and  $\delta^{13}C_T' = 5.13$ , and the duration of the PCIE from the data

716  $\Delta t_{data, PCIE} = 0.4$  Myrs. A provisional estimate of the necessary organic carbon burial  
717 flux can be provisionally derived using an intermediate value for the organic carbon  
718 isotopic composition  $\delta^{13}C_{organic} = -24.5\text{\textperthousand}$  (An expanded range  $-32.5\text{\textperthousand} \leq$   
719  $\delta^{13}C_{organic} \leq -17.5\text{\textperthousand}$ <sup>51</sup> is explored in the figure below ([Fig. S10](#))). These numbers (in  
720 GtC) can be related to the present day organic carbon burial flux  $mocb_0 = 3.75 \times$   
721  $10^{12} \text{mol yr}^{-1}$ <sup>52</sup> via  $GtC(\text{organic, out}) = x \cdot \int_0^{\Delta t_{data, PCIE}} mocb_0 dt$  where  $x$  is the  
722 magnitude of the organic carbon burial flux relative to present. Results of these  
723 calculations are listed in [Table S8](#).

724 However, these are underestimates because the mass balance calculation in (2) neglects  
725 both dynamical carbon sinks and the fact the positive excursion occurs after the carbon  
726 input corresponding to the negative excursion, which will increase the baseline reservoir  
727 size  $M_T$ . Consequently we now turn to a dynamical modelling approach.

728

### 729 **Proxy inversion modelling**

730 Our inversion model aims to get the maximum amount of information from the dataset  
731 whilst making the minimum possible number of assumptions. We proceed by back-  
732 calculating CO<sub>2</sub> and temperature via the δ<sup>18</sup>O data, then estimating carbon cycle fluxes  
733 compatible with both these calculations and the δ<sup>13</sup>C data:

- 734 1. The δ<sup>18</sup>O dataset is related to global average surface temperature using an existing  
735 empirical formulation<sup>32</sup> (see below).
- 736 2. This δ<sup>18</sup>O-inversion temperature  $T_{\delta^{18}O}$  is used to estimate a corresponding value for  
737 relative atmospheric CO<sub>2</sub>,  $R_{CO_2}(\delta^{18}O)$  using the Geocarbulf model's temperature  
738 function.
- 739 3. Estimates of the normalized magnitude of uplift  $U$ , degassing  $D$  and bulk weathering  $W$   
740 are taken from the forcings for the COPSE model<sup>53</sup> across the time interval  
741 corresponding to the dataset – allowing us to estimate the various weathering fluxes  
742 relevant to the organic and carbonate carbon cycle mass balances.
- 743 4. The marine carbonate carbon burial flux  $mccb$  is assumed to be calculable from mass  
744 balance with the silicate and carbonate weathering fluxes (or, in an alternative scenario,  
745 the size and distribution of the atmosphere ocean CO<sub>2</sub> reservoir).
- 746 5. The combination of all the above flux estimates, the δ<sup>13</sup>C data, and isotopic mass  
747 balance, allows us to estimate the marine organic carbon burial  $mocb$  flux.
- 748 6. The marine phosphate concentration  $\bar{P}$  corresponding to this marine organic carbon  
749 burial flux, along with a rough estimate of the corresponding global ocean anoxic  
750 fraction  $f_{anox}$  is then calculated.

751 Thus, our aim in this section is to describe an approximate mapping from each δ<sup>13</sup>C, δ<sup>18</sup>O  
752 datapoint to temperature, carbon cycle weathering/burial fluxes, marine limiting  
753 nutrient concentration, and finally anoxia.

754 We begin with Berner's global carbon isotopic mass balance<sup>54</sup>, which is an isotopically  
 755 weighted mass balance combining the inputs to and outputs from the organic and  
 756 carbonate carbon cycles (please see **Table S9** for flux abbreviations):

$$757 \delta^{13}C_C \cdot (carbw + ccdeg) + \delta^{13}C_G \cdot (oxidw + ocdeg) + \delta^{13}C_{\Delta toarcian} \cdot F_{\Delta toarcian} \\ 758 = \delta^{13}C_{mccb} \cdot mccb + (\delta^{13}C_{mccb} - \varepsilon) \cdot mocb \quad (5)$$

759 The isotopic composition  $\delta^{13}C_{mccb}$  of the marine carbonate carbon burial (mccb) flux is  
 760 assumed to reflect the isotopic composition of the marine DIC pool and is given by:

$$761 \delta^{13}C_{mccb} = \frac{\delta^{13}C_C \cdot (carbw + ccdeg) + \delta^{13}C_G \cdot (oxidw + ocdeg) + \varepsilon \cdot mocb + \delta^{13}C_{\Delta toarcian} \cdot F_{\Delta toarcian}}{mocb + mccb} \quad (6)$$

762 Where  $\delta^{13}C_{\Delta toarcian} \cdot F_{\Delta toarcian}$  is the isotopically weighted input from the putative  
 763 Toarcian-specific perturbation, i.e. the sum of large igneous province (LIP) associated  
 764  $CO_2$  degassing and  $CO_2$  associated with the oxidation of clathrate-derived  $CH_4$ :

$$765 \delta^{13}C_{\Delta toarcian} \cdot F_{\Delta toarcian} = \delta^{13}C_{LIP} \cdot F_{LIP} + \delta^{13}C_{CH_4} \cdot F_{CH_4} \quad (7)$$

766 (Note that the above is set to zero by default for the figure discussed in the main text,  
 767 because in this exercise we treat each  $\delta^{13}C$  data point as reflecting a mass balance within  
 768 which the above fluxes have already gone in to the atmospheric  $CO_2$  pool, and thus drive  
 769 the temperature increase). The  $\delta^{18}O$  data is related to the inversion model temperature  
 770 estimate using the fit of Brand et al (2013)<sup>32</sup>, which incorporates the impact on  $\delta^{18}O$  of  
 771 the proportion of  $MgCO_3$  in the shell:

$$772 T_{\delta^{18}O (model)} = 16.192 - 3.468 \cdot (\delta^{18}O_{data} - \delta^{18}O_{SW} - \delta_{Mg}) \quad (8)$$

773 Where we assume, in line with previous estimates, that the average seawater isotopic  
 774 composition can be approximated by  $\delta^{18}O_{SW} = -1\text{\textperthousand}$ , and the magnesium calcite  
 775 adjustment factor  $\delta_{Mg} = 0.17 \text{ mol\% } MgCO_3$ <sup>14</sup>, was for this dataset approximately  
 776  $\text{mol\% } MgCO_3 = 0.4$ . For comparison, we additionally show Andersen & Arthur's<sup>39</sup> fit,  
 777 which does not include a magnesium calcite correction:

$$778 T_{\delta^{18}O (reference)} = 16.0 - 4.14 \cdot \delta^{18}O_{data} + 0.13 \cdot (\delta^{18}O_{data})^2 \quad (9)$$

779 We equate (9) to the Geocarbsulf's temperature function:

$$780 T_{\delta^{18}O} - T_0 = ESS \cdot \frac{\ln\left(\frac{CO_2 \text{ (atmos)}}{CO_2_0}\right)}{\ln(2)} - W_s \left(\frac{t_{bp}}{570}\right) + GEOG \quad (10)$$

781 Where the baseline modern temperature  $T_0 = 15^\circ C$ ,  $ESS = 5$  is the "Earth system  
 782 sensitivity" (long term climate sensitivity),  $GEOG = 3$  (corresponding to the early  
 783 Jurassic) is Royer's adjustment to Berner's original model to express the sensitivity of  
 784 temperature to changes in paleogeography<sup>55</sup>,  $W_s = 7.4$  represents Berner's linearization

of the luminosity component of the temperature function<sup>56</sup>, atmospheric  $CO_2$  is normalized to pre-industrial levels of  $CO_{2\ 0} = 280$  ppm and  $t_{bp}$  is the model time in millions of years before present. This allows us to derive an estimate of the relative atmospheric  $R_{CO_2} = \frac{CO_2(\text{atmos})}{CO_{2\ 0}}$  corresponding to each inversion temperature.

$$R_{CO_2(\delta^{18}O)} = \frac{CO_2(\text{atmos})}{CO_{2\ 0}} = e^{(T_{\delta^{18}O} - T_0 - GEOG + W_s(\frac{t_{bp}}{570})) \cdot \frac{\ln(2)}{ESS}} \quad (11)$$

Several of the fluxes in (5) are plausibly a function of the relative size of the carbonate and organic carbon rock reservoirs. The differential equations describing the mass of carbonate  $C$  and organic  $G$  carbon are estimated by simple differential equations of the form given by Berner's original Geocarb model:

$$\frac{dc}{dt} = mccb - carbw - ccdeg \quad (12)$$

$$\frac{dG}{dt} = mocb - oxidw - ocdeg \quad (13)$$

Degassing fluxes are constrained by time-dependent forcings taken from the COPSE model<sup>53</sup>:

$$ccdeg = ccdeg_0 \cdot D_{(t_{bp})} \quad (14)$$

$$ocdeg = ocdeg_0 \cdot D_{(t_{bp})} \quad (15)$$

Where  $D_{(t_{bp})}$  is a normalized estimate of the time-specific degassing rate. We estimate the carbonate  $carbw$  and oxidative  $oxidw$  weathering fluxes via:

$$carbw = carbw_0 \cdot U_{(t_{bp})}^{0.9} \cdot (1 + 0.087 \cdot \Delta T) \cdot 2 \cdot \left( \frac{R_{CO_2(\delta^{18}O)}}{1 + R_{CO_2(\delta^{18}O)}} \right) \cdot \frac{C(t)}{C_0} \quad (16)$$

$$oxidw = oxidw_0 \cdot U_{(t_{bp})} \cdot \frac{G(t)}{G_0} \quad (17)$$

Where  $\Delta T = T_{\delta^{18}O} - T_0$  is the deviation between the temperature estimated from the proxy inversion and the baseline planetary average. (We also experimented with an adjustment for the bias in global weathering to tropical latitudes  $\Delta T_{tropics} = \frac{2}{3} \Delta T^5$ , but this did not qualitatively alter the results).

We explored two options for the marine carbonate carbon burial flux  $mccb$ . The default carbonate carbon burial flux was assumed to balance carbonate and silicate weathering:

$$mccb_{balance} = carbw + silw \quad (18)$$

The kinetic-limited silicate weathering flux scales with temperature and  $CO_2$  via Caldeira and Kasting (1992)<sup>57</sup>:

$$silw_{kinetic} = silw_0 \cdot U_{(t_{bp})}^{0.33} \cdot e^{0.09\Delta T} \cdot (1 + 0.038 \cdot \Delta T)^{0.65} \cdot \sqrt{R_{CO_2(\delta^{18}O)}} \quad (19)$$

814 Limitation of silicate weathering by the supply, via physical erosion, of silicate cations in  
 815 weatherable rock is imposed using a formulation from previous deep time work<sup>58</sup>:

$$816 \quad silw_{supply} = silw_{kinetic} + \frac{silw_{max} - silw_{kinetic}}{1 + e^{-k_{supply}(silw_{kinetic} - silw_{max})}} \quad (20)$$

817 Where  $silw_{max} = 3 \cdot silw_0$  and  $k_{supply} = 100$ , such that the formulation in (20) dictates  
 818 the manner in which  $silw_{supply}$  plateaus out at  $silw_{max}$  at high weathering rates. In the  
 819 simulations discussed in the main text we imposed supply limitation of silicate  
 820 weathering at lower thresholds of 1.5 to 2 times the modern value.

821 An alternative functional form of the marine carbonate carbon burial flux involves a  
 822 coarse approximation to its (short-term) dependence on carbonate alkalinity:

$$823 \quad mccb_{variable} = mccb_0 \cdot RCO_{2(ocean)} \quad (21)$$

824 Where  $RCO_{2(ocean)}$  is the normalized size of the marine component of the global ocean-  
 825 atmosphere  $CO_2$  reservoir. In keeping with the revised COPSE model<sup>59</sup> and previous  
 826 calculations<sup>51</sup>, we assume that relative atmospheric  $CO_2$  scales with the second power of  
 827 the normalized reservoir size:

$$828 \quad R_{CO_2(\delta^{18}O)} = \left( \frac{A(t)}{A_0} \right)^2, \therefore A(t) = A_0 \cdot \sqrt{R_{CO_2(\delta^{18}O)}} \quad (22)$$

829 This allows us to estimate the atmospheric fraction  $\phi$  of the total ocean-atmosphere  $CO_2$   
 830 reservoir (assuming a constant total number of moles of air in the atmosphere of  
 831  $mol_{atmos} = 1.773 \times 10^{20}$ ):

$$832 \quad \phi_{(t)} = \frac{R_{CO_2(\delta^{18}O)} \cdot CO_{2\ 0} \cdot 1 \times 10^{-6} \cdot mol_{atmos}}{A_0 \cdot \sqrt{R_{CO_2(\delta^{18}O)}}} \quad (23)$$

833 Which finally gives the ocean component of the  $CO_2$  reservoir, scaled relative to present  
 834 day values:

$$835 \quad RCO_{2(ocean)(t)} = \frac{(1 - \phi_{(t)})A(t)}{(1 - \phi_0)A_0} \quad (24)$$

836 This is then plugged into the  $mccb_{variable}$  flux (21).

837 The only remaining undetermined flux, marine organic carbon burial, can now be  
 838 calculated by assuming  $\delta^{13}C_{mccb} = \delta^{13}C_{data}$  and solving (5) for this flux:

$$839 \quad mocb = \frac{\delta^{13}C_C \cdot (carbw + ccdeg) + \delta^{13}C_G \cdot (oxidw + ocdeg) + \delta^{13}C_{\Delta toarcian} \cdot F_{\Delta toarcian} - \delta^{13}C_{mccb} \cdot mccb}{(\delta^{13}C_{mccb} - \varepsilon)} \quad (25)$$

840 We initialize at the first time step using isotopic compositions for carbonate  $\delta^{13}C_C = 0\text{‰}$   
 841 and organic carbon in rock  $\delta^{13}C_G = -\varepsilon = -24.5$  and modern day reservoir sizes  $C_0$  and  
 842  $G_0$ , then proceed to use the dataset to solve the differential equations (24) and (25) by

843 Euler's method. Berner's original equations for the change over time in the isotopic  
 844 composition of the organic and carbonate rock reservoirs were also used:

$$845 \quad \frac{d\delta_{CC}}{dt} = \delta_{mccb} \cdot mccb - \delta_C \cdot carbw - \delta_C \cdot ccdeg \quad (26)$$

$$846 \quad \frac{d\delta_{GG}}{dt} = (\delta_{mccb} - \varepsilon) \cdot mocb - \delta_G \cdot oxidw - \delta_G \cdot ocdeg \quad (27)$$

847 For each estimate of marine organic carbon burial *mocb* that we arrive at (i.e. at each  
 848 timestep), we calculate the corresponding relative concentration of limiting nutrient  
 849 necessary to sustain it:

$$850 \quad mocb = mocb_0 \cdot \bar{P}^2, \therefore \bar{P} = \frac{PO_4}{PO_{40}} = \sqrt{\frac{mocb}{mocb_0}} \quad (28)$$

851 The global phosphorous weathering flux is taken from COPSE, and is a function of  
 852 temperature,  $CO_2$  and the other weathering fluxes:

$$853 \quad phosw = phosw_0 \left( f_{silw} \frac{silw}{silw_0} + f_{carbw} \frac{carbw}{carbw_0} + f_{oxidw} \frac{oxidw}{oxidw_0} \right) \quad (29)$$

854 Where we use recently revised apportioning factors are  $f_{silw} = 0.58$ ,  $f_{carbw} = 0.21$ ,  
 855  $f_{oxidw} = 0.21$ . The formulations of the calcium-phosphate burial flux *capb*, iron adsorbed  
 856 phosphate burial flux *fepb* and marine organic phosphate *mopb* are given by:

$$857 \quad capb = capb_0 \cdot \bar{P}^2 \quad (30)$$

$$858 \quad fepb = fepb_0 (1 - f_{anox}) \quad (31)$$

$$859 \quad mopb = mocb \left( \frac{f_{anox}}{CP_{anox}} + \frac{1-f_{anox}}{CP_{ox}} \right) \quad (32)$$

860 We make the (highly idealized/approximate) simplifying assumption that the global  
 861 phosphate reservoir's dynamics are at roughly steady state at each carbon isotope data  
 862 point:

$$863 \quad \frac{d\bar{P}}{dt} = phosw - capb - fepb - mopb \approx 0 \quad (33)$$

864 This assumption allows us to estimate the global ocean anoxic fraction  $f_{anox}$  by  
 865 substituting (35)-(38) into (39):

$$866 \quad f_{anox} = \frac{phosw - capb - fepb_0 - \frac{mocb}{CP_{ox}}}{mocb \left( \frac{1}{CP_{anox}} - \frac{1}{CP_{ox}} \right) - fepb_0} \quad (34)$$

867 Where we additionally impose the necessary constraint that  $0 \leq f_{anox} \leq 1$ .

868 To sum up, we have used the  $\delta^{18}O$  data to produce a temperature (thus  $CO_2$  greenhouse)  
 869 estimate, then plugged this estimate and the  $\delta^{13}C_{data}$  into an isotopically weighted  
 870 carbon cycle mass balance in order to estimate marine organic carbon burial, thus

871 limiting nutrient concentration, thus anoxia. The results of this proxy inversion exercise  
 872 are discussed in the main text. Discrete values taken for modelling are listed in **Table S9**.  
 873

874 ***Forward modelling in the COPSE (Carbon, Oxygen, Phosphorous, Sulphur, Evolution)  
 875 model***

876 In the forward model we aim to reproduce the data using prescribed greenhouse forcings,  
 877 as opposed to using this data to drive the model. Full model equations for COPSE can be  
 878 found in the original descriptions<sup>53,59</sup>; we restrict our description here to those fluxes of  
 879 key conceptual relevance. The greenhouse forcings dictating the injection of LIP- $CO_2$  and  
 880 clathrate  $CH_4$  are given by (also see equations (3) and (4) above):

881  $F_{LIP\ CO_2(t_{LIP\ start} \geq |t_{bp}| \geq t_{LIP\ end})} = F_{Toarcian\ (CO_2)_0},\ F_{LIP\ CO_2(\neg(t_{LIP\ start} \geq |t_{bp}| \geq t_{LIP\ end}))} = 0$  (35)

882  $F_{Clathrate\ CH_4(t_{CH_4\ start} \geq |t_{bp}| \geq t_{CH_4\ end})} = F_{Toarcian\ (CH_4)_0}$

883  $F_{Clathrate\ CH_4(\neg(t_{CH_4\ start} \geq |t_{bp}| \geq t_{CH_4\ end}))} = 0$  (36)

884 Where  $t_{bp}$  is model time in millions of years before present and  $t_{LIP\ start}, t_{LIP\ end}$   
 885  $t_{CH_4\ start}, t_{CH_4\ end}$  are tuneable parameters describing, respectively, the time (in years  
 886 before present) at which LIP- $CO_2$  and clathrate  $CH_4$  begin and cease. Additional forcings  
 887 are degassing  $D$ , uplift  $U$ , weathering  $W$ , and relative biotic terrestrial evolution  $E$ , from  
 888 the original model.

889 As above, the  $\delta_{mccb}$  value predicted by the model is assumed equilibrated with the  
 890 isotopic composition of the global ocean-atmosphere  $CO_2$  reservoir  $A$ ,  $\delta_{mccb} = \delta_A$ . The  
 891 mass and isotopic composition of the global ocean-atmosphere  $CO_2$  reservoir changes  
 892 over time according to:

893  $\frac{dA}{dt} = ocdeg + ccdeg + oxidw + carbw - mccb - mocb - tocb - sfw + F_{LIP\ CO_2} +$   
 894  $F_{Clathrate\ CH_4}$  (37)

895  $\frac{d(\delta_A A)}{dt} = \delta_G(ocdeg + oxidw) + \delta_C(ccdeg + carbw) - \delta_A mccb - (\delta_A - \varepsilon_{ocean})mccb$   
 896  $- (\delta_A - \varepsilon_{land})toci + \delta^{13}C_{CH_4}F_{Clathrate\ CH_4} + \delta^{13}C_{LIP}F_{LIP\ CO_2}$  (38)

897 Where the isotopic composition of the organic  $\delta_G$  and carbonate  $\delta_C$  rock reservoirs  
 898 change according to (26) and (27). The terrestrial organic carbon burial flux  $toci$  is  
 899 related to phosphorous weathering of the terrestrial rock surface:

900  $toci = 0.02041 \cdot V \cdot CP_{land} \cdot phosw$  (39)

901 Where  $CP_{land} = 1000$ . The relative mass of the terrestrial photosynthetic biosphere  $V$   
 902 exhibits a simple Michaelis-Menten style dependence on atmospheric  $CO_2$ , a dependence  
 903 on temperature relative to a presumed maximum productivity at  $T_{P_{max}} = 25^\circ C$ , and is  
 904 inhibited by excessive oxygen levels in a way the represents photorespiration and fire:

$$905 \quad V = k_{npp} \cdot E_{(t_{bp})} \cdot (1.5 - 0.5 \cdot \bar{O}) \cdot \left(1 - \left(\frac{T-T_{P_{max}}}{T_{P_{max}}}\right)^2\right) \cdot \left(\frac{P_{CO_2}-P_{min}}{\frac{P_1+P_{CO_2}-P_{min}}{2}}\right) \cdot \left(\frac{k_{fire}}{k_{fire}-1+ignit}\right)$$

906 (40)

907 Where  $k_{npp} = 2$  is a normalizing constant,  $E_{(t_{bp})} = 1$  is the terrestrial evolutionary  
 908 forcing corresponding to the Jurassic,  $\bar{O} = \frac{O_2}{O_{2\ 0}}$  is the normalized global oxygen reservoir  
 909 size,  $P_{CO_2} = R_{CO_2} \cdot CO_{2\ 0}$  is the atmospheric  $CO_2$  mixing ratio in parts per million,  $P_{min} =$   
 910  $10\ ppm$  and  $P_{\frac{1}{2}} = 183.6\ ppm$  express the dependence of primary production on  $P_{CO_2}$ ,  
 911  $k_{fire} = 3$  expresses a 50% suppression of vegetation today relative to a world with no  
 912 fire<sup>60</sup>, and  $ignit$  is a measure of the magnitude of the negative impact of fires on  
 913 terrestrial production as oxygen's mixing ratio increases, given by Lenton et al (2018)<sup>59</sup>:

$$914 \quad ignit = MIN \left[ MAX \left[ 48 \cdot \left( \frac{\bar{O}}{\bar{O}+3.762} \right) - 9.08, 0 \right], 5 \right] \quad (41)$$

915 Removal of  $CO_2$  at the deep ocean crust via seafloor "weathering"  $sfw$  is assumed to  
 916 exhibit a kinetic dependence on temperature comparable to terrestrial basalt  
 917 weathering:

$$918 \quad sfw = sfw_0 \cdot k_{sfw} \cdot D_{(t_{bp})} \cdot e^{k_T sfw \Delta T} \quad (42)$$

919 Where  $sfw_0 = 3 \times 10^{12} mol yr^{-1}$ ,  $k_{sfw} = 0.068$ ,  $k_T sfw = 0.1332$ . Terrestrial silicate and  
 920 carbonate weathering fluxes are enhanced by the biosphere via  $V$  using the formulation  
 921 from the original COPSE model<sup>53</sup>:

$$922 \quad f_{Tsilw} = e^{0.09 \Delta T} \cdot (1 + 0.038 \Delta T)^{0.65} \quad (43)$$

$$923 \quad f_{CO_2\ silw} = \sqrt{R_{CO_2}} \left( 1 - MIN \left[ V \cdot W_{(t_{bp})}, 1 \right] \right) + \left( \frac{2 \cdot R_{CO_2}}{R_{CO_2} + 1} \right)^{0.4} \cdot MIN \left[ V \cdot W_{(t_{bp})}, 1 \right] \quad (44)$$

$$924 \quad silw = silw_0 \cdot U_{(t_{bp})} \cdot f_{Tsilw} \cdot f_{CO_2\ silw} \cdot \left( k_{plants} + (1 - k_{plants}) \cdot MIN \left[ V \cdot W_{(t_{bp})}, 1 \right] \right) \quad (45)$$

925 Similarly for the carbonate weathering flux:

$$926 \quad g_{Tcarbw} = 1 + 0.087 \Delta T \quad (46)$$

$$927 \quad g_{CO_2\ carbw} = f_{CO_2\ silw} \quad (47)$$

$$928 \quad carbw = carbw_0 \cdot U_{(t_{bp})} \cdot g_{Tcarbw} \cdot g_{CO_2\ carbw} \cdot \left( k_{plants} + (1 - k_{plants}) \cdot MIN \left[ V \cdot \right. \right. \\ 929 \quad \left. \left. W_{(t_{bp})}, 1 \right] \right) \quad (48)$$

930 The time derivative for the global oxygen reservoir is identical to that of the original  
 931 model, except for the addition of an oxygen sink for those time steps at which the  $CH_4$   
 932 input is non-zero (at which points we assume complete and instantaneous oxidation to  
 933  $CO_2$  via stoichiometry  $CH_4 + 2O_2 \rightarrow CO_2 + 2H_2O$ ):

$$934 \quad \frac{dO}{dt} = mocb + tocb - oxidw + 2 \cdot (mpsbt - pyrw - pyrdeg) - 2 \cdot F_{Clathrate\ CH_4} \quad (49)$$

935 Where the other fluxes are (left to right) marine organic carbon burial, terrestrial organic  
 936 carbon burial, oxidative weathering, marine pyrite sulphur burial, pyrite weathering,  
 937 pyrite degassing (see **Table S9** for a full list of abbreviations). The formulation of each of  
 938 these fluxes is:

$$939 \quad mocb = mocb_0(\bar{P}^2) \cdot \alpha e^{-\beta O_2\ conc} \quad (50)$$

940 For  $\alpha = 2.217$ ,  $\beta = 2277$ , and  $O_2\ conc$  is an estimate of the oxygen concentration in  
 941 surficial seawater corresponding to the global reservoir size  $O_2\ conc = \bar{O} \cdot O_2\ conc_0$ , where  
 942  $O_2\ conc_0 = 331.5\ \mu mol kg^{-1}$ . The sulphur cycle is a key component of the Earth system's  
 943 response to global anoxic events, including the Toarcian<sup>61</sup>. The relationship between  
 944 burial of marine pyrite, that of marine organic carbon and the oxygen/sulphur marine  
 945 reservoirs, is written as:

$$946 \quad mpsb_{revised} = mocb \cdot \left( \frac{f_{anox}}{C:S_{anox}} + \frac{1-f_{anox}}{C:S_{ox}} \right) \quad (51)$$

947 Where  $C:S_{anox} = 2$ ,  $C:S_{ox} = 3.5$ <sup>32</sup>. The weathering and degassing of pyrite in rock is  
 948 described by:

$$949 \quad pyrw = pyrw_0 \cdot U_{(t_{bp})} \cdot \frac{PYR}{PYR_0} \quad (52)$$

$$950 \quad pyrdeg = pyrdeg_0 \cdot D_{(t_{bp})} \cdot \frac{PYR}{PYR_0} \quad (53)$$

951 The pyrite rock reservoir  $PYR$  changes according  $\frac{dpyr}{dt} = pyrw + pyrdeg - mpsb$  as  
 952 described in the original model.

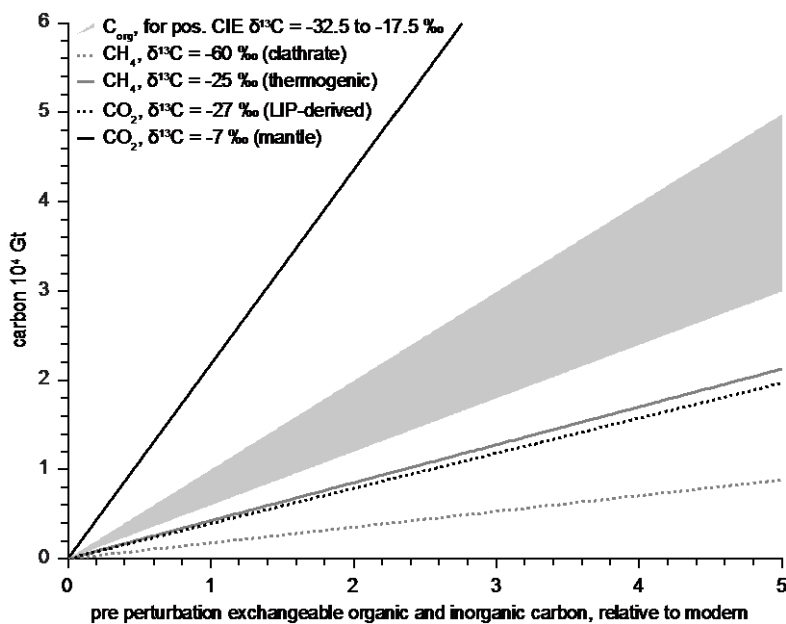
953

954 ***Elaboration on modelling results***

955 *Mass balance calculations*

956 A simple estimate of the mass of  $^{13}C$ -depleted carbon that must be introduced into the  
 957 exchangeable ocean-atmosphere carbon pool in order to drive the observed negative CIE  
 958 can be derived from simple mass balance equations (see supplement, model description  
 959 section 1<sup>42</sup>). **Figure S10** depicts the requisite quantity of methane carbon derived from  
 960 clathrate-decomposition ( $\delta^{13}C_{CH_4\ hyd} = -60\text{‰}$ )<sup>46</sup> or contact metamorphism  
 961 ( $\delta^{13}C_{CH_4\ therm} \leq -25\text{‰}$ )<sup>47</sup>, as well as that of  $CO_2$  carbon derived directly from magma  
 962 ( $-7\text{‰} \leq \delta^{13}C_{CO_2\ magma} = -5\text{‰}$ )<sup>62</sup> or thermogenic sources ( $-27\text{‰} \leq \delta^{13}C_{CO_2\ therm} \leq$   
 963  $5\text{‰}$ )<sup>47</sup>. Additionally depicted for reference is the quantity of organic carbon (assuming  
 964  $-32.5\text{‰} \leq \delta^{13}C_{organic} \leq -17.5\text{‰}$ , e.g. Ref. 38) that would need to be removed from the  
 965 exchangeable pool (i.e. buried) in order to explain the positive isotopic excursion (i.e. the  
 966 recovery from the negative CIE). However in this latter case it is more realistic to conceive  
 967 of the carbon burial increase as a continuous dynamical change than the discrete  
 968 perturbation represented by these calculations.

969



970 **Figure S10:** Simple mass balance calculations depicting the quantity of methane (grey) and  $CO_2$  (black)  
 971 needed to drive the observed negative carbon isotopic excursion, and the amount of additional organic  
 972 carbon burial (grey field) necessary to drive the observed positive carbon isotopic excursion, assuming  
 973 different pre-perturbation sizes of the combined organic/inorganic ocean-atmosphere exchangeable  
 974 carbon pool relative to present.

975

976

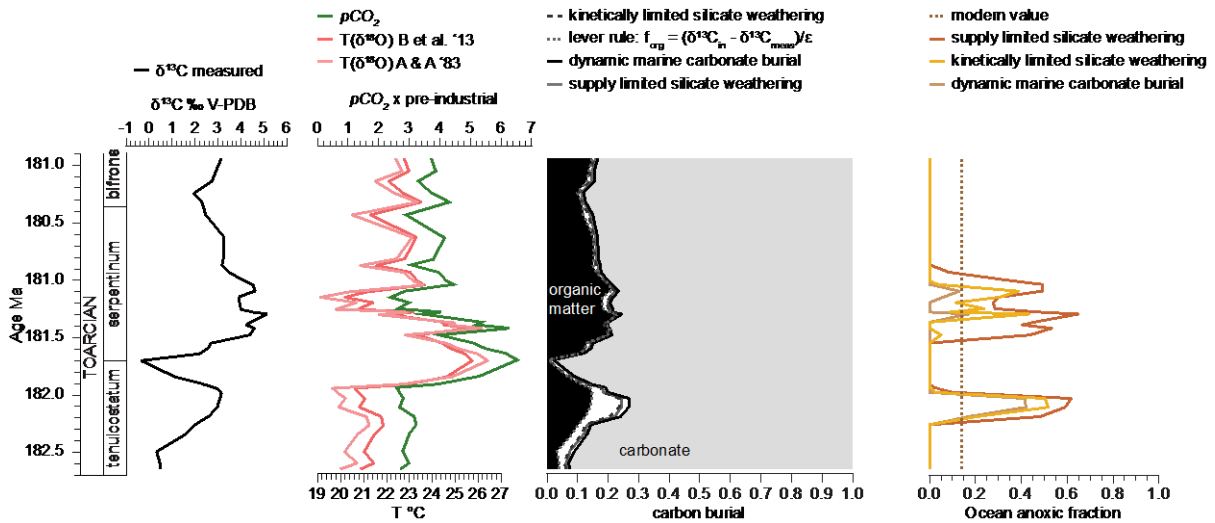
977

978 *Proxy Inversion model*

979 The results of proxy inversion modelling are depicted in **Figure S11**. The inversion  
980 temperature  $T_{\delta^{18}O}$  is compatible with a hyperthermal interval and supports a  $\sim 2 - 4^{\circ}\text{C}$   
981 increase precisely in line with the negative CIE, strongly supporting the case for methane  
982 induced warming, in the context of a prolonged, baseline hyperthermal state.

983 The organic carbon burial “ $f$ ” ratio positively covaries with  $\delta^{13}\text{C}$ , reaching a lower limit  
984 at the most negative point of the CIE. This is based on the assumption that the organic  
985 carbon burial flux is in equilibrium with a carbonate burial flux, which in turn  
986 proportionally increases in line with the  $\text{CO}_2/\text{CH}_4$  input, which is, in turn, tracked by the  
987 negative CIE (see model description, equation (10)). However, as  $\delta^{13}\text{C}$  approaches zero  
988 it is highly likely that the system deviates from steady state- with the implication that the  
989 “ $f$ ” ratio estimates at this point are loose approximations only. All other factors being  
990 equal, high marine organic carbon burial necessitates both high limiting nutrient  
991 concentration (to support the production) and translates into high ocean anoxia (due to  
992 the increased oxygen consumption as the organic carbon is remineralized).

993 The marine carbonate carbon burial flux is generally assumed to balance silicate and  
994 carbonate weathering over timescales of the order of that represented by the dataset (e.g.  
995 Ref. 51); which implicitly assumes continuous carbonate supersaturation in the ocean.  
996 We (simplistically) represent a scenario in which this assumption is relaxed (e.g. due to  
997 short term changes in marine carbonate alkalinity, and/or insufficient time for carbonate  
998 burial to equilibrate with increased weathering), via a formulation in which marine  
999 carbonate carbon burial scales with total ocean inorganic carbon (see description). This  
1000 translates into a lower carbonate burial flux (and correspondingly higher organic flux in  
1001 order to sustain mass balance).



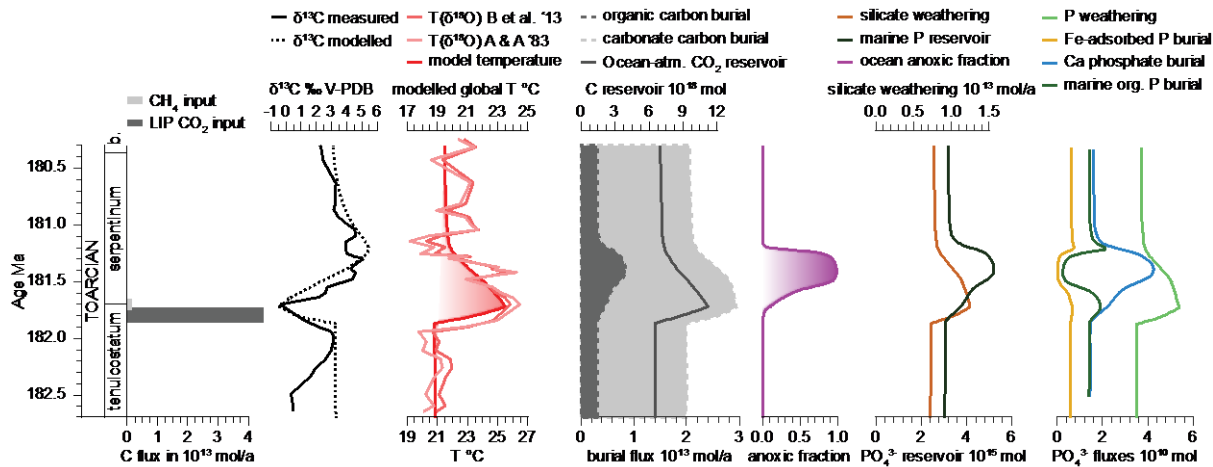
1002

1003 **Figure S11:** Results of a Geocarb-style inversion model in which the data is used to directly infer  
1004 temperature,  $\text{CO}_2$ , carbon cycle fluxes and anoxia.  $\delta^{18}\text{O}$  (red dotted line) and  $\delta^{13}\text{C}$  (blue dotted line) data,  
1005 temperature inversions (yellow and purple lines) corresponding to the former, and the corresponding  
1006 relative atmospheric  $\text{CO}_2$  level (green line) calculated from the selected (yellow) temperature, using  
1007 Geocarbsulf's temperature function. The organic carbon burial “ $f$ ” ratios  $f_{\text{org}} = \frac{\text{mocb}}{\text{mocb} + \text{mcbb}}$  calculated from  
1008 the model temperature and  $\text{CO}_2$  and isotopic mass balance (model description, equations (10) and (31))  
1009 under different scenarios for the other carbon cycle fluxes with which marine organic carbon burial is in  
1010 mass balance. Grey solid line shows a supply (i.e. rock substrate) limited silicate weathering flux, dashed  
1011 black line a kinetically (i.e.  $\text{CO}_2$ , temperature) flux, black solid line a scenario in which the marine carbonate  
1012 carbon burial flux scales with the relative size of the marine inorganic carbon pool (rather than balancing  
1013 weathering as in the other scenarios). Dashed grey line shows a “traditional” steady state interpretation of  
1014 the  $\delta^{13}\text{C}$  record in which the organic fraction is calculated from  $\delta^{13}\text{C}$  assuming constant weathering input  
1015  $\delta^{13}\text{C}_{\text{in}} = -0.5\text{‰}$  and organic fractionation  $\varepsilon = -24.5\text{‰}$  (e.g., Ref 51). Global ocean anoxic fraction  
1016 calculated from the marine organic carbon burial fluxes, combined with the assumption of steady state  
1017 marine phosphate. Dashed brown line shows modern value.  
1018

### 1019 Forward biogeochemical modelling

1020 Results of COPSE (Carbon, Oxygen, Phosphorous, Sulphur, Evolution)<sup>53,59</sup> forward  
1021 biogeochemical box modeling using Toarcian-specific tectonic forcings representing  
1022 large igneous province (LIP)-derived  $\text{CO}_2$  and hydrate-derived  $\text{CH}_4$  (see model  
1023 description) are presented in **Figure S12**. The greenhouse perturbation translates to an  
1024 increase in the input of phosphorous to the ocean via weathering, which boosts  
1025 production, marine organic carbon burial and respiratory oxygen demand. This increases  
1026 marine anoxia, reducing marine phosphate burial<sup>63</sup>, further boosting organic carbon  
1027 production, within a net positive feedback. The timing of anoxia lags behind that of the  
1028 greenhouse input (consistent with the lag between the most negative lower limit of the  
1029  $\delta^{13}\text{C}$  curve and the maximum value of the marine organic carbon burial flux implied by  
1030 the inversion model). The hyperthermal interval also lasts longer than the negative CIE  
1031 (due to the time needed for weathering to consume the  $\text{CO}_2$  introduced via the  
1032 perturbation).

1033 The OAE terminates as a result of the “extra” (i.e. perturbation induced) CO<sub>2</sub> input being  
 1034 consumed by the silicate weathering flux, as well as a slight increase in oxygen caused by  
 1035 the elevated marine organic carbon burial flux (not shown, see supplement). As above,  
 1036 the time interval required to bring CO<sub>2</sub> down to pre-perturbation levels is increased if  
 1037 silicate weathering becomes supply limited.



1038

1039 **Figure S12:** Reproduction of the coarse features of the δ<sup>13</sup>C data by transient injection of CO<sub>2</sub> and CH<sub>4</sub> in  
 1040 the COPSE forward biogeochemical model. δ<sup>13</sup>C data and greenhouse forcings relative to baseline fluxes  
 1041 (model description, equations (7) and (8)). An initial boundary condition of δ<sup>13</sup>C<sub>c</sub> = +2 ‰ is imposed on  
 1042 the carbonate carbon rock reservoir. Injected CO<sub>2</sub> is assumed to be thermogenic with δ<sup>13</sup>C value of -27 ‰,  
 1043 and assumed δ<sup>13</sup>C for injected methane is -60 ‰. Modelled global temperature (red line with shading)  
 1044 is shown together with local temperature reconstructions based on fossil oxygen isotope ratios converted  
 1045 using equations by Brand et al. (2013)<sup>31</sup> and Anderson and Arthur (1983)<sup>38</sup>. Carbon cycle fluxes and relative  
 1046 size of global ocean-atmosphere CO<sub>2</sub> reservoir (dark grey line). Note the increase in marine organic carbon  
 1047 burial (dark grey field) and silicate weathering (brown line), given by the minimum of the kinetically  
 1048 limited and supply limited flux values with W<sub>max</sub> = 2 \* silw<sub>0</sub> associated with the anoxic event. Global ocean  
 1049 anoxic fraction and various fluxes relevant to the marine phosphate cycle. Note the decline in iron-adsorbed  
 1050 and organic phosphate burial as anoxia increase.  
 1051

### 1052 *Formulation of ocean anoxic fraction*

1053 The representation of the global ocean anoxic fraction depicted in **Figure S12** is defined  
 1054 as the fraction of the ocean surface area below which the saturation of oxygen in the  
 1055 oxygen minimum zone would be less than 10%<sup>64</sup>. An alternative formulation<sup>59</sup> represents  
 1056 the fraction of the seafloor directly overlain by anoxic waters. This corresponds to a much  
 1057 lower baseline value<sup>65</sup> but is arguably a better encapsulation of the spatial heterogeneity  
 1058 in marine redox state. Nevertheless, the qualitative feedback sequence of “greenhouse  
 1059 gas injection, negative CIE, hyperthermal, elevated organic carbon burial and anoxia,  
 1060 recovery from perturbation via silicate weathering CO<sub>2</sub> sink” is robust to such changes in  
 1061 formulation, as is the sustained temperature increase.

1062 The δ<sup>13</sup>C record can either be evaluated in terms of simple mass balance calculations,  
 1063 used as an input to proxy inversion models, or a target at which that forward models aim

1064 via appropriate formulation of the underlying biogeochemical dynamics. We briefly  
1065 consider each of these approaches in turn.

1066

1067 **Qualitative description of feedback sequence corresponding to model results**

1068 The modelling illustrates that the basic feedback sequence resulting from the LIP-  
1069 associated CO<sub>2</sub> input is as follows: an increase in silicate weathering, leading to an  
1070 increase in the size of the marine phosphate reservoir, thus an increase in marine  
1071 production (increasing remineralization of organic carbon in the ocean, thus increasing  
1072 marine anoxia over a short timescale) and marine organic carbon burial (ultimately  
1073 increasing a long-term source of oxygen). The short-term increase in anoxia results in a  
1074 decrease (and eventual cessation) of Fe-adsorbed phosphate burial. This leads to a  
1075 secondary increase in the marine phosphate reservoir, which in the short-term boosts  
1076 production, therefore remineralization, therefore anoxia (i.e. a positive feedback), and in  
1077 the long term boosts marine organic carbon burial, therefore oxygen, therefore a  
1078 decrease in anoxia (a negative feedback).

1079 Because each of these processes operates over different timescales, predicting the  
1080 system's net response time is complex. Examples of the timescales over which various  
1081 fluxes and reservoirs respond to the greenhouse perturbation are given in Table S1,  
1082 which corresponds to a model run based on the same set of parameter choices as those  
1083 used to produce the results in the main text (see also **Table S10**). The peak of the CO<sub>2</sub>  
1084 perturbation shown corresponds to an estimated atmospheric CO<sub>2</sub> reservoir of  
1085 ~12.31PAL, which happens at 181.724 million years before present. The fall from this  
1086 maximum value corresponds to an *e*-folding time of:

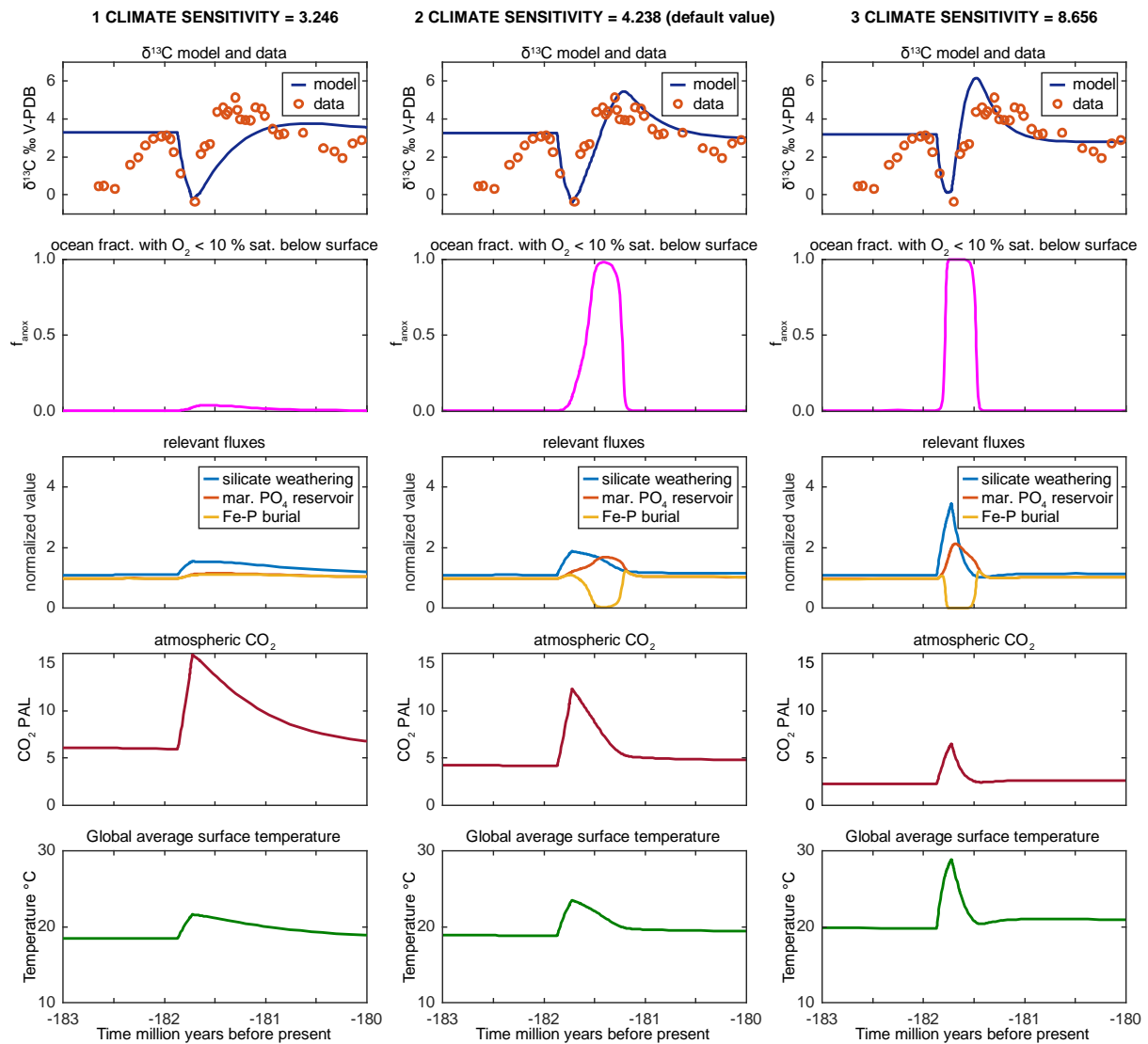
1087  $12.31 \cdot \left(1 - \frac{1}{e}\right) = 7.7814\text{PAL} \equiv 293\text{Kyr}$ .

1088 This is broadly in line with the error margin placed on the *e*-folding time of 170 –  
1089 340Kyr, probably ~240Kyr, estimated from more complex climate models<sup>66</sup>.

1090 The anoxia function responds within approximately 18kyrs to the increased nutrient  
1091 input, but the above-mentioned feedback involves a sharp decrease in Fe-adsorbed P  
1092 burial, which does not become significant until anoxia reaches roughly  $f_{anox} > 0.8$ . (The  
1093 asymptotic nature of Fe-P burial's response to anoxia is due to the fact that anoxia is a  
1094 logistic function that increases with increasingly P, but decreases with increasing O, and  
1095 is determined by the ratio of these two variables, both of which are increasing in size at  
1096 different rates). If the OAE is defined as the entire perturbation of  $f_{anox}$ , it lasts for

1097 approximately 565kyrs. If it is defined as the continuous interval of time during which  
 1098  $f_{\text{anox}} > 0.8$ , it lasts~266 kyr. This is shorter than (although within a reasonable  
 1099 “ballpark” estimate of) the~1.4Myr OAE duration that this model system produces<sup>64</sup> in  
 1100 the absence of a significant greenhouse perturbation – because the elevated nutrient  
 1101 input associated with the temperature/ CO<sub>2</sub> pushes the system through the above-  
 1102 mentioned feedback sequence at a faster rate than would occur at, for example, 1PAL CO<sub>2</sub>.  
 1103 It is important to note that the numbers quoted here, and shown in the table, are subject  
 1104 to an error margin dictated by uncertainty in parameter choices, which in this case have  
 1105 been selected so as to most accurately reproduce the carbon isotope data. This is  
 1106 illustrated by the sensitivity analysis depicted in **Figure S13**, which shows different  
 1107 values for the climate sensitivity parameter  $k_c$ .

1108



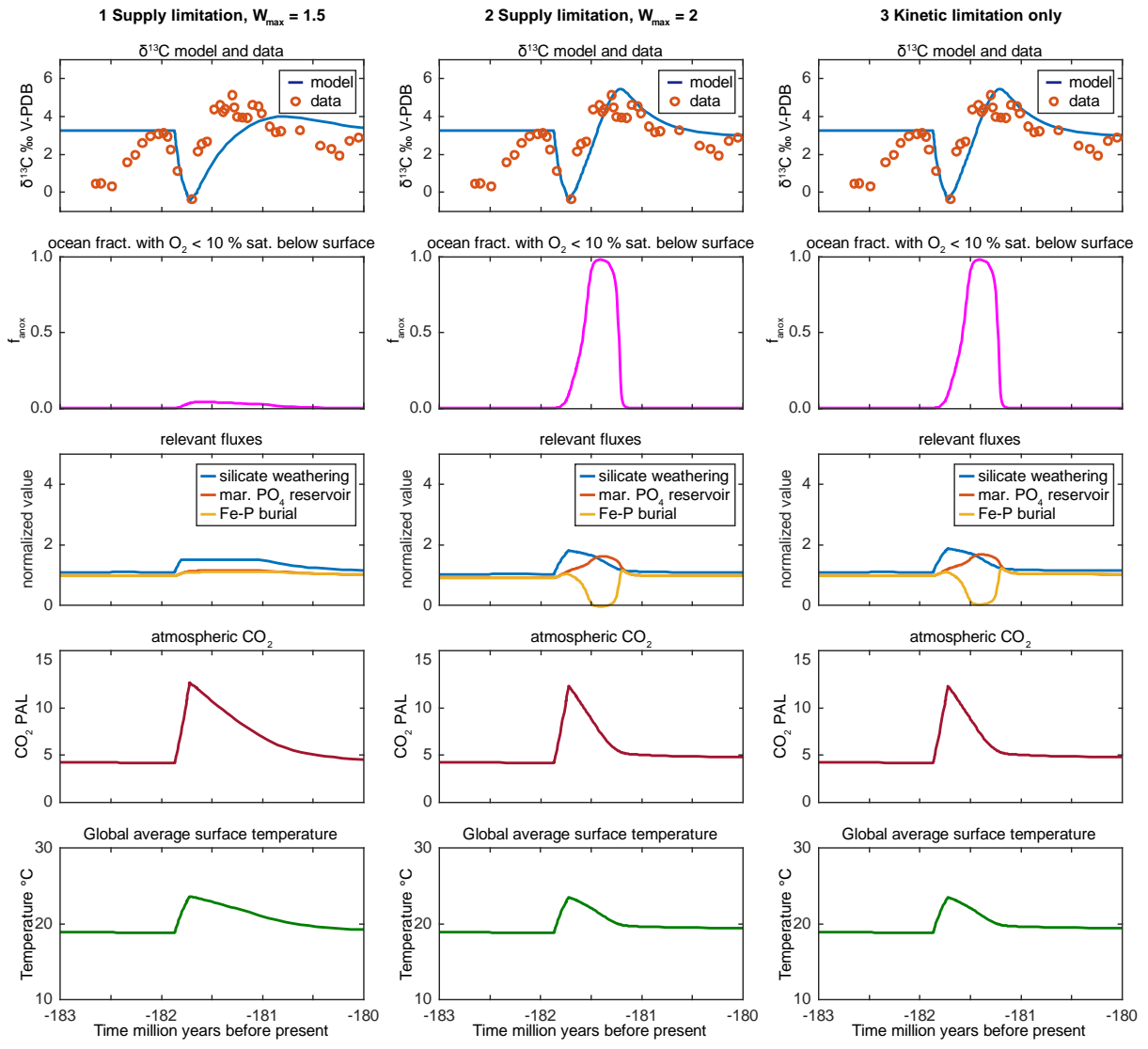
1109

1110 **Figure S13:** Model response as a function of the climate sensitivity parameter.

1111 Model temperature is of the form  $T = T_L + k_c \log(\frac{CO_2}{CO_{20}})$ , where  $T_L$  describes the increase  
1112 in temperature associated with the increase in solar luminosity over Earth's history,  
1113 whereas  $k_c$  represents temperature's sensitivity to log-normalized  $CO_{20}$ . The default  
1114 value  $k_c = 4.328$ , corresponds to the widely assumed climate sensitivity of  $4.328 \cdot$   
1115  $\log(2) \approx 3$  degrees warming per doubling of  $CO_2$ . Figure S1 illustrates the sensitivity of  
1116 the depicted feedback sequence to larger and smaller values of  $k_c$ , taken from the range  
1117 explored in the COPSE-reloaded model<sup>59</sup>. A larger value of  $k_c$  means that a smaller unit  
1118  $CO_2$  change will cause the same temperature change – meaning that the greenhouse  
1119 perturbation triggers the feedback sequence described more rapidly, and the overall  
1120 greenhouse gas change is lower. Similarly a smaller  $k_c$  requires a larger  $CO_2$  change to  
1121 initiate the feedback sequence, which is spread over a correspondingly larger timescale  
1122 (i.e. relative to the response times in **Table S11**).

1123 Based on previous discussion of the relationship between the silicate weathering and  
1124 OAE duration<sup>67</sup>, we investigated the idea of supply limitation of this flux. We find that the  
1125 best reproduction of the  $\delta^{13}C$  data is produced with a maximum kinetic limited silicate  
1126 weathering of around twice the modern value (i.e. such that silicate weathering becomes  
1127 supply limited rather than kinetically limited above this threshold). However, the difference,  
1128 in terms of reproducing the carbon isotope data, is slight relative to silicate  
1129 weathering that is solely kinetically limited (**Figure S14**), because the kinetically limited  
1130 flux does not significantly exceed this magnitude in any case. Furthermore, the threshold  
1131 at which supply limitation begins is highly uncertain, and a fair case can be made that it  
1132 is likely higher than twice the present value. We nevertheless retain the  $W_{max} = 2$   
1133 threshold (see model description), because it accurately reproduces the data. Some  
1134 limitation of terrestrial silicate weathering and its biotic enhancement may also be a  
1135 legitimate assumption based on previous arguments<sup>68</sup> for a link between enhanced fire  
1136 probability and repression of growth of the terrestrial biosphere during the Toarcian  
1137 event. In other words, our modelling is compatible with the idea that the silicate  
1138 weathering flux plateaued at about twice its present magnitude, which could have  
1139 occurred for a range of reasons.

1140



1141

1142

1143

**Figure S14:** Sensitivity study exploring the effects of the supply limitation threshold.

1144 **References**

- 1145 <sup>1</sup>Duarte, L.V., 2007. Lithostratigraphy, sequence stratigraphy and depositional setting of  
1146 the Pliensbachian and Toarcian series in the Lusitanian Basin, Portugal. Pp. 17–23 in  
1147 R. B. Rocha, ed. The Peniche section (Portugal). Contributions to the definition of the  
1148 Toarcian GSSP. International Subcommission on Jurassic Stratigraphy, Lisbon.
- 1149 <sup>2</sup>Pittet, B., Suan, G., Lenoir, F., Duarte, L.V., Mattioli, E., 2014. Carbon isotope evidence for  
1150 sedimentary discontinuities in the lower Toarcian of the Lusitanian Basin (Portugal):  
1151 Sea level change at the onset of the Oceanic Anoxic Event. *Sedimentary Geology* 303,  
1152 1–14. doi: 10.1016/j.sedgeo.2014.01.001.
- 1153 <sup>3</sup>Rodríguez-Tovar, F. J., Miguez-Salas, O., Duarte, L.V., 2017. Toarcian Oceanic Anoxic  
1154 Event induced unusual behaviour and palaeobiological changes in *Thalassinoides*  
1155 tracemakers. *Palaeogeography, Palaeoclimatology, Palaeoecology* 485, 46–56.
- 1156 <sup>4</sup>Piazza, V., Duarte, L.V., Renaudie, J., Aberhan, M., 2019. Reductions in body size of benthic  
1157 macroinvertebrates as a precursor of the early Toarcian (Early Juarssic) extinction  
1158 event in the Lusitanian Basin, Portugal. *Paleobiology* 45 (2), 296–316. doi:  
1159 10.1017/pab.2019.11.
- 1160 <sup>5</sup>Gómez, J. J., Goy, A., 2005. Late Triassic and Early Jurassic palaeogeographic evolution  
1161 and depositional cycles of the Western Tethys Iberian platform system (Eastern  
1162 Spain). *Palaeogeography, Palaeoclimatology, Palaeoecology* 222, 77–94.
- 1163 <sup>6</sup>Goy, A., Gómez, J.J., Yébenes, A., 1976. El Jurásico de la Rama Castellana de la Cordillera  
1164 Ibérica (Mitad Norte). I. Unidades litoestratigráficas 32, 391–423.
- 1165 <sup>7</sup>Gahr, M.E., 2002. Palökologie des Makrobenthos aus dem Unter-Toarc SW-Europas.  
1166 *Beringeria* 31, 3–204.
- 1167 <sup>8</sup>García Joral, F., Goy, A., 2010. Rhynchonellida (Brachiopoda) Biozones of the Toarcian in  
1168 the Iberian and Cantabrian Cordilleras (Spain). In: Comunicaciones del V Congreso del  
1169 Jurásico de España. Museo del Jurásico de Asturias (MUJA), Colunga, 8-11 de  
1170 septiembre de 2010 (J.I. Ruiz-Omeñaca, L. Piñuela & J.C. García-Ramos, Eds.). Museo  
1171 del Jurásico de Asturias, Colunga, 3–9.
- 1172 <sup>9</sup>Gahr, M.E., 2005. Response of Lower Toarcian (Lower Jurassic) macrobenthos of the  
1173 Iberian Peninsula to sea level changes and mass extinction. *Journal of Iberian Geology*  
1174 31, 197–215.
- 1175 <sup>10</sup>Fürsich, F.T., Berndt, R., Scheuer, T., Gahr, M., 2001. Comparative ecological analysis of  
1176 Toarcian (Lower Jurassic) benthic faunas from southern France and east-central  
1177 Spain. *Lethaia* 34, 169–199.
- 1178 <sup>11</sup>Aurell, M., Robles, S., Bádenas, B., Rosales, I., Quesada, S., Meléndez, G., García-Ramos,  
1179 J.C., 2003. Transgressive-regressive cycles and Jurassic palaeogeography of northeast  
1180 Iberia. *Sedimentary Geology* 162, 239–271.
- 1181 <sup>12</sup>Duarte, L.V., Soares, A.F., 2002. Litostratigraphy of the Lower Jurassic marly limestone  
1182 units from the Lusitanian Basin (Portugal). *Comun. Inst. Geol. e Mineiro* 89, 135–154.
- 1183 <sup>13</sup>Mouterde, R., Ruget, C., Moitinho de Almeida, F., 1964-1965. Coupe du Lias au Sud de  
1184 Condeixa. *Comunicações dos Serviços Geológicos de Portugal* 48, 61–91.
- 1185 <sup>14</sup>Comas-Rengifo, M. J., Duarte, L.V., García Joral, F., Goy, A., 2013. The brachiopod record  
1186 in the Lower Toarcian (Jurassic) of the Rabaçal - Condeixa region (Portugal):  
1187 stratigraphic distribution and palaeobiogeography. *Comunicações Geológicas* 100,  
1188 37–42.
- 1189 <sup>15</sup>Perilli, N., Duarte, L.V., 2006. Toarcian nannobiohorizons from Lusitanian Basin  
1190 (Portugal) and their calibration against ammonite zones. *Rivista Italiana di*  
1191 *Paleontologia e Stratigrafia* 112, 417–434.

- 1192 <sup>16</sup>Correia, V.D.P.F., 2018. Jurassic dinoflagellate cyst biostratigraphy of the Lusitanian  
1193 Basin, West-central Portugal, and its relevance to the opening of the North Atlantic and  
1194 petroleum geology, PhD thesis, Universidade do Algarve, 315pp.
- 1195 <sup>17</sup>Duarte, L.V., 1997. Facies analysis and sequential evolution of the Toarcian-Lower  
1196 Aalenian series in the Lusitanian Basin (Portugal). *Comunicações do Instituto*  
1197 *Geológico e Mineiro* 83, 65–94.
- 1198 <sup>18</sup>Duarte, L.V., Perilli, N., Dino, R., Rodrigues, R., Paredes, R., 2004. Lower to Middle  
1199 Toarcian from the Coimbra region (Lusitanian Basin, Portugal): sequence stratigraphy,  
1200 calcareous nannofossils and stable-isotope evolution. *Rivista Italiana di Paleontologia*  
1201 e Stratigrafia
- 1202 <sup>19</sup>Duarte, L.V., Oliveira, L.C., Rodrigues, R., 2007. Carbon isotopes as a sequence  
1203 stratigraphic tool: examples from the Lower to Middle Toarcian marly limestones of  
1204 Portugal. *Boletín Geológico y Minero* 118, 3–18.
- 1205 <sup>20</sup>Kullberg, J.C., Oloriz, F., Marques, B., Caetano, P.S., Rocha, R.B., 2001. Sedimentary  
1206 Geology 139, 49–70.
- 1207 <sup>21</sup>Röhl, H.-J., Schmidt-Röhl, A., Oschmann, W., Frimmel, A., Schwark, L., 2001. The  
1208 Posidonia Shale (Lower Toarcian) of SW-Germany: an oxygen-depleted ecosystem  
1209 controlled by sea level and palaeoclimate. *Palaeogeography, Palaeoclimatology,*  
1210 *Palaeoecology* 165, 27–52.
- 1211 <sup>22</sup>Wignall, P.B., Bond, D.P.G., 2008. The end-Triassic and Early Jurassic mass extinction  
1212 records in the British Isles. *Proceedings of the Geologists' Association* 119, 73–84.
- 1213 <sup>23</sup>Danise, S., Twitchett, R.J., Little, C.T.S., 2015. Environmental controls on Jurassic marine  
1214 ecosystems during global warming. *Geology* 43, 263–266.
- 1215 <sup>24</sup>Martindale, R.C., Aberhan, M., 2017. Response of microbenthic communities to the  
1216 Toarcian Oceanic Anoxic Event in northeastern Panthalassa (Ya Ha Tinda, Alberta,  
1217 Canada). *Paleogeography, Palaeoclimatology, Palaeoecology* 478, 103–120. doi:  
1218 10.1016/j.palaeo.2017.01.009.
- 1219 <sup>25</sup>Duarte, L.V., Rodrigues, R., Oliveira, L.C., Silva, F., 2005. Avaliação preliminar das  
1220 variações do carbono orgânico total nos sedimentos margosos do Jurássico inferior da  
1221 Bacia Lusitânica (Portugal). Pp. 39-43 in XIV Semana de Geoquímica and VIII  
1222 Congresso de Geoquímica dos Países de Língua Portuguesa, Aveiro, I.
- 1223 <sup>26</sup>García Joral, F., Gómez, J.J., Goy, A., 2011. Mass extinction and recovery of the Early  
1224 Toarcian (Early Jurassic) brachiopods linked to climate change in Northern and  
1225 Central Spain. *Palaeogeography, Palaeoclimatology, Palaeoecology* 302, 367–380.
- 1226 <sup>27</sup>Miguez-Salas, O., Rodríguez-Tovar, F.J., Duarte, L.V., 2017. Selective incidence of the  
1227 Toarcian oceanic anoxic event on macroinvertebrate marine communities: a case from  
1228 the Lusitanian basin, Portugal. *Lethaia* 50, 548–560.
- 1229 <sup>28</sup>Rodríguez-Tovar, F. J., Miguez-Salas, O., Dorador, J., Duarte, L.V., 2019. Opportunistic  
1230 behaviour after the Toarcian Oceanic Anoxic Event: The trace fossil *Halimedides*.  
1231 *Palaeogeography, Palaeoclimatology, Palaeoecology* 520, 240–256. Doi:  
1232 10.1016/j.palaeo.2019.01.036.
- 1233 <sup>29</sup>Canudo, J.I., 2018. The collection of type fossils of the Natural Science Museum of the  
1234 University of Zaragoza (Spain). *Geoheritage* 10 (3), 385–392. doi: 10.1007/s12371-  
1235 017-0228-1.
- 1236 <sup>30</sup>Imai N., Terashima S., Itoh S., Ando A., 1996. 1996 Compilation of analytical data on nine  
1237 GSJ geochemical reference samples, “sedimentary rock series”. *Geostandards*  
1238 *Newsletter* 20 (2), 165–216.
- 1239 <sup>31</sup>Govindaraju K., 1994. 1994 Compilation of working values and sample description for  
1240 383 geostandards. *Geostandards Newsletter* 18, 1–158.

- 1241   <sup>32</sup>Brand, U., Azmy, K., Bitner, M.A., Logan, A., Zuschin, M., Came, R., Ruggiero, E., 2013.  
1242   Oxygen isotopes and MgCO<sub>3</sub> in brachiopod calcite and a new paleotemperature  
1243   equation. *Chemical Geology* 359, 23–31. doi: 10.1016/j.chemgeo.2013.09.014.
- 1244   <sup>33</sup>Suan, G., Mattioli, E., Pittet, B., Mailliot, S., Lécuyer, C., 2008. Evidence for major  
1245   environmental perturbation prior to and during the Toarcian (Early Jurassic) oceanic  
1246   anoxic event from the Lusitanian Basin, Portugal. *Paleoceanography* 23, PA1202, doi:  
1247   10.1029/2007PA001459.
- 1248   <sup>34</sup>Ullmann, C.V., Böhm, F., Rickaby, R.E.M., Wiechert, U., Korte, C., 2013. The Giant Pacific  
1249   Oyster (*Crassostrea gigas*) as a modern analog for fossil ostreoids: Isotopic (Ca, O, C)  
1250   and elemental (Mg/Ca, Sr/Ca, Mn/Ca) proxies. *Geochemistry, Geophysics, Geosystems*  
1251   14 (10), 4109–4120. doi: 10.1002/ggge.20257.
- 1252   <sup>35</sup>Ullmann, C.V., Korte, C., 2015. Diagenetic alteration in low-Mg calcite from macrofossils:  
1253   a review. *Geological Quarterly* 59 (1), 3–20.
- 1254   <sup>36</sup>McConaughey, T., 1989. <sup>13</sup>C and <sup>18</sup>O isotopic disequilibrium in biological carbonates: I.  
1255   Patterns. *Geochimica et Cosmochimica Acta* 53, 151–162.
- 1256   <sup>37</sup>Wefer, G., Berger, W.H., 1991. Isotope paleontology: growth and composition of extant  
1257   calcareous species. *Marine Geology* 100, 207–248.
- 1258   <sup>38</sup>Ullmann, C.V., Frei, R., Korte, C., Lüter, C., 2017. Element/Ca, C and O isotope ratios in  
1259   modern brachiopods: Species-specific signals of biomineralisation. *Chemical Geology*  
1260   460, 15–24. doi: 10.1016/j.chemgeo.2017.03.034.
- 1261   <sup>39</sup>Anderson, T.F., Arthur, M.A., 1983. Stable isotopes of oxygen and carbon and their  
1262   application to sedimentologic and paleoenvironmental problems. In: Arthur, M.A.,  
1263   Anderson, T.F., Kaplan, I.R., Veizer, J., Land, L.S. (Eds.), *Stable Isotopes in Sedimentary*  
1264   *Geology*. SEPM, Dallas, Texas, pp. 1–151.
- 1265   <sup>40</sup>Jiménez-López, C., Romanek, C.S., Huertas, F.J., Ohmoto, H., Caballero, E., 2004. Oxygen  
1266   isotope fractionation in synthetic magnesian calcite. *Geochimica et Cosmochimica Acta*  
1267   68 (16), 3367–3377.
- 1268   <sup>41</sup>Gradstein, F.M., Ogg, J.G., Schmitz, M., Ogg, G. (eds.), 2012. *The geologic time scale 2012*.  
1269   elsevier.
- 1270   <sup>42</sup>Holser, W.T., Schidlowski, M., Mackenzie, F.T., Maynard, J.B., 1988. in *Chemical Cycles in*  
1271   *the Evolution of the Earth*, eds. Gregor, C. B., Garrels, R. M., Mackenzie, F. T. & Maynard,  
1272   J. B. (Wiley, New York), pp. 105–173.
- 1273   <sup>43</sup>Dickens, G.R., O'Neill, J.R., Rea, D.K., Owen, R.M., 1995. Dissociation of oceanic methane  
1274   as the cause of the carbon isotopic excursion at the end of the Paleocene.  
1275   *Paleoceanography* 10 (6), 965–971.
- 1276   <sup>44</sup>Hesselbo, S.P., Gröcke, D.R., Jenkyns, H.C., Bjerrum, C.J., Farrimond, P., Morgans Bell, H.S.,  
1277   Green, O.R., 2000. Massive dissociation of gas hydrate during an oceanic anoxic event.  
1278   *Nature* 406, 392–395.
- 1279   <sup>45</sup>Jiao, N., Herndl, G.J., Hansell, D.A., Benner R., Kattner G., Wilhelm, S.W., Kirchman, D.L.,  
1280   Weinbauer M.G., Luo, T., Chen, F., Azam, F., 2010. Microbial production of recalcitrant  
1281   dissolved organic matter: long-term carbon storage in the global ocean. *Nat. Rev. Microbiol.* 8, 593–599.
- 1282   <sup>46</sup>Kvenvolden, K.A., 2002. Methane Hydrate in the global carbon cycle. *Terra Nova* 14,  
1283   302–306.
- 1284   <sup>47</sup>Dunkley-Jones, T., Ridgwell, A., Lunt, D.J., Maslin, M.A., Schmidt, D.N., Valdes, P.J., 2010.  
1285   A Palaeogene perspective on climate sensitivity and methane hydrate instability. *Phil. Trans. R. Soc. A* 368, 2395–2415.

- 1288   <sup>48</sup>Jones, M.T., Jerram, D.A. Svensen, H.H., Grove, C., 2016. The effects of large igneous  
1289   provinces on the global carbon and sulphur cycles. *Paleogeography, Palaeoclimatology,*  
1290   *Palaeoecology* 441 4–21.
- 1291   <sup>49</sup>Beerling, D.J., Lomas, M.R., Gröcke, D.R., 2002. On the nature of methane gas hydrate  
1292   dissociation during the Toarcian and Aptian oceanic anoxic events. *Am. J. Sci.* 302, 28–  
1293   49.
- 1294   <sup>50</sup>Dera, G., Donnadieu, Y., 2012. Modeling evidences for global warming, Arctic seawater  
1295   freshening, and sluggish oceanic circulation during the Early Toarcian anoxic event.  
1296   *Paleoceanography* 27, PA2211. doi: 10.1029/2012PA002283.
- 1297   <sup>51</sup>Kump, L.R., Arthur, M.A., 1999. Interpreting carbon isotope excursions: carbonates and  
1298   organic matter. *Chem. Geol.* 161, 181–198.
- 1299   <sup>52</sup>Betts, R.A., Holland, H.D., 1991. The oxygen content of ocean bottom waters, the burial  
1300   efficiency of organic carbon, and the regulation of atmospheric oxygen.  
1301   *Palaeogeography, Palaeoclimatology, Palaeoecology* 97, 5–8.
- 1302   <sup>53</sup>Bergman, N.M., Lenton, T.M., Watson, A.J., 2004. COPSE: a new model of biogeochemical  
1303   cycling over Phanerozoic time. *Am. J. Sci.* 304, 397–437.
- 1304   <sup>54</sup>Berner, R.A., 1994. Geocarb II. A revised model of atmospheric CO<sub>2</sub> over geologic time.  
1305   *Am. J. Sci.* 294, 55–91.
- 1306   <sup>55</sup>Royer, D.L., Donnadieu, Y., Park, J., Kowalczyk, J. Godderis, Y., 2014. Error analysis of CO<sub>2</sub>  
1307   and O<sub>2</sub> estimates from the long-term geochemical model Geocarbsulf. *Am. J. Sci.* 314,  
1308   1259–1284.
- 1309   <sup>56</sup>Berner, R.A., 2006. Geocarbsulf: A combined model for Phanerozoic atmospheric O<sub>2</sub> and  
1310   CO<sub>2</sub>. *Geochimica et Cosmochimica Acta* 70 (23), 5653–5664.
- 1311   <sup>57</sup>Caldeira, K. & Kasting, J. F. 1992, The life span of the biosphere revisited: *Nature* 360,  
1312   721–723.
- 1313   <sup>58</sup>Mills, B.J.W., Watson, A.J., Goldblatt, C., Boyle, R.A., Lenton, T.M.L., 2011. Timing of  
1314   Neoproterozoic glaciations linked to transport-limited global weathering. *Nature*  
1315   *Geoscience* 4, 861–864.
- 1316   <sup>59</sup>Lenton, T.M., Daines, S.J., Mills, B.M., 2018. COPSE reloaded: An improved model of  
1317   biogeochemical cycling over Phanerozoic time. *Earth Sci. Rev* 178, 1–28.
- 1318   <sup>60</sup>Bond, W.J., Woodward, F.I., Midgley, G.F., 2005. The global distribution of ecosystems in  
1319   a world without fire. *New Phytol.* 165, 525–538.
- 1320   <sup>61</sup>Gill, B.C., Lyons, T.W., Jenkyns, H.C., 2011. A global perturbation to the sulphur cycle  
1321   during the Toarcian ocean. *Earth Plan. Sci. Lett.* 312, 484–496.
- 1322   <sup>62</sup>Cervantes, P., Wallace, P.J., 2003. Role of H<sub>2</sub>O in subduction-zone magmatism: New  
1323   insights from melt inclusions in high-Mg basalts from central Mexico. *Geology* 31, 235–  
1324   238.
- 1325   <sup>63</sup>Van Cappellen, P., Ingall, E.D. 1994. Benthic phosphorus Regeneration, primary  
1326   production, and ocean anoxia: A model of the coupled marine biogeochemical cycles  
1327   of carbon and phosphorus *Paleoceanography* 9, (5), 677–692.
- 1328   <sup>64</sup>Handoh, I.C., Lenton, T.M., 2003. Periodic mid-Cretaceous oceanic anoxic events linked  
1329   by oscillations of the phosphorus and oxygen biogeochemical cycles. *Global.*  
1330   *Biogeochem. Cycles.* 17 (4), 1092.
- 1331   <sup>65</sup>Helly, J.J., Levin, L.A., 2004. Global distribution of naturally occurring marine hypoxia on  
1332   continental margins. *Deep-Sea Res. I. Oceanogr. Res. Pap.* 51 (9), 1159–1168.
- 1333   <sup>66</sup>Colbourn, G., Ridgwell, A., Lenton, T.M., 2015. The timescale of the silicate weathering  
1334   negative feedback on atmospheric CO<sub>2</sub>. *Global Biogeochemical cycles* 29, 583–596.
- 1335   <sup>67</sup>Kump, L.R., 2013. Prolonged Late Permian–Early Triassic hyperthermal: A failure of  
1336   climate regulation? *Phil. Trans. R. Soc. A* 376: 20170078.

1337   <sup>68</sup>Baker, S.J., Hesselbo, S.P., Lenton, T.M., Duarte, L.V., Belcher, C.M. Charcoal evidence that  
1338       rising atmospheric oxygen terminated Early Jurassic ocean anoxia. Nat. Comm.  
1339       8:15018.

**Table S1:** Occurrences of macrofossils in the studied sections



**Table S2:** Analytical results for element-Ca standards measured alongside studied samples. Note that samples from Portugal were measured using a different batch of AK and BCQC and standard data therefore differ for these two stock solutions.

should bias %	Mg/Ca	Sr/Ca	Mn/Ca	Fe/Ca	S/Ca	P/Ca	Mg/Ca	Sr/Ca	Mn/Ca	Fe/Ca	S/Ca	P/Ca	Mg/Ca	Sr/Ca	Mn/Ca	Fe/Ca	S/Ca	P/Ca					
	mmol/mol	mmol/mol	mmol/mol	mmol/mol	mmol/mol	mmol/mol	mmol/mol	mmol/mol	mmol/mol	mmol/mol	mmol/mol	mmol/mol	mmol/mol	mmol/mol	mmol/mol	mmol/mol	mmol/mol	mmol/mol					
	avg	15.37	0.341	0.032	0.142	0.434	0.411	2.472	3.044	0.043	1.110	1.731	0.388	13.281	0.923	0.730	1.445	2.518	2.613				
	2ds	0.07	0.005	0.001	0.010	0.221	0.169	0.017	0.013	0.001	0.059	0.182	0.167	13.318	0.926	0.728	1.434	2.536	2.604				
	2rsd	0.46	1.40	2.8	7.2	51	41	0.67	0.44	2.2	5.3	11	43	0.59	0.97	0.43	0.91	9	4				
	n	72	72	72	72	72	72	48	48	48	48	48	48	24	24	24	24	24	24				
JLs-1	01/06/2018	15.412	0.343	0.031	0.150	0.337	0.544	AK	01/06/2018	2.481	3.052	0.042	1.078	1.645	0.265	BCQC	01/06/2018	13.270	0.926	0.728	1.428	2.652	2.646
JLs-1	01/06/2018	15.311	0.342	0.031	0.152	0.414	0.398	AK	01/06/2018	2.475	3.045	0.042	1.070	1.707	0.347	BCQC	01/06/2018	13.349	0.925	0.730	1.440	2.406	2.721
JLs-1	01/06/2018	15.362	0.343	0.031	0.150	0.565	0.549	AK	01/06/2018	2.470	3.044	0.042	1.074	1.640	0.468	BCQC	01/06/2018	13.323	0.925	0.727	1.429	2.572	2.615
JLs-1	01/06/2018	15.387	0.343	0.031	0.148	0.364	0.182	AK	01/06/2018	2.467	3.029	0.043	1.069	1.709	0.429	BCQC	01/06/2018	13.336	0.927	0.728	1.433	2.432	2.691
JLs-1	01/06/2018	15.407	0.343	0.031	0.152	0.432	0.484	AK	01/06/2018	2.473	3.041	0.042	1.069	1.750	0.369								
JLs-1	01/06/2018	15.389	0.343	0.032	0.148	0.480	0.347	AK	01/06/2018	2.478	3.041	0.043	1.069	1.721	0.376								
JLs-1	01/06/2018	15.383	0.343	0.032	0.143	0.520	0.326	AK	01/06/2018	2.480	3.050	0.043	1.076	1.615	0.366								
JLs-1	01/06/2018	15.386	0.342	0.032	0.142	0.496	0.498	AK	01/06/2018	2.472	3.032	0.043	1.066	1.746	0.418								
JLs-1	01/06/2018	15.382	0.343	0.032	0.143	0.364	0.431																
JLs-1	01/06/2018	15.388	0.343	0.032	0.146	0.484	0.425																
JLs-1	01/06/2018	15.437	0.343	0.032	0.142	0.573	0.369																
JLs-1	01/06/2018	15.401	0.343	0.031	0.143	0.404	0.294																
JLs-1	04/06/2018	15.458	0.344	0.032	0.147	0.414	0.323	AK	04/06/2018	2.487	3.064	0.042	1.088	1.857	0.240	BCQC	04/06/2018	13.347	0.927	0.727	1.432	2.451	2.570
JLs-1	04/06/2018	15.311	0.342	0.032	0.147	0.405	0.401	AK	04/06/2018	2.469	3.046	0.043	1.089	1.806	0.290	BCQC	04/06/2018	13.394	0.932	0.727	1.433	2.685	2.618
JLs-1	04/06/2018	15.355	0.342	0.032	0.147	0.518	0.393	AK	04/06/2018	2.471	3.051	0.043	1.089	1.696	0.465	BCQC	04/06/2018	13.350	0.928	0.728	1.436	2.630	2.642
JLs-1	04/06/2018	15.353	0.342	0.032	0.147	0.508	0.386	AK	04/06/2018	2.479	3.049	0.042	1.082	1.560	0.413	BCQC	04/06/2018	13.344	0.928	0.730	1.445	2.542	2.685
JLs-1	04/06/2018	15.407	0.343	0.032	0.143	0.434	0.413	AK	04/06/2018	2.474	3.042	0.043	1.087	1.786	0.482								
JLs-1	04/06/2018	15.353	0.342	0.032	0.144	0.428	0.372	AK	04/06/2018	2.469	3.047	0.042	1.095	1.788	0.552								
JLs-1	04/06/2018	15.345	0.341	0.032	0.151	0.396	0.446	AK	04/06/2018	2.478	3.048	0.042	1.088	1.746	0.452								
JLs-1	04/06/2018	15.362	0.342	0.032	0.150	0.550	0.384	AK	04/06/2018	2.478	3.056	0.043	1.086	1.688	0.561								
JLs-1	04/06/2018	15.350	0.342	0.031	0.152	0.689	0.465																
JLs-1	04/06/2018	15.376	0.342	0.031	0.152	0.336	0.462																
JLs-1	04/06/2018	15.343	0.341	0.032	0.149	0.398	0.501																
JLs-1	04/06/2018	15.366	0.342	0.032	0.151	0.308	0.342																
JLs-1	08/06/2018	15.407	0.342	0.032	0.146	0.328	0.162	AK	08/06/2018	2.473	3.044	0.044	1.094	1.753	0.457	BCQC	08/06/2018	13.295	0.927	0.728	1.428	2.475	2.513
JLs-1	08/06/2018	15.359	0.343	0.032	0.142	0.740	0.456	AK	08/06/2018	2.478	3.045	0.043	1.103	1.858	0.237	BCQC	08/06/2018	13.316	0.931	0.728	1.428	2.519	2.591
JLs-1	08/06/2018	15.395	0.342	0.032	0.139	0.573	0.527	AK	08/06/2018	2.480	3.050	0.042	1.098	1.854	0.375	BCQC	08/06/2018	13.317	0.930	0.727	1.426	2.660	2.636
JLs-1	08/06/2018	15.369	0.342	0.032	0.140	0.514	0.438	AK	08/06/2018	2.464	3.045	0.042	1.091	1.755	0.152	BCQC	08/06/2018	13.292	0.929	0.728	1.425	2.645	2.535
JLs-1	08/06/2018	15.393	0.343	0.032	0.143	0.519	0.417	AK	08/06/2018	2.474	3.037	0.043	1.090	1.590	0.470								



**Table S3:** Analytical results for isotope standards measured alongside the studied samples.

	date	$\delta^{13}\text{C}$ ‰ VPDB	$\delta^{18}\text{O}$ ‰ VPDB		date	% $\text{CaCO}_3$	$\delta^{13}\text{C}$ ‰ VPDB	$\delta^{18}\text{O}$ ‰ VPDB
n	179	0.06	0.14		80	97.1	0.09	0.33
2sd						1.5		
CAR	10/08/2018	2.10	-2.08	NCA	10/08/2018	97.2	-5.56	-21.98
CAR	10/08/2018	2.11	-1.99	NCA	10/08/2018	97.3	-5.59	-21.97
CAR	10/08/2018	2.11	-1.99	NCA	10/08/2018	97.7	-5.67	-22.02
CAR	10/08/2018	2.08	-2.03	NCA	10/08/2018	97.7	-5.58	-21.77
CAR	10/08/2018	2.11	-1.99	NCA	10/08/2018	97.8	-5.65	-22.01
CAR	10/08/2018	2.11	-2.15	NCA	10/08/2018	97.7	-5.64	-21.96
CAR	10/08/2018	2.12	-2.01	NCA	10/08/2018	97.8	-5.68	-21.83
CAR	10/08/2018	2.09	-2.02	NCA	10/08/2018	98.0	-5.68	-21.67
CAR	10/08/2018	2.08	-2.03					
CAR	10/08/2018	2.08	-1.96					
CAR	10/08/2018	2.16	-2.02					
CAR	10/08/2018	2.10	-2.08					
CAR	10/08/2018	2.08	-2.15					
CAR	10/08/2018	2.08	-1.94					
CAR	10/08/2018	2.14	-1.96					
CAR	10/08/2018	2.08	-2.06					
CAR	10/08/2018	2.10	-2.09					
CAR	10/08/2018	2.09	-1.99					
CAR	12/08/2018	2.13	-1.91	NCA	12/08/2018	96.7	-5.67	-22.11
CAR	12/08/2018	2.07	-2.15	NCA	12/08/2018	98.6	-5.62	-22.05
CAR	12/08/2018	2.12	-2.06	NCA	12/08/2018	96.1	-5.67	-21.87
CAR	12/08/2018	2.06	-2.04	NCA	12/08/2018	97.7	-5.55	-21.80
CAR	12/08/2018	2.12	-2.00	NCA	12/08/2018	98.2	-5.67	-22.00
CAR	12/08/2018	2.11	-2.01	NCA	12/08/2018	98.3	-5.65	-21.71
CAR	12/08/2018	2.14	-1.94	NCA	12/08/2018	98.2	-5.62	-21.73
CAR	12/08/2018	2.08	-2.07	NCA	12/08/2018	97.7	-5.59	-21.94
CAR	12/08/2018	2.10	-2.12					
CAR	12/08/2018	2.04	-2.08					
CAR	12/08/2018	2.08	-1.98					
CAR	12/08/2018	2.15	-1.99					
CAR	12/08/2018	2.18	-1.97					
CAR	12/08/2018	2.04	-2.07					
CAR	12/08/2018	2.05	-2.04					
CAR	12/08/2018	2.12	-2.05					
CAR	12/08/2018	2.11	-2.07					
CAR	12/08/2018	2.09	-1.99					
CAR	13/08/2018	2.09	-2.13	NCA	13/08/2018	96.0	-5.70	-22.22
CAR	13/08/2018	2.12	-1.92	NCA	13/08/2018	96.4	-5.62	-22.06
CAR	13/08/2018	2.10	-2.03	NCA	13/08/2018	97.0	-5.68	-21.96
CAR	13/08/2018	2.09	-2.01	NCA	13/08/2018	93.5	-5.62	-21.54
CAR	13/08/2018	2.12	-2.06	NCA	13/08/2018	96.9	-5.68	-22.16
CAR	13/08/2018	2.07	-2.09	NCA	13/08/2018	97.1	-5.56	-21.62
CAR	13/08/2018	2.13	-2.03	NCA	13/08/2018	96.8	-5.64	-22.03
CAR	13/08/2018	2.12	-1.94	NCA	13/08/2018	97.2	-5.53	-21.61
CAR	13/08/2018	2.07	-2.03					
CAR	13/08/2018	2.07	-2.13					
CAR	13/08/2018	2.13	-1.99					
CAR	13/08/2018	2.11	-1.95					
CAR	13/08/2018	2.08	-2.23					
CAR	13/08/2018	2.14	-1.92					
CAR	13/08/2018	2.07	-1.98					
CAR	13/08/2018	2.11	-2.07					
CAR	13/08/2018	2.10	-1.87					
CAR	13/08/2018	2.10	-2.17					
CAR	14/08/2018	2.09	-1.94	NCA	14/08/2018	97.2	-5.62	-22.08
CAR	14/08/2018	2.12	-2.11	NCA	14/08/2018	97.0	-5.67	-22.05
CAR	14/08/2018	2.07	-2.07	NCA	14/08/2018	97.6	-5.58	-21.87
CAR	14/08/2018	2.10	-2.07	NCA	14/08/2018	97.4	-5.69	-21.95
CAR	14/08/2018	2.16	-1.97	NCA	14/08/2018	97.6	-5.64	-21.82
CAR	14/08/2018	2.08	-1.88	NCA	14/08/2018	97.9	-5.63	-21.83
CAR	14/08/2018	2.05	-2.26	NCA	14/08/2018	97.5	-5.62	-21.80
CAR	14/08/2018	2.11	-2.02	NCA	14/08/2018	97.4	-5.59	-21.81
CAR	14/08/2018	2.07	-1.97					
CAR	14/08/2018	2.15	-1.97					
CAR	14/08/2018	2.07	-2.05					

CAR	14/08/2018	2.11	-2.04					
CAR	14/08/2018	2.08	-2.15					
CAR	14/08/2018	2.15	-1.88					
CAR	14/08/2018	2.06	-2.04					
CAR	14/08/2018	2.12	-2.05					
CAR	14/08/2018	2.10	-2.01					
CAR	14/08/2018	2.10	-2.04					
CAR	15/08/2018	2.11	-1.98	NCA	15/08/2018	95.7	-5.67	-22.10
CAR	15/08/2018	2.12	-2.07	NCA	15/08/2018	96.1	-5.58	-21.94
CAR	15/08/2018	2.07	-2.08	NCA	15/08/2018	96.9	-5.67	-22.16
CAR	15/08/2018	2.05	-2.03	NCA	15/08/2018	96.6	-5.63	-21.90
CAR	15/08/2018	2.17	-1.89	NCA	15/08/2018	95.9	-5.68	-21.76
CAR	15/08/2018	2.11	-2.10	NCA	15/08/2018	97.0	-5.49	-21.71
CAR	15/08/2018	2.12	-2.09	NCA	15/08/2018	97.0	-5.68	-21.82
CAR	15/08/2018	2.11	-1.96	NCA	15/08/2018	96.9	-5.65	-21.81
CAR	15/08/2018	2.09	-1.98					
CAR	15/08/2018	2.05	-2.17					
CAR	15/08/2018	2.03	-2.01					
CAR	15/08/2018	2.09	-1.97					
CAR	15/08/2018	2.19	-2.07					
CAR	15/08/2018	2.20	-1.99					
CAR	15/08/2018	2.04	-2.00					
CAR	15/08/2018	2.04	-2.08					
CAR	15/08/2018	2.09	-2.04					
CAR	15/08/2018	2.13	-2.02					
CAR	16/08/2018	2.07	-2.01	NCA	16/08/2018	96.4	-5.68	-22.17
CAR	16/08/2018	2.13	-2.04	NCA	16/08/2018	96.5	-5.65	-22.13
CAR	16/08/2018	2.10	-2.02	NCA	16/08/2018	97.6	-5.60	-21.90
CAR	16/08/2018	2.09	-2.09	NCA	16/08/2018	97.1	-5.59	-21.94
CAR	16/08/2018	2.10	-1.91	NCA	16/08/2018	97.1	-5.64	-21.87
CAR	16/08/2018	2.11	-2.10	NCA	16/08/2018	96.1	-5.61	-21.78
CAR	16/08/2018	2.12	-2.03	NCA	16/08/2018	97.5	-5.64	-21.72
CAR	16/08/2018	2.08	-2.04	NCA	16/08/2018	95.9	-5.62	-21.69
CAR	16/08/2018	2.09	-2.04					
CAR	16/08/2018	2.09	-2.01					
CAR	16/08/2018	2.12	-2.04					
CAR	16/08/2018	2.11	-2.10					
CAR	16/08/2018	2.01	-2.02					
CAR	16/08/2018	2.16	-1.94					
CAR	air leak							
CAR	16/08/2018	2.11	-2.06					
CAR	16/08/2018	2.07	-2.15					
CAR	16/08/2018	2.12	-1.91					
CAR	17/08/2018	2.09	-2.05	NCA	17/08/2018	96.8	-5.70	-22.18
CAR	17/08/2018	2.11	-2.00	NCA	17/08/2018	96.7	-5.69	-22.31
CAR	17/08/2018	2.08	-2.04	NCA	17/08/2018	97.5	-5.63	-21.91
CAR	17/08/2018	2.14	-2.02	NCA	17/08/2018	97.4	-5.60	-21.99
CAR	17/08/2018	2.03	-2.03	NCA	17/08/2018	97.0	-5.63	-21.68
CAR	17/08/2018	2.11	-2.09	NCA	17/08/2018	95.7	-5.61	-21.68
CAR	17/08/2018	2.11	-1.94	NCA	17/08/2018	97.6	-5.59	-21.82
CAR	17/08/2018	2.16	-2.00	NCA	17/08/2018	97.5	-5.59	-21.64
CAR	17/08/2018	2.10	-2.11					
CAR	17/08/2018	2.08	-2.03					
CAR	17/08/2018	2.10	-2.06					
CAR	17/08/2018	2.06	-2.02					
CAR	17/08/2018	2.10	-2.12					
CAR	17/08/2018	2.15	-1.86					
CAR	17/08/2018	2.07	-2.18					
CAR	17/08/2018	2.11	-1.94					
CAR	17/08/2018	2.10	-2.03					
CAR	17/08/2018	2.10	-2.03					
CAR	30/03/2019	2.08	-2.03	NCA	30/03/2019	96.1	-5.62	-22.04
CAR	30/03/2019	2.11	-2.04	NCA	30/03/2019	96.6	-5.60	-22.09
CAR	30/03/2019	2.09	-2.00	NCA	30/03/2019	97.7	-5.65	-21.87
CAR	30/03/2019	2.12	-2.03	NCA	30/03/2019	97.6	-5.68	-21.71
CAR	30/03/2019	2.12	-2.01	NCA	30/03/2019	97.9	-5.61	-21.88
CAR	30/03/2019	2.06	-2.09	NCA	30/03/2019	98.1	-5.60	-21.81
CAR	30/03/2019	2.11	-2.04	NCA	30/03/2019	97.0	-5.60	-21.91
CAR	30/03/2019	2.09	-2.00	NCA	30/03/2019	97.2	-5.68	-21.90
CAR	30/03/2019	2.11	-2.05					
CAR	30/03/2019	2.09	-2.01					

CAR	30/03/2019	2.14	-2.01					
CAR	30/03/2019	2.09	-2.04					
CAR	30/03/2019	2.06	-2.08					
CAR	30/03/2019	2.11	-1.99					
CAR	30/03/2019	2.08	-2.10					
CAR	30/03/2019	2.14	-1.96					
CAR	30/03/2019	2.09	-1.97					
CAR	30/03/2019	2.11	-2.08					
CAR	18/04/2019	2.08	-2.13	NCA	18/04/2019	98.0	-5.67	-22.05
CAR	18/04/2019	2.12	-1.95	NCA	18/04/2019	97.1	-5.63	-21.96
CAR	18/04/2019	2.12	-2.00	NCA	18/04/2019	97.5	-5.61	-22.03
CAR	18/04/2019	2.08	-1.93	NCA	18/04/2019	97.4	-5.63	-21.94
CAR	18/04/2019	2.08	-2.10	NCA	18/04/2019	97.6	-5.63	-21.85
CAR	18/04/2019	2.12	-2.19	NCA	18/04/2019	97.4	-5.64	-21.78
CAR	18/04/2019	2.09	-1.95	NCA	18/04/2019	97.9	-5.64	-21.83
CAR	18/04/2019	2.10	-2.03	NCA	18/04/2019	97.8	-5.60	-21.75
CAR	18/04/2019	2.08	-1.90					
CAR	18/04/2019	2.16	-2.03					
CAR	18/04/2019	2.00	-2.15					
CAR	18/04/2019	2.15	-1.96					
CAR	18/04/2019	2.07	-2.12					
CAR	18/04/2019	2.16	-2.06					
CAR	18/04/2019	2.10	-2.07					
CAR	18/04/2019	2.09	-1.87					
CAR	18/04/2019	2.05	-2.17					
CAR	18/04/2019	2.14	-1.94					
CAR	21/04/2019	2.08	-2.04	NCA	21/04/2019	97.4	-5.71	-22.15
CAR	21/04/2019	2.11	-2.00	NCA	21/04/2019	97.0	-5.71	-22.05
CAR	21/04/2019	2.13	-2.08	NCA	21/04/2019	97.5	-5.60	-22.02
CAR	21/04/2019	2.08	-2.04	NCA	21/04/2019	98.0	-5.64	-21.90
CAR	21/04/2019	2.06	-2.02	NCA	21/04/2019	97.5	-5.65	-22.00
CAR	21/04/2019	2.11	-1.94	NCA	21/04/2019	97.3	-5.62	-21.68
CAR	21/04/2019	2.10	-2.07	NCA	21/04/2019	97.9	-5.57	-21.81
CAR	21/04/2019	2.11	-2.04	NCA	21/04/2019	97.7	-5.55	-21.60
CAR	21/04/2019	2.10	-2.06					
CAR	21/04/2019	2.12	-2.04					
CAR	21/04/2019	2.10	-1.94					
CAR	21/04/2019	2.05	-2.09					
CAR	21/04/2019	2.11	-1.94					
CAR	21/04/2019	2.13	-2.09					
CAR	21/04/2019	2.12	-2.10					
CAR	21/04/2019	2.07	-2.01					
CAR	21/04/2019	2.06	-1.92					
CAR	21/04/2019	2.14	-2.12					

Table S4: Geochemical data acquired for fossils from Lower Toarcian sections in Spain and Portugal.

collection number	lab number	stratigraphy	sample ID	specimen number	species	type	description	prepared date	measured TE date	Ca wt%	Mg/Ca mmol/mol	Sr/Ca mmol/mol	Mn/Ca mmol/mol	Fe/Ca mmol/mol	S/Ca mmol/mol	P/Ca mmol/mol	measured ISO date	CaCO3 %	$\delta^{13}\text{C}$ ‰ VPDB	$\delta^{18}\text{O}$ ‰ VPDB	
MPZ 2019/482	CVU_carb_3831	Barranco de la Cañada	BC22	26.70	1	1	<i>Homoeorhynchia meridionalis</i>	brachiopod ventral	28/06/2018	06/07/2018	38.2	2.55	1.172	0.013	0.07	6.93	0.05	16/08/2018	96.9	3.06	-2.39
MPZ 2019/482	CVU_carb_3832	Barranco de la Cañada	BC22	26.70	1	1	<i>Homoeorhynchia meridionalis</i>	brachiopod ventral	28/06/2018	06/07/2018	38.2	2.37	1.168	0.012	0.05	6.62	0.02	16/08/2018	97.8	2.96	-2.16
MPZ 2019/482	CVU_carb_3833	Barranco de la Cañada	BC22	26.70	1	1	<i>Homoeorhynchia meridionalis</i>	brachiopod ventral	28/06/2018	06/07/2018	39.1	2.73	1.184	0.012	0.07	7.31	0.07	16/08/2018	97.5	3.00	-2.54
MPZ 2019/482	CVU_carb_3977	Barranco de la Cañada	BC22	26.70	1	1	<i>Homoeorhynchia meridionalis</i>	calcite cement	19/07/2018	02/08/2018	37.6	11.78	0.298	0.648	6.91	1.07	0.03	17/08/2018	99.6	1.86	-10.41
MPZ 2019/479	CVU_carb_3826	Barranco de la Cañada	BC21	25.55	2	1	<i>Homoeorhynchia meridionalis</i>	brachiopod	28/06/2018	06/07/2018	38.3	3.71	1.114	0.033	0.29	6.46	0.04	15/08/2018	98.0	2.73	-2.95
MPZ 2019/479	CVU_carb_3827	Barranco de la Cañada	BC21	25.55	2	1	<i>Homoeorhynchia meridionalis</i>	brachiopod	28/06/2018	06/07/2018	38.5	5.23	1.164	0.047	0.38	6.75	0.04	15/08/2018	98.7	2.74	-2.73
MPZ 2019/480	CVU_carb_3828	Barranco de la Cañada	BC21	25.55	2	2	<i>Homoeorhynchia meridionalis</i>	brachiopod	28/06/2018	06/07/2018	38.1	4.74	1.194	0.035	0.37	7.23	0.07	16/08/2018	96.2	2.60	-2.92
MPZ 2019/481	CVU_carb_3829	Barranco de la Cañada	BC21	25.55	2	3	<i>Homoeorhynchia meridionalis</i>	brachiopod	28/06/2018	06/07/2018	38.2	2.41	1.183	0.010	0.10	6.24	0.08	16/08/2018	96.0	2.66	-2.23
MPZ 2019/478	CVU_carb_3949	Barranco de la Cañada	BC21	25.55	1	1	<i>Homoeorhynchia meridionalis</i>	bulk rock	28/06/2018	06/07/2018	33.0	27.95	0.454	0.549	12.46	1.38	0.03	16/08/2018	85.4	2.06	-4.47
MPZ 2019/476	CVU_carb_3815	Barranco de la Cañada	BC20	24.55	2	1	<i>Homoeorhynchia meridionalis</i>	brachiopod	18/07/2018	02/08/2018	39.3	9.01	0.886	0.040	0.35	3.45	0.10	17/08/2018	100.4	3.04	-1.81
MPZ 2019/476	CVU_carb_3816	Barranco de la Cañada	BC20	24.55	2	1	<i>Homoeorhynchia meridionalis</i>	brachiopod	28/06/2018	06/07/2018	38.3	4.26	1.206	0.029	0.28	7.32	0.13	15/08/2018	97.6	2.58	-2.13
MPZ 2019/476	CVU_carb_3817	Barranco de la Cañada	BC20	24.55	2	1	<i>Homoeorhynchia meridionalis</i>	brachiopod	28/06/2018	06/07/2018	38.4	3.63	1.189	0.026	0.17	7.26	0.00	15/08/2018	97.3	2.68	-1.93
MPZ 2019/476	CVU_carb_3818	Barranco de la Cañada	BC20	24.55	2	1	<i>Homoeorhynchia meridionalis</i>	calcite cement	28/06/2018	06/07/2018	38.6	6.84	0.047	2.494	2.98	0.50	0.08	15/08/2018	99.9	1.46	-6.07
MPZ 2019/476	CVU_carb_3819	Barranco de la Cañada	BC20	24.55	2	1	<i>Homoeorhynchia meridionalis</i>	bulk rock	28/06/2018	06/07/2018	34.9	24.86	0.436	0.471	11.34	1.42	0.25	15/08/2018	90.6	1.99	-3.95
MPZ 2019/477	CVU_carb_3820	Barranco de la Cañada	BC20	24.55	2	2	<i>Homoeorhynchia meridionalis</i>	brachiopod	28/06/2018	06/07/2018	38.6	3.78	1.230	0.020	0.17	6.14	0.00	15/08/2018	98.6	2.62	-2.60
MPZ 2019/473	CVU_carb_3821	Barranco de la Cañada	BC20	24.55	1	1	<i>Homoeorhynchia meridionalis</i>	brachiopod	28/06/2018	06/07/2018	38.3	3.31	1.145	0.014	0.14	6.37	-0.05	15/08/2018	98.0	3.25	-2.03
MPZ 2019/473	CVU_carb_3822	Barranco de la Cañada	BC20	24.55	1	1	<i>Homoeorhynchia meridionalis</i>	bulk rock	28/06/2018	06/07/2018	38.2	3.66	1.095	0.30	0.30	6.86	0.01	15/08/2018	97.4	2.44	-2.02
MPZ 2019/474	CVU_carb_3823	Barranco de la Cañada	BC20	24.55	1	2	<i>Homoeorhynchia meridionalis</i>	brachiopod	28/06/2018	06/07/2018	38.4	3.63	1.189	0.026	0.17	7.26	0.00	15/08/2018	97.3	2.68	-1.93
MPZ 2019/474	CVU_carb_3824	Barranco de la Cañada	BC20	24.55	1	2	<i>Homoeorhynchia meridionalis</i>	calcite cement	28/06/2018	06/07/2018	38.6	6.84	0.047	2.494	2.98	0.50	0.08	15/08/2018	99.9	1.46	-6.07
MPZ 2019/475	CVU_carb_3825	Barranco de la Cañada	BC20	24.55	1	3	<i>Homoeorhynchia meridionalis</i>	bulk rock	28/06/2018	06/07/2018	34.9	24.86	0.436	0.471	11.34	1.42	0.25	15/08/2018	90.6	1.99	-3.95
MPZ 2019/472	CVU_carb_3751	Barranco de la Cañada	BC19	23.45	1	1	<i>Homoeorhynchia battleri</i>	brachiopod	28/06/2018	06/07/2018	37.9	8.93	1.157	0.090	0.19	5.58	0.05	15/08/2018	96.9	2.11	-2.58
MPZ 2019/472	CVU_carb_3752	Barranco de la Cañada	BC19	23.45	1	1	<i>Homoeorhynchia battleri</i>	brachiopod	17/06/2018	25/06/2018	38.2	3.39	1.200	0.019	0.19	7.54	0.04	15/08/2018	98.0	2.64	-2.52
MPZ 2019/472	CVU_carb_3753	Barranco de la Cañada	BC19	23.45	1	1	<i>Homoeorhynchia battleri</i>	brachiopod	17/06/2018	25/06/2018	38.3	7.90	1.239	0.035	0.44	7.69	0.09	15/08/2018	98.3	3.06	-1.99
MPZ 2019/472	CVU_carb_3754	Barranco de la Cañada	BC19	23.45	1	1	<i>Homoeorhynchia battleri</i>	bulk rock from fossil fill	17/06/2018	25/06/2018	32.7	26.76	0.614	25.31	1.16	1.79	0.03	15/08/2018	85.4	2.46	-3.16
MPZ 2019/471	CVU_carb_3755	Barranco de la Cañada	BC18	22.65	1	1	<i>Homoeorhynchia battleri</i>	brachiopod	17/06/2018	25/06/2018	38.2	6.68	1.006	0.140	0.97	4.72	0.06	15/08/2018	98.2	2.29	-3.07
MPZ 2019/471	CVU_carb_3756	Barranco de la Cañada	BC18	22.65	1	1	<i>Homoeorhynchia battleri</i>	brachiopod	17/06/2018	25/06/2018	38.3	5.67	1.167	0.090	0.39	4.93	-0.08	15/08/2018	97.6	2.26	-2.84
MPZ 2019/471	CVU_carb_3757	Barranco de la Cañada	BC18	22.65	1	1	<i>Homoeorhynchia battleri</i>	brachiopod	17/06/2018	25/06/2018	38.3	6.02	1.222	0.094	0.40	5.26	0.09	15/08/2018	98.8	2.16	-2.73
MPZ 2019/471	CVU_carb_3758	Barranco de la Cañada	BC18	22.65	1	1	<i>Homoeorhynchia battleri</i>	brachiopod	17/06/2018	25/06/2018	38.1	5.44	1.217	0.083	0.33	5.01	0.07	15/08/2018	97.9	2.49	-2.55
MPZ 2019/471	CVU_carb_3759	Barranco de la Cañada	BC18	22.65	1	1	<i>Homoeorhynchia battleri</i>	brachiopod	17/06/2018	25/06/2018	38.2	5.62	1.113	0.104	0.45	5.05	0.18	15/08/2018	97.5	2.33	-2.57
MPZ 2019/471	CVU_carb_3760	Barranco de la Cañada	BC18	22.65	1	1	<i>Homoeorhynchia battleri</i>	brachiopod	17/06/2018	25/06/20											

MPZ 2019/453	CVU_carb_3776	Barranco de la Cañada	BC08	16.05	2	1	<i>Homoeorhynchia batalleri</i>	brachiopod	ventral	17/06/2018	25/06/2018	38.4	4.14	1.059	0.097	0.28	3.00	0.14	15/08/2018	97.9	3.64	-2.23
MPZ 2019/453	CVU_carb_3777	Barranco de la Cañada	BC08	16.05	2	1	<i>Homoeorhynchia batalleri</i>	brachiopod	ventral	17/06/2018	25/06/2018	38.1	3.70	1.060	0.038	0.07	3.40	0.07	15/08/2018	98.9	3.76	-2.22
MPZ 2019/453	CVU_carb_3778	Barranco de la Cañada	BC08	16.05	2	1	<i>Homoeorhynchia batalleri</i>	brachiopod	dorsal	17/06/2018	25/06/2018	38.5	4.16	1.094	0.059	0.12	3.32	0.16	15/08/2018	98.8	3.16	-2.36
MPZ 2019/453	CVU_carb_3780	Barranco de la Cañada	BC08	16.05	2	1	<i>Homoeorhynchia batalleri</i>	brachiopod	dorsal	17/06/2018	25/06/2018	38.3	3.66	1.103	0.045	0.06	3.18	0.19	15/08/2018	99.3	3.70	-2.47
MPZ 2019/452	CVU_carb_3781	Barranco de la Cañada	BC08	16.05	1	1		bulk rock	bulk rock from fossil fill	17/06/2018	25/06/2018	34.2	26.15	0.543	0.672	20.59	3.02	26.79	15/08/2018	85.3	2.98	-3.66
MPZ 2019/449	CVU_carb_3430	Barranco de la Cañada	BC07	15.25	1	2	<i>Homoeorhynchia meridionalis</i>	brachiopod		10/04/2018	01/06/2018	38.1	3.42	1.019	0.045	0.34	2.42	0.13	10/08/2018	98.5	4.05	-2.59
MPZ 2019/448	CVU_carb_3688	Barranco de la Cañada	BC07	15.25	1	1	<i>Homoeorhynchia meridionalis</i>	brachiopod		08/06/2018	25/06/2018	38.6	6.20	0.981	0.121	0.69	3.37	0.16	14/08/2018	98.9	4.34	-2.38
MPZ 2019/448	CVU_carb_3689	Barranco de la Cañada	BC07	15.25	1	1	<i>Homoeorhynchia meridionalis</i>	brachiopod		08/06/2018	25/06/2018	38.4	6.35	0.984	0.133	0.71	3.56	0.19	14/08/2018	99.5	4.30	-2.70
MPZ 2019/448	CVU_carb_3690	Barranco de la Cañada	BC07	15.25	1	1	<i>Homoeorhynchia meridionalis</i>	brachiopod		08/06/2018	25/06/2018	38.7	4.27	0.932	0.135	0.42	3.19	0.10	14/08/2018	99.4	4.39	-2.73
MPZ 2019/448	CVU_carb_3691	Barranco de la Cañada	BC07	15.25	1	1	<i>Homoeorhynchia meridionalis</i>	brachiopod		08/06/2018	25/06/2018	30.1	31.55	0.460	0.762	22.96	0.97	0.94	14/08/2018	78.3	3.08	-4.06
MPZ 2019/449	CVU_carb_3692	Barranco de la Cañada	BC07	15.25	1	2	<i>Homoeorhynchia meridionalis</i>	brachiopod		08/06/2018	25/06/2018	38.8	4.17	0.982	0.070	0.29	2.70	0.13	14/08/2018	98.1	4.22	-2.81
MPZ 2019/449	CVU_carb_3693	Barranco de la Cañada	BC07	15.25	1	2	<i>Homoeorhynchia meridionalis</i>	brachiopod		08/06/2018	25/06/2018	38.7	4.39	0.965	0.096	0.60	2.80	-0.02	14/08/2018	99.2	4.27	-2.77
MPZ 2019/449	CVU_carb_3694	Barranco de la Cañada	BC07	15.25	1	2	<i>Homoeorhynchia meridionalis</i>	brachiopod		08/06/2018	25/06/2018	38.4	3.69	0.893	0.092	0.74	2.37	0.14	14/08/2018	98.0	4.17	-2.52
MPZ 2019/449	CVU_carb_3695	Barranco de la Cañada	BC07	15.25	1	2	<i>Homoeorhynchia meridionalis</i>	brachiopod		08/06/2018	25/06/2018	38.3	4.60	0.976	0.069	0.25	2.77	0.02	14/08/2018	99.1	3.97	-2.86
MPZ 2019/449	CVU_carb_3696	Barranco de la Cañada	BC07	15.25	1	2	<i>Homoeorhynchia meridionalis</i>	brachiopod		08/06/2018	25/06/2018	38.6	4.26	0.990	0.058	0.20	3.16	0.15	14/08/2018	99.6	4.25	-2.58
MPZ 2019/449	CVU_carb_3697	Barranco de la Cañada	BC07	15.25	1	2	<i>Homoeorhynchia meridionalis</i>	brachiopod		08/06/2018	25/06/2018	38.5	4.10	0.974	0.057	0.17	2.83	0.16	14/08/2018	98.6	4.20	-2.55
MPZ 2019/450	CVU_carb_3698	Barranco de la Cañada	BC07	15.25	1	3	<i>Homoeorhynchia meridionalis</i>	brachiopod		08/06/2018	25/06/2018	38.2	6.04	1.128	0.214	0.71	3.42	0.16	14/08/2018	98.2	3.87	-2.94
MPZ 2019/450	CVU_carb_3699	Barranco de la Cañada	BC07	15.25	1	3	<i>Homoeorhynchia meridionalis</i>	brachiopod		08/06/2018	25/06/2018	38.5	3.34	1.053	0.198	0.57	2.23	0.28	14/08/2018	98.9	4.38	-2.59
MPZ 2019/450	CVU_carb_3700	Barranco de la Cañada	BC07	15.25	1	3	<i>Homoeorhynchia meridionalis</i>	brachiopod		08/06/2018	25/06/2018	38.4	5.96	1.134	0.099	0.33	3.46	0.20	14/08/2018	99.1	4.22	-2.66
MPZ 2019/442	CVU_carb_3435	Barranco de la Cañada	BC06	14.85	1	1	<i>Gryphaea cf. dumortieri</i>	bivalve		10/04/2018	04/06/2018	39.0	3.14	0.882	0.051	0.37	0.94	0.05	10/08/2018	100.4	5.34	-2.53
MPZ 2019/443	CVU_carb_3512	Barranco de la Cañada	BC06	14.85	2	1	<i>Homoeorhynchia meridionalis</i>	brachiopod	ventral	02/05/2018	04/06/2018	38.5	3.82	0.935	0.044	0.33	2.58	0.12	12/08/2018	99.6	4.56	-3.22
MPZ 2019/443	CVU_carb_3513	Barranco de la Cañada	BC06	14.85	2	1	<i>Homoeorhynchia meridionalis</i>	brachiopod	ventral	02/05/2018	04/06/2018	38.2	6.02	1.060	0.034	0.15	3.62	0.24	12/08/2018	98.8	4.55	-2.98
MPZ 2019/443	CVU_carb_3514	Barranco de la Cañada	BC06	14.85	2	1	<i>Homoeorhynchia meridionalis</i>	brachiopod	ventral	02/05/2018	04/06/2018	38.2	4.18	0.988	0.029	0.12	3.07	0.17	12/08/2018	99.0	4.61	-3.16
MPZ 2019/443	CVU_carb_3515	Barranco de la Cañada	BC06	14.85	2	1	<i>Homoeorhynchia meridionalis</i>	bulk rock		02/05/2018	04/06/2018	32.2	26.51	0.452	0.691	16.60	1.21	1.05	12/08/2018	85.2	3.24	-4.35
MPZ 2019/444	CVU_carb_3516	Barranco de la Cañada	BC06	14.85	2	2	<i>Homoeorhynchia meridionalis</i>	brachiopod	dorsal	02/05/2018	04/06/2018	37.8	3.97	0.989	0.037	0.17	2.84	0.06	12/08/2018	99.2	4.46	-3.07
MPZ 2019/444	CVU_carb_3517	Barranco de la Cañada	BC06	14.85	2	2	<i>Homoeorhynchia meridionalis</i>	brachiopod	dorsal	02/05/2018	04/06/2018	38.3	3.90	1.025	0.023	0.10	3.10	0.22	12/08/2018	99.3	4.41	-3.23
MPZ 2019/444	CVU_carb_3518	Barranco de la Cañada	BC06	14.85	2	2	<i>Homoeorhynchia meridionalis</i>	brachiopod	dorsal	02/05/2018	04/06/2018	38.2	4.04	0.990	0.034	0.16	3.07	0.16	12/08/2018	100.0	4.34	-3.36
MPZ 2019/444	CVU_carb_3519	Barranco de la Cañada	BC06	14.85	2	2	<i>Homoeorhynchia meridionalis</i>	calcite cement		02/05/2018	04/06/2018	38.0	10.33	0.291	0.827	8.36	0.56	0.00	12/08/2018	97.6	2.24	-9.70
MPZ 2019/444	CVU_carb_3520	Barranco de la Cañada	BC06	14.85	2	2	<i>Homoeorhynchia meridionalis</i>	calcite cement		02/05/2018	04/06/2018	38.3	10.75	0.268	0.846	8.65	0.50	0.09	12/08/2018	99.6	2.28	-9.89
MPZ 2019/445	CVU_carb_3521	Barranco de la Cañada	BC06	14.85	2	3	<i>Homoeorhynchia meridionalis</i>	brachiopod	ventral	10/05/2018	04/06/2018	38.5	3.93	0.981	0.039	0.23	2.80	-0.				

MPZ 2019/425	CVU_carb_3447	Barranco de la Cañada	BC02	12.60	2	2	<i>Choffatirhynchia vasconcellosi</i>	brachiopod	ventral	28/04/2018	04/06/2018	38.4	5.69	0.973	0.085	0.38	2.73	0.11	10/08/2018	99.1	4.15	-1.91
MPZ 2019/425	CVU_carb_3448	Barranco de la Cañada	BC02	12.60	2	2	<i>Choffatirhynchia vasconcellosi</i>	brachiopod	ventral	28/04/2018	04/06/2018	38.4	4.48	0.890	0.068	0.29	2.52	0.04	10/08/2018	100.0	3.74	-1.98
MPZ 2019/425	CVU_carb_3449	Barranco de la Cañada	BC02	12.60	2	2	<i>Choffatirhynchia vasconcellosi</i>	brachiopod	ventral	28/04/2018	04/06/2018	38.6	4.27	0.828	0.094	0.47	2.01	0.10	10/08/2018	100.5	3.67	-2.10
MPZ 2019/425	CVU_carb_3450	Barranco de la Cañada	BC02	12.60	2	2	<i>Choffatirhynchia vasconcellosi</i>	brachiopod	dorsal	28/04/2018	04/06/2018	38.2	4.95	0.925	0.069	0.28	2.67	0.03	10/08/2018	98.7	4.10	-1.97
MPZ 2019/425	CVU_carb_3451	Barranco de la Cañada	BC02	12.60	2	2	<i>Choffatirhynchia vasconcellosi</i>	brachiopod	dorsal	28/04/2018	04/06/2018	39.1	3.79	0.792	0.094	0.47	1.98	0.07	10/08/2018	99.1	3.76	-1.88
MPZ 2019/425	CVU_carb_3452	Barranco de la Cañada	BC02	12.60	2	2	<i>Choffatirhynchia vasconcellosi</i>	brachiopod	dorsal	28/04/2018	04/06/2018	38.3	4.73	0.839	0.089	0.44	2.14	0.14	10/08/2018	99.7	3.85	-1.98
MPZ 2019/426	CVU_carb_3453	Barranco de la Cañada	BC02	12.60	2	3	<i>Choffatirhynchia vasconcellosi</i>	brachiopod	ventral	28/04/2018	04/06/2018	37.9	7.76	1.031	0.094	0.60	3.16	-0.10	10/08/2018	98.5	3.93	-1.47
MPZ 2019/426	CVU_carb_3454	Barranco de la Cañada	BC02	12.60	2	3	<i>Choffatirhynchia vasconcellosi</i>	brachiopod	ventral	28/04/2018	04/06/2018	38.2	6.86	1.030	0.065	0.33	3.09	0.05	10/08/2018	98.3	4.00	-1.55
MPZ 2019/426	CVU_carb_3455	Barranco de la Cañada	BC02	12.60	2	3	<i>Choffatirhynchia vasconcellosi</i>	brachiopod	ventral	28/04/2018	04/06/2018	38.2	8.44	0.984	0.108	0.84	3.53	0.01	10/08/2018	98.8	3.35	-2.09
MPZ 2019/426	CVU_carb_3456	Barranco de la Cañada	BC02	12.60	2	3	<i>Choffatirhynchia vasconcellosi</i>	brachiopod	dorsal	29/04/2018	04/06/2018	38.0	9.32	1.106	0.085	0.53	3.99	-0.01	10/08/2018	98.4	4.31	-1.60
MPZ 2019/426	CVU_carb_3457	Barranco de la Cañada	BC02	12.60	2	3	<i>Choffatirhynchia vasconcellosi</i>	brachiopod	dorsal	29/04/2018	04/06/2018	37.8	13.40	1.428	0.044	0.19	5.77	0.03	10/08/2018	98.1	4.22	-1.93
MPZ 2019/426	CVU_carb_3458	Barranco de la Cañada	BC02	12.60	2	3	<i>Choffatirhynchia vasconcellosi</i>	brachiopod	dorsal	29/04/2018	04/06/2018	38.5	11.63	1.098	0.117	0.69	4.13	-0.02	10/08/2018	99.8	4.09	-1.89
MPZ 2019/427	CVU_carb_3459	Barranco de la Cañada	BC02	12.60	2	4	<i>Choffatirhynchia vasconcellosi</i>	brachiopod	dorsal	29/04/2018	04/06/2018	38.0	6.84	0.926	0.076	0.38	3.86	0.10	10/08/2018	99.7	4.20	-2.07
MPZ 2019/427	CVU_carb_3460	Barranco de la Cañada	BC02	12.60	2	4	<i>Choffatirhynchia vasconcellosi</i>	brachiopod	dorsal	29/04/2018	04/06/2018	38.0	7.43	0.980	0.072	0.37	3.89	-0.02	10/08/2018	99.2	4.24	-1.71
MPZ 2019/427	CVU_carb_3461	Barranco de la Cañada	BC02	12.60	2	4	<i>Choffatirhynchia vasconcellosi</i>	brachiopod	dorsal	29/04/2018	04/06/2018	38.2	6.81	0.912	0.080	0.41	3.56	0.09	10/08/2018	99.1	4.13	-1.69
MPZ 2019/427	CVU_carb_3462	Barranco de la Cañada	BC02	12.60	2	4	<i>Choffatirhynchia vasconcellosi</i>	brachiopod	ventral	29/04/2018	04/06/2018	38.2	7.02	0.986	0.072	0.32	3.56	-0.03	10/08/2018	99.4	4.13	-2.10
MPZ 2019/427	CVU_carb_3463	Barranco de la Cañada	BC02	12.60	2	4	<i>Choffatirhynchia vasconcellosi</i>	brachiopod	ventral	29/04/2018	04/06/2018	38.0	8.46	1.257	0.035	0.14	3.80	0.04	10/08/2018	98.5	4.13	-1.38
MPZ 2019/427	CVU_carb_3464	Barranco de la Cañada	BC02	12.60	2	4	<i>Choffatirhynchia vasconcellosi</i>	brachiopod	ventral	29/04/2018	04/06/2018	38.2	6.79	0.881	0.083	0.39	3.30	0.06	10/08/2018	100.3	4.14	-1.57
MPZ 2019/428	CVU_carb_3465	Barranco de la Cañada	BC02	12.60	2	5	<i>Choffatirhynchia vasconcellosi</i>	brachiopod	ventral	29/04/2018	04/06/2018	38.3	5.91	0.944	0.105	1.01	2.98	0.15	10/08/2018	100.5	4.16	-1.78
MPZ 2019/428	CVU_carb_3466	Barranco de la Cañada	BC02	12.60	2	5	<i>Choffatirhynchia vasconcellosi</i>	brachiopod	ventral	29/04/2018	04/06/2018	38.2	6.17	0.944	0.089	0.98	3.14	0.10	10/08/2018	100.0	4.18	-1.71
MPZ 2019/428	CVU_carb_3467	Barranco de la Cañada	BC02	12.60	2	5	<i>Choffatirhynchia vasconcellosi</i>	brachiopod	ventral	29/04/2018	04/06/2018	38.1	6.37	0.989	0.063	0.55	3.12	-0.02	10/08/2018	99.1	4.22	-1.35
MPZ 2019/428	CVU_carb_3468	Barranco de la Cañada	BC02	12.60	2	5	<i>Choffatirhynchia vasconcellosi</i>	brachiopod	dorsal	29/04/2018	04/06/2018	38.5	6.03	0.935	0.087	0.71	3.13	0.22	10/08/2018	98.2	3.87	-1.87
MPZ 2019/428	CVU_carb_3469	Barranco de la Cañada	BC02	12.60	2	5	<i>Choffatirhynchia vasconcellosi</i>	brachiopod	dorsal	29/04/2018	04/06/2018	38.7	6.92	0.986	0.100	0.83	3.15	0.16	10/08/2018	99.6	3.69	-1.82
MPZ 2019/428	CVU_carb_3470	Barranco de la Cañada	BC02	12.60	2	5	<i>Choffatirhynchia vasconcellosi</i>	brachiopod	dorsal	29/04/2018	04/06/2018	38.3	6.55	0.930	0.085	0.65	2.65	0.18	10/08/2018	99.2	3.37	-1.93
MPZ 2019/429	CVU_carb_3560	Barranco de la Cañada	BC02	12.60	3	1	<i>Choffatirhynchia aff. paucicostata</i>	brachiopod	ventral	28/05/2018	08/06/2018	38.7	6.96	0.956	0.060	0.29	3.77	0.22	12/08/2018	99.1	3.87	-2.19
MPZ 2019/429	CVU_carb_3561	Barranco de la Cañada	BC02	12.60	3	1	<i>Choffatirhynchia aff. paucicostata</i>	brachiopod	ventral	28/05/2018	08/06/2018	38.3	6.89	0.959	0.060	0.30	3.96	0.19	12/08/2018	99.3	3.79	-2.01
MPZ 2019/429	CVU_carb_3562	Barranco de la Cañada	BC02	12.60	3	1	<i>Choffatirhynchia aff. paucicostata</i>	brachiopod	ventral	28/05/2018	08/06/2018	38.5	5.96	0.822	0.074	0.44	3.37	0.01	12/08/2018	100.6	3.90	-2.26
MPZ 2019/429	CVU_carb_3563	Barranco de la Cañada	BC02	12.60	3	1	<i>Choffatirhynchia aff. paucicostata</i>	brachiopod	dorsal	28/05/2018	08/06/2018	38.1	7.91	1.024	0.075	0.54	4.13	0.02	12/08/2018	99.1	4.11	-2.12
MPZ 2019/429	CVU_carb_3564	Barranco de la Cañada	BC02	12.60	3	1	<i>Choffatirhynchia aff. paucicostata</i>	brachiopod	dorsal	28/05/2018	08/06/2018	38.4	7.66	0.996	0.069	0.33	4.32	0.21	12/08/2018	99.8	4.07	-2.05
MPZ 2019/429	CVU_carb_3565	Barranco de la Cañada	BC02</td																			

MPZ 2019/566	CVU_carb_3766	Barranco de la Cañada	C33a	10.80	1	1		<i>Soaresirhynchia bouchardi</i>	bulk rock	bulk rock from fossil fill	17/06/2018	25/06/2018	34.5	24.59	0.381	0.358	10.55	0.71	0.50	15/08/2018	90.7	3.01	-2.74
MPZ 2019/564	CVU_carb_3706	Barranco de la Cañada	C30	10.20	1	1		<i>Soaresirhynchia bouchardi</i>	brachiopod		08/06/2018	25/06/2018	38.2	7.88	1.012	0.055	0.26	4.50	0.07	14/08/2018	98.8	4.72	-2.96
MPZ 2019/565	CVU_carb_3707	Barranco de la Cañada	C30	10.20	1	2		<i>Soaresirhynchia bouchardi</i>	brachiopod		08/06/2018	25/06/2018	38.3	6.07	0.917	0.060	0.33	3.62	-0.10	14/08/2018	99.3	4.18	-2.51
MPZ 2019/565	CVU_carb_3708	Barranco de la Cañada	C30	10.20	1	2		<i>Soaresirhynchia bouchardi</i>	brachiopod		08/06/2018	25/06/2018	37.9	7.10	0.898	0.066	0.60	3.70	-0.08	14/08/2018	89.8	4.25	-2.29
MPZ 2019/565	CVU_carb_3709	Barranco de la Cañada	C30	10.20	1	2		<i>Soaresirhynchia bouchardi</i>	bulk rock	bulk rock	08/06/2018	25/06/2018	33.9	23.16	0.413	0.417	12.16	0.93	0.42	14/08/2018	88.5	3.78	-3.79
MPZ 2019/557	CVU_carb_3533	Barranco de la Cañada	C28	9.40	1	1		<i>Soaresirhynchia bouchardi</i>	brachiopod	dorsal	24/05/2018	04/06/2018	39.4	3.60	0.524	0.026	0.20	1.58	0.02	12/08/2018	100.4	2.88	-2.98
MPZ 2019/557	CVU_carb_3534	Barranco de la Cañada	C28	9.40	1	1		<i>Soaresirhynchia bouchardi</i>	brachiopod	dorsal	24/05/2018	04/06/2018	39.1	3.71	0.534	0.027	0.25	1.68	0.03	12/08/2018	100.6	2.92	-2.78
MPZ 2019/557	CVU_carb_3535	Barranco de la Cañada	C28	9.40	1	1		<i>Soaresirhynchia bouchardi</i>	brachiopod	dorsal	24/05/2018	04/06/2018	39.2	3.28	0.524	0.016	0.17	1.65	0.25	12/08/2018	101.1	2.90	-2.85
MPZ 2019/557	CVU_carb_3536	Barranco de la Cañada	C28	9.40	1	1		<i>Soaresirhynchia bouchardi</i>	bulk rock	bulk rock	24/05/2018	04/06/2018	31.6	27.33	0.408	0.476	18.21	2.28	0.55	12/08/2018	80.4	2.01	-4.11
MPZ 2019/558	CVU_carb_3537	Barranco de la Cañada	C28	9.40	1	2		<i>Soaresirhynchia bouchardi</i>	brachiopod	ventral	24/05/2018	04/06/2018	39.4	2.95	0.614	0.037	0.29	1.45	-0.03	12/08/2018	100.3	2.63	-2.73
MPZ 2019/558	CVU_carb_3538	Barranco de la Cañada	C28	9.40	1	2		<i>Soaresirhynchia bouchardi</i>	brachiopod	ventral	24/05/2018	04/06/2018	39.2	2.21	0.525	0.026	0.20	1.21	0.12	12/08/2018	100.6	2.84	-2.67
MPZ 2019/558	CVU_carb_3539	Barranco de la Cañada	C28	9.40	1	2		<i>Soaresirhynchia bouchardi</i>	brachiopod	ventral	24/05/2018	04/06/2018	39.3	2.57	0.511	0.030	0.23	1.22	0.13	12/08/2018	100.9	2.87	-2.88
MPZ 2019/558	CVU_carb_3540	Barranco de la Cañada	C28	9.40	1	2		<i>Soaresirhynchia bouchardi</i>	brachiopod	dorsal	24/05/2018	04/06/2018	39.1	2.85	0.547	0.045	0.31	1.35	0.22	12/08/2018	101.1	2.66	-2.89
MPZ 2019/558	CVU_carb_3541	Barranco de la Cañada	C28	9.40	1	2		<i>Soaresirhynchia bouchardi</i>	brachiopod	calcite cement	24/05/2018	04/06/2018	38.5	13.70	0.344	0.651	7.76	0.78	0.14	12/08/2018	98.6	1.76	-8.63
MPZ 2019/559	CVU_carb_3542	Barranco de la Cañada	C28	9.40	1	3		<i>Soaresirhynchia bouchardi</i>	brachiopod	ventral	24/05/2018	04/06/2018	39.2	2.60	0.533	0.009	0.08	1.42	0.09	12/08/2018	100.3	2.76	-2.65
MPZ 2019/559	CVU_carb_3543	Barranco de la Cañada	C28	9.40	1	3		<i>Soaresirhynchia bouchardi</i>	brachiopod	ventral	24/05/2018	04/06/2018	39.4	2.47	0.544	0.010	0.08	1.24	0.09	12/08/2018	101.8	2.89	-2.53
MPZ 2019/559	CVU_carb_3544	Barranco de la Cañada	C28	9.40	1	3		<i>Soaresirhynchia bouchardi</i>	brachiopod	ventral	24/05/2018	04/06/2018	39.3	2.41	0.544	0.005	0.06	1.25	0.07	12/08/2018	101.6	2.82	-2.49
MPZ 2019/559	CVU_carb_3545	Barranco de la Cañada	C28	9.40	1	3		<i>Soaresirhynchia bouchardi</i>	brachiopod	dorsal	24/05/2018	04/06/2018	39.5	2.86	0.520	0.017	0.14	1.25	-0.08	12/08/2018	100.7	2.84	-2.70
MPZ 2019/559	CVU_carb_3546	Barranco de la Cañada	C28	9.40	1	3		<i>Soaresirhynchia bouchardi</i>	brachiopod	dorsal	24/05/2018	04/06/2018	39.1	2.87	0.536	0.010	0.06	1.39	0.02	12/08/2018	101.9	2.81	-2.51
MPZ 2019/559	CVU_carb_3547	Barranco de la Cañada	C28	9.40	1	3		<i>Soaresirhynchia bouchardi</i>	brachiopod	dorsal	24/05/2018	04/06/2018	39.3	2.85	0.533	0.013	0.10	1.04	0.06	12/08/2018	101.3	2.73	-2.79
MPZ 2019/560	CVU_carb_3548	Barranco de la Cañada	C28	9.40	1	4		<i>Soaresirhynchia bouchardi</i>	brachiopod	ventral	24/05/2018	04/06/2018	39.0	2.38	0.548	0.016	0.12	1.27	0.02	12/08/2018	97.4	2.59	-3.57
MPZ 2019/560	CVU_carb_3549	Barranco de la Cañada	C28	9.40	1	4		<i>Soaresirhynchia bouchardi</i>	brachiopod	ventral	24/05/2018	04/06/2018	39.0	2.83	0.534	0.008	0.04	1.45	0.03	12/08/2018	100.6	2.67	-3.52
MPZ 2019/560	CVU_carb_3550	Barranco de la Cañada	C28	9.40	1	4		<i>Soaresirhynchia bouchardi</i>	brachiopod	ventral	24/05/2018	04/06/2018	39.5	2.71	0.566	0.003	0.01	1.17	0.10	12/08/2018	100.3	2.68	-3.38
MPZ 2019/561	CVU_carb_3551	Barranco de la Cañada	C28	9.40	1	5		<i>Soaresirhynchia bouchardi</i>	brachiopod	ventral	28/05/2018	04/06/2018	38.9	2.34	0.542	0.056	0.45	1.19	-0.02	12/08/2018	100.9	2.36	-3.40
MPZ 2019/561	CVU_carb_3552	Barranco de la Cañada	C28	9.40	1	5		<i>Soaresirhynchia bouchardi</i>	brachiopod	ventral	28/05/2018	08/06/2018	39.6	2.37	0.511	0.027	0.21	1.19	0.18	12/08/2018	101.3	2.51	-3.16
MPZ 2019/561	CVU_carb_3553	Barranco de la Cañada	C28	9.40	1	5		<i>Soaresirhynchia bouchardi</i>	brachiopod	ventral	28/05/2018	08/06/2018	39.5	2.37	0.513	0.019	0.12	1.19	0.14	12/08/2018	100.5	2.50	-3.21
MPZ 2019/562	CVU_carb_3554	Barranco de la Cañada	C28	9.40	1	6		<i>Soaresirhynchia bouchardi</i>	brachiopod	ventral	28/05/2018	08/06/2018	39.4	2.12	0.524	0.009	0.06	1.18	0.10	12/08/2018	101.3	2.46	-2.84
MPZ 2019/562	CVU_carb_3555	Barranco de la Cañada	C28	9.40	1	6		<i>Soaresirhynchia bouchardi</i>	brachiopod	ventral	28/05/2018	08/06/2018	39.6	2.10	0.528	0.009	0.06	1.25	0.18	12/08/2018	101.6	2.54	-2.90
MPZ 2019/562	CVU_carb_3556	Barranco de la Cañada	C28	9.40	1	6		<i>Soaresirhynchia bouchardi</i>	brachiopod	dorsal	28/05/2018	08/06/2018	38.7	3.09	0.526	0.071	0.79	1.22	0.21	12/08/2018	101.4	2.33	-3.61
MPZ 2019/563	CVU_carb_3557	Barranco de la Cañada	C28	9.40	1	7</td																	

MPZ 2019/535	CVU_carb_3433	Barranco de la Cañada	C19	6.20	3	1	<i>Gryphaea (B.) sublobata</i>	bivalve	10/04/2018	04/06/2018	38.8	3.71	0.710	0.046	0.51	4.95	-0.02	10/08/2018	99.4	2.98	-2.18
MPZ 2019/538	CVU_carb_3616	Barranco de la Cañada	C19	6.20	4	1	<i>Quadratirhynchia attenuata</i>	brachiopod	04/06/2018	08/06/2018	38.2	4.60	0.951	0.025	0.21	5.08	0.20	13/08/2018	98.1	2.24	-2.70
MPZ 2019/538	CVU_carb_3617	Barranco de la Cañada	C19	6.20	4	1	<i>Quadratirhynchia attenuata</i>	brachiopod	04/06/2018	08/06/2018	38.5	4.55	1.001	0.016	0.16	4.79	0.10	13/08/2018	97.8	2.34	-2.49
MPZ 2019/538	CVU_carb_3618	Barranco de la Cañada	C19	6.20	4	1	<i>Quadratirhynchia attenuata</i>	brachiopod	04/06/2018	08/06/2018	38.5	5.20	1.033	0.016	0.19	6.12	0.15	13/08/2018	99.1	2.06	-2.51
MPZ 2019/538	CVU_carb_3619	Barranco de la Cañada	C19	6.20	4	1	<i>Quadratirhynchia attenuata</i>	brachiopod	04/06/2018	08/06/2018	38.3	6.06	0.983	0.043	0.56	5.54	0.13	13/08/2018	98.6	2.14	-2.61
MPZ 2019/538	CVU_carb_3620	Barranco de la Cañada	C19	6.20	4	1	<i>Quadratirhynchia attenuata</i>	brachiopod	04/06/2018	08/06/2018	36.0	5.46	0.960	0.038	0.40	5.53	0.18	13/08/2018	98.0	2.06	-2.76
MPZ 2019/538	CVU_carb_3621	Barranco de la Cañada	C19	6.20	4	1	<i>Quadratirhynchia attenuata</i>	brachiopod	04/06/2018	08/06/2018	38.4	5.22	0.989	0.031	0.32	5.21	0.17	13/08/2018	98.3	2.08	-2.49
MPZ 2019/533	CVU_carb_3804	Barranco de la Cañada	C19	6.20	2	1	<i>Tetrarhynchia subconcinna</i>	brachiopod	28/06/2018	06/07/2018	38.3	6.44	0.996	0.055	0.54	5.38	-0.02	15/08/2018	97.1	2.04	-2.61
MPZ 2019/533	CVU_carb_3805	Barranco de la Cañada	C19	6.20	2	1	<i>Tetrarhynchia subconcinna</i>	brachiopod	28/06/2018	06/07/2018	38.6	6.16	0.972	0.067	0.91	5.38	-0.02	15/08/2018	96.7	1.79	-2.73
MPZ 2019/533	CVU_carb_3806	Barranco de la Cañada	C19	6.20	2	1	<i>Tetrarhynchia subconcinna</i>	brachiopod	28/06/2018	06/07/2018	38.4	6.83	1.066	0.043	0.56	6.26	-0.01	15/08/2018	99.1	1.72	-2.53
MPZ 2019/533	CVU_carb_3807	Barranco de la Cañada	C19	6.20	2	1	<i>Gryphaea (B.) sublobata</i>	bivalve	29/06/2018	06/07/2018	38.9	3.47	0.715	0.044	0.61	5.62	-0.01	15/08/2018	52.8	1.30	-3.05
MPZ 2019/535	CVU_carb_3876	Barranco de la Cañada	C19	6.20	3	1	<i>Gryphaea (B.) sublobata</i>	bivalve	02/07/2018	06/07/2018	39.1	3.13	0.670	0.043	0.50	3.49	0.02	16/08/2018	99.3	2.86	-2.61
MPZ 2019/535	CVU_carb_3877	Barranco de la Cañada	C19	6.20	3	1	<i>Gryphaea (B.) sublobata</i>	bivalve	02/07/2018	06/07/2018	38.8	3.68	0.752	0.031	0.40	3.27	-0.07	16/08/2018	101.0	3.46	-2.06
MPZ 2019/536	CVU_carb_3879	Barranco de la Cañada	C19	6.20	3	2	<i>Gryphaea (B.) sublobata</i>	bivalve	02/07/2018	06/07/2018	38.9	2.86	0.707	0.022	0.27	5.93	0.11	16/08/2018	98.4	2.98	-2.57
MPZ 2019/536	CVU_carb_3880	Barranco de la Cañada	C19	6.20	3	2	<i>Gryphaea (B.) sublobata</i>	bivalve	02/07/2018	06/07/2018	39.0	2.96	0.719	0.024	0.28	6.04	0.05	16/08/2018	99.5	2.95	-2.25
MPZ 2019/536	CVU_carb_3881	Barranco de la Cañada	C19	6.20	3	2	<i>Gryphaea (B.) sublobata</i>	bivalve	02/07/2018	06/07/2018	38.8	3.82	0.746	0.017	0.21	6.20	-0.01	16/08/2018	100.3	3.10	-2.65
MPZ 2019/527	CVU_carb_3431	Barranco de la Cañada	C18c	5.90	1	3	<i>Quadratirhynchia aff. attenuata</i>	brachiopod	10/04/2018	01/06/2018	38.4	3.85	1.015	0.016	0.18	4.77	0.00	10/08/2018	98.7	2.44	-1.66
MPZ 2019/525	CVU_carb_3664	Barranco de la Cañada	C18c	5.90	1	1	<i>Quadratirhynchia aff. attenuata</i>	brachiopod	05/06/2018	08/06/2018	38.5	6.61	1.165	0.009	0.08	5.23	0.02	13/08/2018	98.6	2.46	-2.41
MPZ 2019/525	CVU_carb_3665	Barranco de la Cañada	C18c	5.90	1	1	<i>Quadratirhynchia aff. attenuata</i>	brachiopod	05/06/2018	08/06/2018	38.3	6.26	1.082	0.014	0.16	5.59	0.07	13/08/2018	98.9	2.63	-2.41
MPZ 2019/525	CVU_carb_3666	Barranco de la Cañada	C18c	5.90	1	1	<i>Quadratirhynchia aff. attenuata</i>	brachiopod	05/06/2018	08/06/2018	38.3	6.08	1.084	0.011	0.10	5.63	0.16	13/08/2018	98.2	2.74	-2.42
MPZ 2019/525	CVU_carb_3667	Barranco de la Cañada	C18c	5.90	1	1	<i>Quadratirhynchia aff. attenuata</i>	brachiopod	05/06/2018	08/06/2018	38.5	6.62	1.078	0.014	0.17	5.61	0.04	13/08/2018	99.4	2.54	-2.31
MPZ 2019/525	CVU_carb_3668	Barranco de la Cañada	C18c	5.90	1	1	<i>Quadratirhynchia aff. attenuata</i>	brachiopod	05/06/2018	08/06/2018	38.2	6.98	1.110	0.012	0.15	5.65	0.05	14/08/2018	96.6	2.68	-1.92
MPZ 2019/525	CVU_carb_3669	Barranco de la Cañada	C18c	5.90	1	1	<i>Quadratirhynchia aff. attenuata</i>	brachiopod	05/06/2018	08/06/2018	38.4	6.01	1.095	0.013	0.15	4.91	0.06	14/08/2018	97.9	2.59	-2.23
MPZ 2019/526	CVU_carb_3670	Barranco de la Cañada	C18c	5.90	1	2	<i>Quadratirhynchia aff. attenuata</i>	brachiopod	05/06/2018	08/06/2018	38.1	2.99	0.932	0.017	0.24	3.52	0.12	14/08/2018	98.6	3.30	-1.73
MPZ 2019/526	CVU_carb_3671	Barranco de la Cañada	C18c	5.90	1	2	<i>Quadratirhynchia aff. attenuata</i>	brachiopod	05/06/2018	08/06/2018	38.5	3.59	0.951	0.018	0.26	3.88	0.03	14/08/2018	99.4	3.46	-1.79
MPZ 2019/526	CVU_carb_3672	Barranco de la Cañada	C18c	5.90	1	2	<i>Quadratirhynchia aff. attenuata</i>	brachiopod	05/06/2018	25/06/2018	38.0	3.56	0.950	0.024	0.31	3.51	-0.03	14/08/2018	98.4	3.18	-1.89
MPZ 2019/527	CVU_carb_3673	Barranco de la Cañada	C18c	5.90	1	3	<i>Quadratirhynchia aff. attenuata</i>	brachiopod	05/06/2018	25/06/2018	37.9	4.39	1.038	0.016	0.16	4.72	0.02	14/08/2018	99.1	2.82	-1.62
MPZ 2019/527	CVU_carb_3674	Barranco de la Cañada	C18c	5.90	1	3	<i>Quadratirhynchia aff. attenuata</i>	brachiopod	05/06/2018	25/06/2018	38.1	4.85	1.033	0.017	0.16	4.97	0.00	14/08/2018	98.0	2.62	-2.42
MPZ 2019/527	CVU_carb_3675	Barranco de la Cañada	C18c	5.90	1	3	<i>Quadratirhynchia aff. attenuata</i>	brachiopod	05/06/2018	25/06/2018	38.1	4.64	1.038	0.012	0.11	5.10	-0.01	14/08/2018	99.1	2.96	-2.04
MPZ 2019/528	CVU_carb_3960	Barranco de la Cañada	C18c	5.90	2	1	<i>Gryphaea (B.) sublobata</i>	bivalve	19/07/2018	02/08/2018	38.5	3.57	0.701	0.050	0.75	4.23	0.14	17/08/2018	100.6	3.51	-1.76
MPZ 2019/528	CVU_carb_3961	Barranco de la Cañada	C18c	5.90	2	1	<i>Gryphaea (B.) sublobata</i>	bivalve	19/07/2018	02/08/2018	38.8	2.51	0.750	0.040							

MPZ 2019/504	CVU_carb_3883	Barranco de la Cañada	C12b	3.40	1	1	<i>Gryphaea (B.) sublobata</i>	bivalve	02/07/2018	06/07/2018	39.2	2.83	0.792	0.015	0.26	3.51	-0.07	16/08/2018	101.0	3.28	-1.86
MPZ 2019/504	CVU_carb_3884	Barranco de la Cañada	C12b	3.40	1	1	<i>Gryphaea (B.) sublobata</i>	bivalve	02/07/2018	06/07/2018	38.7	2.15	0.772	0.020	0.22	4.89	-0.07	16/08/2018	97.8	3.19	-1.69
MPZ 2019/505	CVU_carb_3885	Barranco de la Cañada	C12b	3.40	1	2	<i>Gryphaea (B.) sublobata</i>	bivalve	02/07/2018	06/07/2018	38.8	3.14	0.650	0.025	0.39	4.55	0.02	16/08/2018	99.6	1.91	-2.22
MPZ 2019/505	CVU_carb_3886	Barranco de la Cañada	C12b	3.40	1	2	<i>Gryphaea (B.) sublobata</i>	bivalve	02/07/2018	06/07/2018	38.6	3.56	0.656	0.039	0.51	5.82	-0.01	16/08/2018	100.4	1.82	-2.45
MPZ 2019/505	CVU_carb_3887	Barranco de la Cañada	C12b	3.40	1	2	<i>Gryphaea (B.) sublobata</i>	bivalve	02/07/2018	06/07/2018	38.6	3.09	0.645	0.031	0.36	4.57	0.06	16/08/2018	98.6	1.91	-2.36
MPZ 2019/505	CVU_carb_3888	Barranco de la Cañada	C12b	3.40	1	2	<i>Gryphaea (B.) sublobata</i>	bulk rock	02/07/2018	06/07/2018	30.4	32.00	0.263	0.429	18.22	1.56	1.51	16/08/2018	79.8	0.72	-2.94
MPZ 2019/498	CVU_carb_3432	Barranco de la Cañada	C12a	2.80	2	1	<i>Gryphaea (B.) sublobata</i>	bivalve	10/04/2018	04/06/2018	38.7	2.49	0.673	0.086	1.02	4.34	-0.04	10/08/2018	100.4	1.74	-2.23
MPZ 2019/502	CVU_carb_3502	Barranco de la Cañada	C12a	2.80	3	1	<i>Quadratirhynchia attenuata</i>	brachiopod	02/05/2018	04/06/2018	38.3	5.21	1.016	0.034	0.31	4.85	0.02	10/08/2018	98.6	1.48	-2.32
MPZ 2019/502	CVU_carb_3504	Barranco de la Cañada	C12a	2.80	3	1	<i>Quadratirhynchia attenuata</i>	brachiopod	02/05/2018	04/06/2018	38.4	5.25	1.077	0.014	0.13	4.50	0.03	10/08/2018	98.6	1.51	-2.12
MPZ 2019/502	CVU_carb_3505	Barranco de la Cañada	C12a	2.80	3	1	<i>Quadratirhynchia attenuata</i>	brachiopod	02/05/2018	04/06/2018	31.3	32.17	0.324	0.390	15.05	1.66	0.83	10/08/2018	82.3	0.57	-3.33
MPZ 2019/503	CVU_carb_3506	Barranco de la Cañada	C12a	2.80	3	2	<i>Quadratirhynchia attenuata</i>	brachiopod	02/05/2018	04/06/2018	38.4	4.96	0.917	0.044	0.29	3.67	0.07	10/08/2018	98.9	1.54	-2.39
MPZ 2019/503	CVU_carb_3507	Barranco de la Cañada	C12a	2.80	3	2	<i>Quadratirhynchia attenuata</i>	brachiopod	02/05/2018	04/06/2018	38.9	4.15	0.822	0.045	0.39	3.86	0.04	10/08/2018	100.4	1.45	-2.48
MPZ 2019/503	CVU_carb_3508	Barranco de la Cañada	C12a	2.80	3	2	<i>Quadratirhynchia attenuata</i>	brachiopod	02/05/2018	04/06/2018	38.4	5.49	0.862	0.058	0.42	3.45	0.09	12/08/2018	98.2	1.43	-2.64
MPZ 2019/503	CVU_carb_3509	Barranco de la Cañada	C12a	2.80	3	2	<i>Quadratirhynchia attenuata</i>	brachiopod	02/05/2018	04/06/2018	38.5	4.45	0.913	0.018	0.13	3.99	0.03	12/08/2018	97.5	1.53	-2.04
MPZ 2019/503	CVU_carb_3510	Barranco de la Cañada	C12a	2.80	3	2	<i>Quadratirhynchia attenuata</i>	brachiopod	02/05/2018	04/06/2018	38.8	4.53	0.889	0.023	0.17	3.70	0.06	12/08/2018	99.2	1.27	-2.25
MPZ 2019/503	CVU_carb_3511	Barranco de la Cañada	C12a	2.80	3	2	<i>Quadratirhynchia attenuata</i>	brachiopod	02/05/2018	04/06/2018	38.3	5.17	0.883	0.024	0.22	4.32	0.03	12/08/2018	98.4	1.30	-2.06
MPZ 2019/498	CVU_carb_3861	Barranco de la Cañada	C12a	2.80	2	1a	<i>Gryphaea (B.) sublobata</i>	bivalve	29/06/2018	06/07/2018	38.4	3.49	0.698	0.085	1.17	3.32	0.09	16/08/2018	99.6	2.08	-2.24
MPZ 2019/499	CVU_carb_3862	Barranco de la Cañada	C12a	2.80	2	1b	<i>Gryphaea (B.) sublobata</i>	bivalve	29/06/2018	06/07/2018	38.7	3.22	0.787	0.026	0.36	6.43	-0.04	16/08/2018	99.2	1.82	-2.23
MPZ 2019/499	CVU_carb_3863	Barranco de la Cañada	C12a	2.80	2	1b	<i>Gryphaea (B.) sublobata</i>	bivalve	29/06/2018	06/07/2018	38.5	2.47	0.808	0.035	0.56	3.11	0.05	16/08/2018	99.1	2.29	-2.02
MPZ 2019/500	CVU_carb_3864	Barranco de la Cañada	C12a	2.80	2	2	<i>Gryphaea (B.) sublobata</i>	bivalve	29/06/2018	06/07/2018	38.9	2.87	0.648	0.010	0.18	2.22	-0.06	16/08/2018	100.3	2.36	-1.60
MPZ 2019/500	CVU_carb_3865	Barranco de la Cañada	C12a	2.80	2	2	<i>Gryphaea (B.) sublobata</i>	bivalve	29/06/2018	06/07/2018	38.2	3.52	0.689	0.019	0.58	1.50	-0.05	16/08/2018	99.6	2.69	-1.30
MPZ 2019/500	CVU_carb_3866	Barranco de la Cañada	C12a	2.80	2	2	<i>Gryphaea (B.) sublobata</i>	bivalve	29/06/2018	06/07/2018	38.6	2.75	0.639	0.027	1.10	1.50	0.00	16/08/2018	97.8	2.58	-1.46
MPZ 2019/501	CVU_carb_3867	Barranco de la Cañada	C12a	2.80	2	3	<i>Gryphaea (B.) sublobata</i>	bivalve	29/06/2018	06/07/2018	38.8	1.54	0.815	0.023	0.34	2.92	0.01	16/08/2018	100.1	2.32	-1.85
MPZ 2019/501	CVU_carb_3868	Barranco de la Cañada	C12a	2.80	2	3	<i>Gryphaea (B.) sublobata</i>	bivalve	29/06/2018	06/07/2018	39.2	1.86	0.647	0.030	0.35	2.33	0.01	16/08/2018	99.9	2.25	-1.90
MPZ 2019/501	CVU_carb_3869	Barranco de la Cañada	C12a	2.80	2	3	<i>Gryphaea (B.) sublobata</i>	bivalve	29/06/2018	06/07/2018	38.6	1.79	0.860	0.026	0.39	2.90	0.04	16/08/2018	96.9	2.20	-1.81
MPZ 2019/493	CVU_carb_3917	Barranco de la Cañada	C07b	1.60	1	1	<i>Gryphaea (B.) sublobata</i>	bulk rock	06/07/2018	02/08/2018	29.1	33.83	0.272	0.454	21.80	1.36	0.68	17/08/2018	77.4	0.05	-2.96
MPZ 2019/494	CVU_carb_3918	Barranco de la Cañada	C07b	1.60	1	2	<i>Gryphaea (B.) sublobata</i>	bivalve	06/07/2018	02/08/2018	38.6	2.79	0.604	0.082	1.06	4.77	0.09	17/08/2018	100.0	0.72	-2.30
MPZ 2019/494	CVU_carb_3919	Barranco de la Cañada	C07b	1.60	1	2	<i>Gryphaea (B.) sublobata</i>	bivalve	06/07/2018	02/08/2018	38.3	2.44	0.735	0.024	0.39	2.46	0.12	17/08/2018	100.7	1.07	-1.76
MPZ 2019/494	CVU_carb_3920	Barranco de la Cañada	C07b	1.60	1	2	<i>Gryphaea (B.) sublobata</i>	bivalve	06/07/2018	02/08/2018	38.6	2.28	0.680	0.022	0.37	3.20	0.12	17/08/2018	100.7	0.83	-2.24
MPZ 2019/491	CVU_carb_3841	Barranco de la Cañada	C07a	0.80	1	1	<i>Gryphaea (B.) sublobata</i>	bivalve	29/06/2018	06/07/2018	37.9	6.55	0.637	0.031	0.86	3.17	0.12	16/08/2018	97.0	0.55	-1.84
MPZ 2019/491	CVU_carb_3842	Barranco de la Cañada	C07a	0.80	1	1	<i>Gryphaea (B.) sublobata</i>	bivalve	29/06/2018	06/07/2018	38.2	4.77	0.640	0.019	0.65	3.18					

MB.B.10891	CVU_carb_4895	Fonte Coberta / Rabacal	FC16e	14.80	1	1	<i>Soaresirhynchia bouchardi</i>	brachiopod	dorsal	08/04/2019	24/04/2019	97.0	2.68	0.485	0.013	0.068	1.58	0.21	21/04/2019	100.1	3.48	-2.46
MB.B.10891	CVU_carb_4896	Fonte Coberta / Rabacal	FC16e	14.80	1	1	<i>Soaresirhynchia bouchardi</i>	brachiopod	dorsal	08/04/2019	24/04/2019	97.1	2.61	0.485	0.014	0.079	1.67	0.05	21/04/2019	100.1	3.44	-2.56
MB.B.10891	CVU_carb_4897	Fonte Coberta / Rabacal	FC16e	14.80	1	1	<i>Soaresirhynchia bouchardi</i>	brachiopod	ventral	08/04/2019	24/04/2019	97.2	2.79	0.482	0.017	0.158	1.50	0.15	21/04/2019	101.0	3.33	-2.51
MB.B.10891	CVU_carb_4898	Fonte Coberta / Rabacal	FC16e	14.80	1	1	<i>Soaresirhynchia bouchardi</i>	brachiopod	ventral	08/04/2019	24/04/2019	96.5	3.07	0.503	0.022	0.327	1.83	0.12	21/04/2019	100.4	3.35	-2.47
MB.B.10891	CVU_carb_4899	Fonte Coberta / Rabacal	FC16e	14.80	1	1	<i>Soaresirhynchia bouchardi</i>	brachiopod	ventral	08/04/2019	24/04/2019	97.1	3.29	0.507	0.020	0.183	2.01	0.10	21/04/2019	100.3	3.38	-2.71
MB.B.10892	CVU_carb_4939	Fonte Coberta / Rabacal	FC16e	14.80	1	2		bulk rock		14/04/2019	24/04/2019	46.2	41.14	0.524	0.861	32.191	2.76	2.84	21/04/2019	47.0	0.96	-3.97
MB.B.10889	CVU_carb_4819	Fonte Coberta / Rabacal	FC16d	14.20	1	1	<i>Soaresirhynchia bouchardi</i>	brachiopod	ventral	25/03/2019	17/04/2019	97.8	3.47	0.529	0.009	0.074	1.90	0.22	30/03/2019	100.5	2.49	-2.49
MB.B.10889	CVU_carb_4820	Fonte Coberta / Rabacal	FC16d	14.20	1	1	<i>Soaresirhynchia bouchardi</i>	brachiopod	ventral	25/03/2019	17/04/2019	96.9	3.01	0.529	0.014	0.190	1.27	0.22	30/03/2019	99.8	2.42	-2.58
MB.B.10889	CVU_carb_4821	Fonte Coberta / Rabacal	FC16d	14.20	1	1	<i>Soaresirhynchia bouchardi</i>	brachiopod	ventral	25/03/2019	17/04/2019	97.0	4.68	0.593	0.011	0.092	2.22	0.21	30/03/2019	100.6	2.24	-2.59
MB.B.10890	CVU_carb_4822	Fonte Coberta / Rabacal	FC16d	14.20	1	2	<i>Soaresirhynchia bouchardi</i>	brachiopod	dorsal	25/03/2019	17/04/2019	97.4	3.30	0.499	0.030	0.366	1.62	0.07	30/03/2019	100.9	2.35	-2.58
MB.B.10890	CVU_carb_4823	Fonte Coberta / Rabacal	FC16d	14.20	1	2	<i>Soaresirhynchia bouchardi</i>	brachiopod	dorsal	25/03/2019	17/04/2019	97.4	2.86	0.491	0.014	0.146	1.27	0.22	30/03/2019	100.5	2.49	-2.55
MB.B.10890	CVU_carb_4824	Fonte Coberta / Rabacal	FC16d	14.20	1	2	<i>Soaresirhynchia bouchardi</i>	brachiopod	ventral	25/03/2019	17/04/2019	97.0	2.60	0.492	0.017	0.184	1.14	0.20	30/03/2019	100.1	2.46	-2.58
MB.B.10890	CVU_carb_4825	Fonte Coberta / Rabacal	FC16d	14.20	1	2	<i>Soaresirhynchia bouchardi</i>	brachiopod	ventral	25/03/2019	17/04/2019	97.0	2.59	0.485	0.014	0.120	1.46	0.06	30/03/2019	100.1	2.39	-2.61
MB.B.10889	CVU_carb_4948	Fonte Coberta / Rabacal	FC16d	14.20	1	1		bulk rock		14/04/2019	24/04/2019	70.7	28.73	0.465	0.493	19.028	1.95	1.03	21/04/2019	73.7	1.72	-4.18
MB.B.20343	CVU_carb_4928	Fonte Coberta / Rabacal	FC16e	13.75	1	1		bulk rock		14/04/2019	24/04/2019	57.0	28.98	0.913	0.425	13.630	2.09	1.77	21/04/2019	59.6	0.48	-4.15
MB.B.10885	CVU_carb_4878	Fonte Coberta / Rabacal	FC14c	7.30	1	1	<i>Nannirhynchia pygmaea</i>	brachiopod	ventral	07/04/2019	24/04/2019	92.5	1.92	0.499	0.031	0.237	1.43	0.22	18/04/2019	100.1	3.63	-1.60
MB.B.20341	CVU_carb_4906	Fonte Coberta / Rabacal	FC14c	7.30	2	2	<i>Harpax spinosa</i>	bivalve		12/04/2019	24/04/2019	95.7	11.43	0.894	0.153	0.792	3.57	0.26	21/04/2019	100.7	2.66	-1.94
MB.B.10885	CVU_carb_4930	Fonte Coberta / Rabacal	FC14c	7.30	1	1		bulk rock		14/04/2019	24/04/2019	68.1	27.30	0.727	0.508	19.642	1.79	1.01	21/04/2019	71.4	1.86	-3.85
MB.B.10882	CVU_carb_4885	Fonte Coberta / Rabacal	FC14b	6.90	1	1	<i>Nannirhynchia pygmaea</i>	brachiopod	ventral	08/04/2019	24/04/2019	97.6	2.09	0.568	0.018	0.053	1.77	0.18	18/04/2019	100.1	3.85	-1.55
MB.B.10882	CVU_carb_4886	Fonte Coberta / Rabacal	FC14b	6.90	1	1	<i>Nannirhynchia pygmaea</i>	brachiopod	dorsal	08/04/2019	24/04/2019	97.5	1.68	0.529	0.020	0.122	1.32	0.09	18/04/2019	100.6	3.91	-1.67
MB.B.10883	CVU_carb_4887	Fonte Coberta / Rabacal	FC14b	6.90	1	2	<i>Nannirhynchia pygmaea</i>	brachiopod	bulk rock	08/04/2019	24/04/2019	97.3	1.62	0.543	0.016	0.061	1.10	0.21	18/04/2019	100.3	3.79	-1.61
MB.B.10883	CVU_carb_4940	Fonte Coberta / Rabacal	FC14b	6.90	1	2		bulk rock		14/04/2019	24/04/2019	76.5	23.86	0.515	0.441	13.650	1.71	1.60	21/04/2019	78.9	2.03	-3.96
MB.B.10879	CVU_carb_4837	Fonte Coberta / Rabacal	FC13e	6.10	1	1	<i>Nannirhynchia pygmaea</i>	brachiopod	other	05/04/2019	24/04/2019	97.8	1.65	0.557	0.013	0.087	1.08	0.08	18/04/2019	97.2	4.21	-1.71
MB.B.10879	CVU_carb_4838	Fonte Coberta / Rabacal	FC13e	6.10	1	1	<i>Nannirhynchia pygmaea</i>	brachiopod	other	05/04/2019	24/04/2019	96.2	1.86	0.543	0.008	0.027	1.03	0.21	18/04/2019	100.3	4.30	-1.61
MB.B.10879	CVU_carb_4839	Fonte Coberta / Rabacal	FC13e	6.10	1	1	<i>Nannirhynchia pygmaea</i>	brachiopod	other	05/04/2019	24/04/2019	96.8	1.97	0.538	0.009	0.049	1.31	0.13	18/04/2019	98.6	4.22	-1.64
MB.B.10879	CVU_carb_4840	Fonte Coberta / Rabacal	FC13e	6.10	1	1	<i>Nannirhynchia pygmaea</i>	brachiopod	other	05/04/2019	24/04/2019	96.5	2.29	0.562	0.015	0.166	1.55	0.10	18/04/2019	100.2	4.35	-1.46
MB.B.10880	CVU_carb_4841	Fonte Coberta / Rabacal	FC13e	6.10	1	2	<i>Nannirhynchia pygmaea</i>	brachiopod	ventral	05/04/2019	24/04/2019	97.0	1.14	0.574	0.015	0.059	0.89	0.10	18/04/2019	100.4	4.30	-1.47
MB.B.10880	CVU_carb_4842	Fonte Coberta / Rabacal	FC13e	6.10	1	2	<i>Nannirhynchia pygmaea</i>	brachiopod	ventral	05/04/2019	24/04/2019	97.2	1.36	0.512	0.007	0.023	0.80	0.11	18/04/2019	100.2	4.39	-1.41
MB.B.10880	CVU_carb_4843	Fonte Coberta / Rabacal	FC13e	6.10	1	2	<i>Nannirhynchia pygmaea</i>	brachiopod	ventral	05/04/2019	24/04/2019	97.1	1.23	0.542	0.014	0.046	0.86	0.14	18/04/2019	99.5	4.36	-1.63
MB.B.10880	CVU_carb_4844	Fonte Coberta / Rabacal	FC13e	6.10	1	2	<i>Nannirhynchia pygmaea</i>	brachiopod	dorsal	05/04/2019	24/04/2019	97.8	1.68	0.538	0.024	0.237	0.97	0.19	18/04/2019	101.3	3.90	-2.11
MB.B.10881	CVU_carb_4845	Fonte Coberta																				

**Table S5:** Median isotopic variability in specimens of brachiopods from the two studied sections computed from specimens for which at least four measurements of well preserved shell calcite are available.

genus	locality	specimens number	median 2sd $\delta^{13}\text{C}$	median 2sd $\delta^{18}\text{O}$
<i>Choffatirhynchia</i>	Barranco de la Cañada	11	0.40	0.31
<i>Gibbirhynchia</i>	Barranco de la Cañada	2	0.41	0.49
<i>Homoeorhynchia</i>	Barranco de la Cañada	6	0.31	0.26
<i>Quadratirhynchia</i>	Barranco de la Cañada	3	0.23	0.39
<i>Soaresirhynchia</i>	Barranco de la Cañada	6	0.12	0.20
<i>Cirpa</i>	Fonte Coberta / Rabaçal	3	0.20	0.14
<i>Homoeorhynchia</i>	Fonte Coberta / Rabaçal	1	0.14	0.18
<i>Nannirhynchia</i> †	Fonte Coberta / Rabaçal	2	0.11	0.22
<i>Soaresirhynchia</i>	Fonte Coberta / Rabaçal	4	0.11	0.18

†: one doubtful datum (CVU\_carb\_4844) excluded

**Table S6:** Average  $\text{CaCO}_3$  concentrations, Mg/Ca and Sr/Ca ratios computed from well-preserved samples for individual rhynchonellid genera from the two studied sections.

genus	locality	samples number	average $\text{CaCO}_3$		average Mg/Ca		average Sr/Ca	
			% vs CAR	2 se	mmol/mol	2 se	mmol/mol	2 se
<i>Choffatirhynchia</i>	Barranco de la Cañada	74	99.1	0.2	6.63	0.31	0.994	0.024
<i>Gibbirhynchia</i>	Barranco de la Cañada	14	97.6	0.8	5.32	0.48	1.140	0.026
<i>Homoeorhynchia</i>	Barranco de la Cañada	91	98.7	0.2	4.82	0.30	1.084	0.020
<i>Quadratirhynchia</i>	Barranco de la Cañada	37 (36)	98.7	0.3	4.85	0.37	1.002	0.024
<i>Soaresirhynchia</i>	Barranco de la Cañada	100 (99)	100.3	0.2	2.63	0.10	0.533	0.006
<i>Cirpa</i>	Fonte Coberta / Rabaçal	22 (20)	99.9	0.5	2.08	0.21	0.506	0.011
<i>Homoeorhynchia</i>	Fonte Coberta / Rabaçal	4	99.1	0.6	5.49	0.66	0.948	0.021
<i>Nannirhynchia</i>	Fonte Coberta / Rabaçal	23 (22)	100.0	0.4	1.85	0.18	0.537	0.010
<i>Soaresirhynchia</i>	Fonte Coberta / Rabaçal	36	100.1	0.3	2.94	0.24	0.514	0.012

Samples numbers in brackets refer to numbers of samples from which average  $\text{CaCO}_3$  concentration was computed. Excluded samples deviated from averages by > 5 % and deviations are ascribed to erroneous weights.

**Table S7: Aggregated isotope data and calculated palaeotemperatures using the equations of Anderson and Arthur (1983) assuming seawater  $\delta^{18}\text{O}$  of -1 ‰ vs V-SMOW and Brand et al., (2013) additonally using the average magnesium content of 0.42 mol% in the macrofossil calcite. Ages are calculated from the Geologic Timescale 2012, assuming constant sedimentaiton rates within each ammonite zone.**

sample name	height m	n	$\delta^{13}\text{C}$ ‰ VPDB	2sd	2se	$\delta^{18}\text{O}$ ‰ VPDB	2sd	2se	T (B'13) °C	T (A'83) °C	Age (GT'12) Ma
BC22	26.70	3	3.14	0.10	0.06	-2.47	0.38	0.22	22.8	22.4	179.94
BC21	25.55	5	2.89	0.37	0.17	-2.54	0.86	0.38	23.0	22.7	180.05
BC20	24.55	9	2.72	0.52	0.17	-2.28	0.63	0.21	22.1	21.5	180.14
BC19	23.45	2	1.94	0.32	0.23	-2.47	0.01	0.01	22.7	22.4	180.24
BC18	22.65	3	2.30	0.34	0.20	-2.71	0.29	0.17	23.6	23.4	180.32
BC17	21.45	6	2.46	0.14	0.06	-2.07	0.17	0.07	21.4	20.6	180.43
BC14	19.35	11	3.27	0.57	0.17	-2.65	0.48	0.14	23.4	23.2	180.63
BC10	17.30	4	3.23	0.28	0.14	-2.50	0.44	0.22	22.9	22.5	180.82
BC09	16.70	2	3.17	0.13	0.09	-2.15	0.01	0.01	21.6	20.9	180.87
BC08	16.05	13	3.47	0.52	0.15	-2.57	0.62	0.17	23.1	22.8	180.93
BC07	15.25	8	4.17	0.21	0.07	-2.67	0.26	0.09	23.4	23.3	181.01
BC06	14.85	22	4.53	0.38	0.08	-2.75	0.67	0.14	23.7	23.7	181.04
BC05	14.25	4	4.61	0.12	0.06	-2.04	0.46	0.23	21.3	20.5	181.10
BC04	13.75	21	3.93	0.44	0.10	-1.75	0.67	0.15	20.3	19.2	181.15
BC03	13.20	13	3.95	0.67	0.19	-2.11	0.70	0.19	21.5	20.8	181.20
BC02	12.60	50	3.99	0.68	0.10	-1.91	0.67	0.10	20.8	19.9	181.25
BC01b	12.35	14	4.49	0.78	0.21	-2.60	0.96	0.26	23.2	23.0	181.28
BC01a	12.10	5	5.13	0.42	0.19	-2.34	0.11	0.05	22.3	21.8	181.30
C37a	11.30	8	4.39	0.30	0.11	-3.05	0.72	0.25	24.7	25.0	181.37
C33b	11.10	7	4.24	0.17	0.06	-3.00	0.48	0.18	24.6	24.8	181.39
C33a	10.80	4	4.60	0.28	0.14	-3.30	0.29	0.14	25.6	26.2	181.42
C30	10.20	3	4.38	0.59	0.34	-2.58	0.68	0.39	23.1	22.9	181.48
C28	9.40	25	2.69	0.35	0.07	-2.97	0.67	0.13	24.5	24.7	181.55
C26	8.90	21	2.56	0.55	0.12	-3.08	0.76	0.17	24.9	25.2	181.60
C25a	8.40	30	2.16	0.46	0.08	-3.26	0.36	0.07	25.5	26.0	181.64
C22	7.80	5	-0.36	0.23	0.10	-3.36	0.32	0.14	25.8	26.5	181.70
C20	6.70	2	1.13	0.10	0.07	-3.03	0.37	0.26	24.7	24.9	181.84
C19	6.20	16	2.26	0.63	0.16	-2.55	0.37	0.09	23.0	22.7	181.91
C18c	5.90	22	2.94	0.66	0.14	-1.88	0.73	0.15	20.7	19.7	181.94
C18b	5.60	17	3.13	0.53	0.13	-1.93	0.39	0.09	20.9	20.0	181.98
C18a	5.20	5	3.09	0.33	0.15	-2.01	0.43	0.19	21.1	20.3	182.03
C15b	4.60	2	2.97	0.24	0.17	-1.94	0.14	0.10	20.9	20.0	182.11
C15a	4.00	22	2.60	0.65	0.14	-2.21	0.59	0.13	21.8	21.2	182.19
C12b	3.40	6	1.98	1.39	0.57	-2.24	0.58	0.24	21.9	21.3	182.26
C12a	2.80	16	1.59	0.49	0.12	-2.13	0.59	0.15	21.6	20.8	182.34
C07b	1.60	2	0.32	0.34	0.24	-2.00	0.68	0.48	21.1	20.3	182.49
C07a	0.80	6	0.47	0.80	0.33	-2.11	0.77	0.31	21.5	20.8	182.60
C05	0.40	15	0.46	0.61	0.16	-1.95	0.55	0.14	20.9	20.0	182.65

**Table S8:** Quantities of Carbon required to explain T-OAE carbon isotope excursions.

	Amount of carbon required to generate negative isotopic excursion, GtC	$1 * M_{T0}$	$2 * M_{T0}$	$4 * M_{T0}$
Relative mass of ocean-atmosphere exchangeable carbon MT (pre-perterbation mass of total, combined organic and inorganic exchangeable carbon, relative to present $M_{T0} = M_{\text{inorganic}} + M_{\text{organic}} \cong 38,062 \text{ GtC}$ )				
$M_{\text{CH}_4}$ (clathrate)	$\delta^{13}\text{C}_{\text{CH}_4 \text{ hyd}} = -60 \text{ ‰}$	1765	3531	7062
$M_{\text{CO}_2}$ (thermogenic)	$\delta^{13}\text{C}_{\text{CO}_2 \text{ therm}} = -27 \text{ ‰}$	3943	7868	15737
$M_{\text{CH}_4}$ (thermogenic)	$\delta^{13}\text{C}_{\text{CH}_4 \text{ therm}} = -25 \text{ ‰}$ $\delta^{13}\text{C}_{\text{CH}_4 \text{ therm}} = -35 \text{ ‰}$	4251	8501	17003
$M_{\text{CO}_2}$ (magma)	$\delta^{13}\text{C}_{\text{CO}_2 \text{ magma}} = -5 \text{ ‰}$ $\delta^{13}\text{C}_{\text{CO}_2 \text{ magma}} = -7 \text{ ‰}$	21729	43457	86916
Total mass of organic carbon necessary to explain PCIE GtC		7476	14953	29907
Relative organic carbon burial flux x, where burial flux $= \int_0^{\Delta t_{data, PCIE}} m o c b_0 dt$		0.415	0.83	1.66

**Table S9:** Proxy Inversion model parameters

Abbreviation	Meaning	Baseline value/source
C	Carbonate carbon rock reservoir	$5.0 \times 10^{21}$ mol
G	Organic carbon rock reservoir	$1.5 \times 10^{21}$ mol
carbw	Carbonate weathering flux from land surface	$\text{carbw}_0 = 13.25 \times 10^{12} \text{ mol yr}^{-1}$
ccdeg	$\text{CO}_2$ degassing flux from the subduction of carbonate	$\text{ccdeg}_0 = 6.6 \times 10^{12} \text{ mol yr}^{-1}$ (COPSE)
ocdeg	$\text{CO}_2$ degassing flux from the subduction of organic carbon in rock	$\text{ocdeg}_0 = 1.25 \times 10^{12} \text{ mol yr}^{-1}$ (COPSE)
mccb	Marine carbonate carbon burial flux	$2.0 \times 10^{13}$ mol
mocb	Marine organic carbon burial flux	$\text{mocb}_0 = 3.75 \times 10^{12}$ mol
oxidw	Oxidative weathering flux of organic carbon in rock on the land surface	$\text{oxidw}_0 = 3.75 \times 10^{12} \text{ mol yr}^{-1}$
$\delta^{13}\text{C}_\text{C}$	Isotopic composition of carbonate carbon rock reservoir	$\delta_{\text{C}(0)} = 0$
$\delta^{13}\text{C}_\text{G}$	Isotopic composition of carbonate carbon rock reservoir	$\delta_{\text{G}(0)} = -\varepsilon = -24.5 \text{ ‰}$
$\delta^{13}\text{C}_{\text{mccb}}$	Isotopic composition of carbonates precipitating in shallow shelf ocean waters (assumed equilibrated with ocean-atmosphere $\text{CO}_2$ reservoir)	Model output, equated with data
$\varepsilon$	Difference between the isotopic composition of the marine organic carbon burial flux mocb and the marine carbonate carbon burial flux mccb. Expressed as a positive number $\varepsilon > 0$ , such the isotopic composition of organic matter being buried in shallow ocean sediments is $\delta^{13}\text{C}_{\text{org}} = \delta^{13}\text{C}_{\text{mccb}} - \varepsilon < 0$	
$F_{\text{LIP}}$	$\text{CO}_2$ release flux associated with large igneous province eruption.	$\int_{t_{\text{LIP start}}}^{t_{\text{LIP end}}} F_{\text{LIP}} dt \leq T_{\text{CO}_2 \text{ LIP}}$ , where $T_{\text{CO}_2 \text{ LIP}}$ is the total emission potential for the whole lifetime of the LIP, and $t_{\text{LIP start}} / t_{\text{LIP end}}$ are model parameters describing the time of onset/cessation of LIP associated $\text{CO}_2$ degassing (for most model runs shown, $t_{\text{LIP start}} \cdot t_{\text{LIP end}} = 0.45$ Myrs, tuned to match the NCIE). Constrained to be in the within the bounds $6.48 \times 10^{17} \text{ mol C} \leq T_{\text{CO}_2 \text{ LIP}} \leq 1.46 \times 10^{18} \text{ mol}$ $(\delta^{13}\text{C}_{\text{LIP}})_{\text{sun-volcanic}} = -5 \text{ ‰}$ (Cervantes & Wallace 2003) $-27 \text{ ‰} \leq (\delta^{13}\text{C}_{\text{LIP}})_{\text{thermogenic}} \leq +2 \text{ ‰}$ (Jones et al., 2016)
$\delta^{13}\text{C}_{\text{LIP}}$	Isotopic composition of large igneous province derived $\text{CO}_2$	
$F_{\text{CH}_4}$	$\text{CO}_2$ release flux associated with the oxidation of $\text{CH}_4$ produced during clathrate decomposition.	Parameterized, see text
$\delta^{13}\text{C}_{\text{CH}_4}$	Isotopic composition of $\text{CH}_4$ -clathrate	$\delta^{13}\text{C}_{\text{CH}_4} = -60 \text{ ‰}$ (Kvenvolden, 2002)
ESS	Long term Earth system sensitivity (temperature change per of atmospheric $\text{CO}_2$ )	ESS = 5 (Geocarbsulf)
$W_s$	Solar luminosity temperature dependence parameter	$W_s = 7.4$ (Geocarbsulf)
GEOG	Continental mean surface temperature (expressing change over time in GEOG(183 MA))	= 3 (Geocarbsulf)
ccdeg <sub>0</sub>	Baseline carbonate carbon degassing flux	$\text{ccdeg}_0 = 6.65 \times 10^{12} \text{ mol}$ (COPSE)
A	Total ocean-atmosphere $\text{CO}_2$ reservoir size	$A_0 = 3.193 \times 10^{18} \text{ mol}$ (COPSE)
$\varphi$	Atmospheric $\text{CO}_2$ fraction	Modern value $\varphi_0 = 2.8 \times 10^8 / (\text{mol}_{\text{atmos}} * A_0) = 0.0155$ (COPSE)
$\delta_C$	Average isotopic composition of global carbonate carbon rock reservoir	$\delta_{\text{C}(0)} = 0 \text{ ‰}$
$\delta_G$	Average isotopic composition of global organic carbon rock reservoir	$\delta_{\text{G}(0)} = -\varepsilon = -24.5 \text{ ‰}$
$f_{\text{anox}}$	Global ocean anoxic fraction	$f_{\text{anox}} = 0.14$
$\bar{P} = \frac{P\text{O}_4}{P\text{O}_4 \text{ }_0}$	Normalized, globally averaged marine phosphate concentration	$P\text{O}_4 \text{ }_0 = 2.2 \mu\text{mol kg}^{-1}$ (Redfield)
phosw	Phosphorous weathering flux from land surface	$\text{phosw}_0 = 3.675 \times 10^{10} \text{ mol yr}^{-1}$ $\text{phosw} = \text{phosw}_0 \left( f_{\text{silw}} \frac{\text{silw}}{\text{silw}_0} + f_{\text{carbw}} \frac{\text{carbw}}{\text{carbw}_0} + f_{\text{oxidw}} \frac{\text{oxidw}}{\text{oxidw}_0} \right)$
capb	Calcium bound marine phosphate burial	$\text{capb}_0 = 1.5 \times 10^{10} \text{ mol yr}^{-1}$
fepb	Iron absorbed phosphate burial	$\text{fepb}_0 = 0.6 \times 10^{10} \text{ mol yr}^{-1}$
mopb	Marine organic phosphorous burial	Scales with mocb as a function of anoxia via constants $\text{CP}_{\text{ox}} = 217 * \text{CP}_{\text{anox}} = 4320$ (Van Capellen & Ingall, 1994)

**Table S10: Example output for model run.**

-248.32	2.55	7.11E+12	0.0805	0	0.98	5.41E+09	3.53E+12	15.8
-248.29	2.55	7.10E+12	0.0796	0	0.98	5.41E+09	3.53E+12	15.8
-248.27	2.55	7.09E+12	0.0785	0	0.98	5.42E+09	3.52E+12	15.8
-248.23	2.54	7.07E+12	0.0761	0	0.98	5.42E+09	3.51E+12	15.8
-248.19	2.53	7.05E+12	0.0736	0	0.97	5.43E+09	3.50E+12	15.8
-248.15	2.53	7.04E+12	0.0712	0	0.97	5.44E+09	3.49E+12	15.8
-248.12	2.53	7.03E+12	0.0690	0	0.97	5.45E+09	3.48E+12	15.8
-248.08	2.52	7.02E+12	0.0670	0	0.97	5.45E+09	3.47E+12	15.8
-248.04	2.52	7.01E+12	0.0652	0	0.97	5.46E+09	3.46E+12	15.8
-247.98	2.52	7.00E+12	0.0627	0	0.97	5.46E+09	3.45E+12	15.8
-247.91	2.53	6.99E+12	0.0608	0	0.97	5.47E+09	3.44E+12	15.8
-247.85	2.53	6.99E+12	0.0591	0	0.97	5.48E+09	3.43E+12	15.8
-247.79	2.53	6.98E+12	0.0576	0	0.97	5.48E+09	3.42E+12	15.8
-247.73	2.54	6.98E+12	0.0563	0	0.97	5.49E+09	3.42E+12	15.8
-247.63	2.55	6.98E+12	0.0547	0	0.97	5.50E+09	3.41E+12	15.8
-247.54	2.55	6.99E+12	0.0534	0	0.97	5.51E+09	3.41E+12	15.8
-247.51	2.56	6.99E+12	0.0530	0	0.97	5.51E+09	3.41E+12	15.9
-247.48	2.56	7.28E+12	0.0526	0	0.97	5.51E+09	3.40E+12	15.9
-247.46	2.55	7.27E+12	0.0625	0	0.98	5.52E+09	3.49E+12	15.8
-247.43	2.55	7.26E+12	0.0670	0	0.98	5.53E+09	3.53E+12	15.8
-247.41	2.54	7.25E+12	0.0697	0	0.99	5.53E+09	3.55E+12	15.8
-247.39	2.54	7.23E+12	0.0707	0	0.99	5.53E+09	3.56E+12	15.8
-247.36	2.54	7.22E+12	0.0710	0	0.99	5.54E+09	3.57E+12	15.8
-247.34	2.53	7.21E+12	0.0707	0	0.99	5.54E+09	3.57E+12	15.8
-247.31	2.53	7.20E+12	0.0701	0	0.99	5.54E+09	3.57E+12	15.8
-247.29	2.52	7.19E+12	0.0693	0	0.99	5.55E+09	3.56E+12	15.8
-247.26	2.52	7.18E+12	0.0682	0	0.99	5.55E+09	3.56E+12	15.8
-247.24	2.52	7.17E+12	0.0670	0	0.99	5.55E+09	3.55E+12	15.8
-247.19	2.51	7.15E+12	0.0652	0	0.99	5.56E+09	3.54E+12	15.8
-247.15	2.51	7.14E+12	0.0636	0	0.99	5.56E+09	3.53E+12	15.8
-247.11	2.51	7.14E+12	0.0620	0	0.99	5.57E+09	3.52E+12	15.8
-247.07	2.51	7.13E+12	0.0606	0	0.99	5.57E+09	3.52E+12	15.8
-247.03	2.51	7.12E+12	0.0594	0	0.99	5.58E+09	3.51E+12	15.8
-246.96	2.51	7.12E+12	0.0575	0	0.98	5.58E+09	3.50E+12	15.8
-246.88	2.52	7.11E+12	0.0561	0	0.98	5.59E+09	3.49E+12	15.8
-246.81	2.52	7.11E+12	0.0549	0	0.98	5.59E+09	3.49E+12	15.8
-246.74	2.52	7.11E+12	0.0538	0	0.98	5.60E+09	3.48E+12	15.8
-246.66	2.53	7.11E+12	0.0529	0	0.98	5.60E+09	3.48E+12	15.8
-246.55	2.54	7.12E+12	0.0518	0	0.98	5.61E+09	3.48E+12	15.8
-246.52	2.54	7.12E+12	0.0514	0	0.98	5.61E+09	3.48E+12	15.8
-246.48	2.54	7.24E+12	0.0511	0	0.98	5.62E+09	3.47E+12	15.8
-246.45	2.54	7.23E+12	0.0574	0	0.99	5.63E+09	3.53E+12	15.8
-246.41	2.54	7.22E+12	0.0575	0	0.99	5.63E+09	3.54E+12	15.8
-246.38	2.54	7.22E+12	0.0569	0	0.99	5.63E+09	3.54E+12	15.8
-246.34	2.54	7.21E+12	0.0567	0	0.99	5.64E+09	3.54E+12	15.8
-246.31	2.54	7.20E+12	0.0560	0	0.99	5.64E+09	3.53E+12	15.8
-246.27	2.54	7.20E+12	0.0557	0	0.99	5.64E+09	3.53E+12	15.8
-246.23	2.54	7.19E+12	0.0548	0	0.99	5.65E+09	3.53E+12	15.8
-246.18	2.54	7.19E+12	0.0539	0	0.99	5.65E+09	3.52E+12	15.8
-246.14	2.54	7.19E+12	0.0532	0	0.99	5.65E+09	3.52E+12	15.8
-246.09	2.54	7.19E+12	0.0526	0	0.99	5.65E+09	3.52E+12	15.8
-246.02	2.54	7.18E+12	0.0516	0	0.99	5.66E+09	3.51E+12	15.8
-245.95	2.55	7.18E+12	0.0508	0	0.99	5.66E+09	3.51E+12	15.9
-245.87	2.55	7.18E+12	0.0501	0	0.99	5.67E+09	3.51E+12	15.9
-245.80	2.56	7.19E+12	0.0494	0	0.99	5.67E+09	3.50E+12	15.9
-245.69	2.56	7.19E+12	0.0485	0	0.99	5.68E+09	3.50E+12	15.9
-245.57	2.57	7.19E+12	0.0477	0	0.99	5.68E+09	3.50E+12	15.9
-245.45	2.58	7.18E+12	0.0470	0	0.99	5.69E+09	3.50E+12	15.9
-245.34	2.58	7.16E+12	0.0436	0	0.99	5.69E+09	3.47E+12	15.9
-245.22	2.58	7.17E+12	0.0436	0	0.99	5.70E+09	3.47E+12	15.9
-245.10	2.59	7.17E+12	0.0430	0	0.99	5.70E+09	3.47E+12	15.9
-244.99	2.60	7.18E+12	0.0424	0	0.99	5.71E+09	3.47E+12	15.9
-244.87	2.60	7.18E+12	0.0419	0	0.99	5.71E+09	3.47E+12	16.0
-244.75	2.61	7.18E+12	0.0413	0	0.99	5.72E+09	3.47E+12	16.0
-244.63	2.62	7.19E+12	0.0408	0	0.99	5.72E+09	3.47E+12	16.0
-244.51	2.62	7.19E+12	0.0403	0	0.99	5.73E+09	3.47E+12	16.0
-244.39	2.63	7.10E+12	0.0372	0	0.99	5.72E+09	3.44E+12	16.0
-244.29	2.65	7.12E+12	0.0353	0	0.99	5.72E+09	3.41E+12	16.0
-244.21	2.66	7.13E+12	0.0351	0	0.99	5.72E+09	3.41E+12	16.1
-244.13	2.67	7.15E+12	0.0354	0	0.99	5.73E+09	3.42E+12	16.1
-244.05	2.68	7.16E+12	0.0356	0	0.99	5.73E+09	3.43E+12	16.1
-243.97	2.68	7.17E+12	0.0356	0	0.99	5.73E+09	3.43E+12	16.1
-243.89	2.69	7.17E+12	0.0355	0	0.99	5.74E+09	3.43E+12	16.1
-243.81	2.69	7.18E+12	0.0354	0	0.99	5.74E+09	3.43E+12	16.1
-243.72	2.70	7.18E+12	0.0354	0	0.99	5.75E+09	3.44E+12	16.1
-243.64	2.70	7.19E+12	0.0351	0	0.99	5.75E+09	3.44E+12	16.1
-243.56	2.71	7.19E+12</						

-242.05	2.90	7.12E+12	0.0253	0	0.98	5.75E+09	3.33E+12	16.5
-241.98	2.91	7.13E+12	0.0254	0	0.98	5.75E+09	3.34E+12	16.5
-241.88	2.92	7.14E+12	0.0255	0	0.98	5.75E+09	3.34E+12	16.5
-241.78	2.93	7.15E+12	0.0255	0	0.98	5.76E+09	3.34E+12	16.5
-241.68	2.93	7.16E+12	0.0254	0	0.98	5.76E+09	3.35E+12	16.5
-241.58	2.94	7.16E+12	0.0253	0	0.98	5.77E+09	3.35E+12	16.5
-241.45	2.95	7.02E+12	0.0228	0	0.98	5.74E+09	3.30E+12	16.5
-241.36	2.96	7.04E+12	0.0212	0	0.97	5.73E+09	3.27E+12	16.6
-241.26	2.97	7.05E+12	0.0210	0	0.97	5.73E+09	3.27E+12	16.6
-241.17	2.98	7.07E+12	0.0213	0	0.97	5.74E+09	3.28E+12	16.6
-241.07	2.99	7.08E+12	0.0215	0	0.98	5.74E+09	3.29E+12	16.6
-240.97	3.00	7.09E+12	0.0215	0	0.98	5.75E+09	3.29E+12	16.6
-240.88	3.00	7.09E+12	0.0214	0	0.98	5.75E+09	3.29E+12	16.6
-240.77	3.01	7.10E+12	0.0213	0	0.98	5.75E+09	3.29E+12	16.6
-240.67	3.01	7.10E+12	0.0214	0	0.98	5.76E+09	3.29E+12	16.7
-240.57	3.02	7.11E+12	0.0212	0	0.98	5.76E+09	3.29E+12	16.7
-240.47	3.03	7.04E+12	0.0202	0	0.97	5.75E+09	3.27E+12	16.7
-240.37	3.04	7.05E+12	0.0194	0	0.97	5.74E+09	3.26E+12	16.7
-240.27	3.05	7.07E+12	0.0193	0	0.97	5.74E+09	3.26E+12	16.7
-240.17	3.06	7.08E+12	0.0195	0	0.97	5.75E+09	3.26E+12	16.7
-240.06	3.06	7.09E+12	0.0196	0	0.98	5.75E+09	3.27E+12	16.7
-239.95	3.07	7.09E+12	0.0195	0	0.98	5.76E+09	3.27E+12	16.7
-239.84	3.08	7.10E+12	0.0194	0	0.98	5.76E+09	3.27E+12	16.7
-239.72	3.08	7.10E+12	0.0193	0	0.98	5.76E+09	3.27E+12	16.8
-239.61	3.09	7.11E+12	0.0193	0	0.98	5.77E+09	3.27E+12	16.8
-239.44	3.09	7.16E+12	0.0199	0	0.98	5.78E+09	3.29E+12	16.8
-239.27	3.08	7.15E+12	0.0201	0	0.98	5.79E+09	3.30E+12	16.8
-239.10	3.08	7.15E+12	0.0197	0	0.98	5.79E+09	3.30E+12	16.8
-238.92	3.08	7.14E+12	0.0192	0	0.98	5.79E+09	3.29E+12	16.8
-238.75	3.08	7.14E+12	0.0190	0	0.98	5.79E+09	3.29E+12	16.8
-238.58	3.09	7.15E+12	0.0188	0	0.98	5.79E+09	3.29E+12	16.8
-238.43	3.08	7.34E+12	0.0215	0	0.99	5.84E+09	3.35E+12	16.8
-238.39	3.07	7.32E+12	0.0225	0	0.99	5.85E+09	3.38E+12	16.8
-238.35	3.06	7.31E+12	0.0229	0	1.00	5.86E+09	3.39E+12	16.7
-238.30	3.05	7.30E+12	0.0227	0	1.00	5.86E+09	3.38E+12	16.7
-238.26	3.04	7.28E+12	0.0224	0	1.00	5.85E+09	3.38E+12	16.7
-238.21	3.04	7.27E+12	0.0221	0	0.99	5.85E+09	3.37E+12	16.7
-238.15	3.03	7.26E+12	0.0218	0	0.99	5.85E+09	3.37E+12	16.7
-238.09	3.03	7.25E+12	0.0215	0	0.99	5.85E+09	3.36E+12	16.7
-238.03	3.02	7.24E+12	0.0212	0	0.99	5.85E+09	3.36E+12	16.7
-237.97	3.02	7.24E+12	0.0210	0	0.99	5.85E+09	3.35E+12	16.7
-237.86	3.02	7.23E+12	0.0206	0	0.99	5.84E+09	3.35E+12	16.7
-237.76	3.01	7.22E+12	0.0204	0	0.99	5.84E+09	3.34E+12	16.7
-237.65	3.01	7.22E+12	0.0202	0	0.99	5.84E+09	3.34E+12	16.7
-237.54	3.01	7.22E+12	0.0200	0	0.99	5.84E+09	3.34E+12	16.7
-237.48	3.00	7.49E+12	0.0225	0	1.00	5.88E+09	3.40E+12	16.7
-237.44	2.99	7.47E+12	0.0252	0	1.01	5.91E+09	3.45E+12	16.7
-237.39	2.98	7.44E+12	0.0264	0	1.01	5.92E+09	3.47E+12	16.6
-237.35	2.97	7.42E+12	0.0263	0	1.01	5.92E+09	3.47E+12	16.6
-237.30	2.96	7.40E+12	0.0258	0	1.01	5.92E+09	3.46E+12	16.6
-237.26	2.95	7.38E+12	0.0252	0	1.01	5.91E+09	3.45E+12	16.6
-237.20	2.94	7.37E+12	0.0247	0	1.01	5.91E+09	3.45E+12	16.6
-237.15	2.93	7.35E+12	0.0243	0	1.01	5.91E+09	3.44E+12	16.6
-237.10	2.92	7.34E+12	0.0239	0	1.01	5.91E+09	3.43E+12	16.6
-237.04	2.92	7.33E+12	0.0236	0	1.00	5.90E+09	3.43E+12	16.6
-236.96	2.91	7.32E+12	0.0232	0	1.00	5.90E+09	3.42E+12	16.6
-236.87	2.91	7.31E+12	0.0229	0	1.00	5.90E+09	3.41E+12	16.5
-236.78	2.91	7.30E+12	0.0226	0	1.00	5.90E+09	3.41E+12	16.5
-236.70	2.90	7.30E+12	0.0224	0	1.00	5.90E+09	3.41E+12	16.5
-236.56	2.90	7.29E+12	0.0222	0	1.00	5.90E+09	3.40E+12	16.5
-236.45	2.89	7.46E+12	0.0246	0	1.01	5.92E+09	3.45E+12	16.5
-236.41	2.88	7.45E+12	0.0257	0	1.01	5.94E+09	3.47E+12	16.5
-236.38	2.88	7.44E+12	0.0263	0	1.01	5.94E+09	3.49E+12	16.5
-236.35	2.87	7.42E+12	0.0263	0	1.01	5.94E+09	3.49E+12	16.5
-236.31	2.87	7.41E+12	0.0260	0	1.01	5.94E+09	3.48E+12	16.5
-236.28	2.86	7.40E+12	0.0260	0	1.01	5.94E+09	3.48E+12	16.5
-236.22	2.86	7.39E+12	0.0256	0	1.01	5.94E+09	3.48E+12	16.5
-236.16	2.85	7.38E+12	0.0252	0	1.01	5.93E+09	3.47E+12	16.5
-236.11	2.85	7.37E+12	0.0249	0	1.01	5.93E+09	3.46E+12	16.5
-236.05	2.84	7.36E+12	0.0247	0	1.01	5.93E+09	3.46E+12	16.5
-235.96	2.84	7.35E+12	0.0244	0	1.01	5.93E+09	3.46E+12	16.5
-235.88	2.83	7.35E+12	0.0242	0	1.01	5.93E+09	3.45E+12	16.4
-235.79	2.83	7.34E+12	0.0240	0	1.01	5.93E+09	3.45E+12	16.4
-235.70	2.83	7.34E+12	0.0239	0	1.01	5.93E+09	3.45E+12	16.4
-235.56	2.83	7.34E+12	0.0237	0	1.01	5.93E+09	3.45E+12	16.4
-235.51	2.83	7.34E+12	0.0237	0	1.01	5.93E+09	3.44E+12	16.4
-235.46	2.83	7.45E+12</						

-232.81	2.82	7.40E+12	0.0246	0	1.01	5.96E+09	3.48E+12	16.5
-232.65	2.82	7.40E+12	0.0247	0	1.02	5.96E+09	3.48E+12	16.5
-232.55	2.82	7.41E+12	0.0246	0	1.02	5.96E+09	3.48E+12	16.5
-232.48	2.82	7.25E+12	0.0226	0	1.01	5.94E+09	3.44E+12	16.5
-232.43	2.83	7.27E+12	0.0214	0	1.01	5.92E+09	3.41E+12	16.5
-232.37	2.84	7.28E+12	0.0209	0	1.00	5.92E+09	3.40E+12	16.5
-232.32	2.85	7.30E+12	0.0210	0	1.00	5.92E+09	3.40E+12	16.5
-232.26	2.85	7.31E+12	0.0212	0	1.01	5.92E+09	3.41E+12	16.5
-232.19	2.86	7.32E+12	0.0215	0	1.01	5.92E+09	3.42E+12	16.5
-232.12	2.86	7.33E+12	0.0218	0	1.01	5.93E+09	3.42E+12	16.5
-232.05	2.87	7.34E+12	0.0219	0	1.01	5.93E+09	3.43E+12	16.5
-231.99	2.87	7.35E+12	0.0221	0	1.01	5.93E+09	3.43E+12	16.6
-231.88	2.88	7.36E+12	0.0222	0	1.01	5.93E+09	3.43E+12	16.6
-231.77	2.88	7.36E+12	0.0223	0	1.01	5.94E+09	3.43E+12	16.6
-231.66	2.88	7.36E+12	0.0223	0	1.01	5.94E+09	3.44E+12	16.6
-231.56	2.88	7.37E+12	0.0223	0	1.01	5.94E+09	3.44E+12	16.6
-231.49	2.89	7.12E+12	0.0199	0	1.00	5.91E+09	3.38E+12	16.6
-231.45	2.90	7.14E+12	0.0179	0	0.99	5.88E+09	3.34E+12	16.6
-231.40	2.91	7.17E+12	0.0171	0	0.99	5.86E+09	3.32E+12	16.6
-231.35	2.92	7.19E+12	0.0172	0	0.99	5.87E+09	3.32E+12	16.6
-231.30	2.93	7.21E+12	0.0176	0	0.99	5.87E+09	3.33E+12	16.7
-231.26	2.94	7.22E+12	0.0179	0	0.99	5.88E+09	3.34E+12	16.7
-231.19	2.95	7.24E+12	0.0182	0	1.00	5.88E+09	3.34E+12	16.7
-231.13	2.96	7.25E+12	0.0183	0	1.00	5.89E+09	3.35E+12	16.7
-231.07	2.97	7.26E+12	0.0186	0	1.00	5.89E+09	3.35E+12	16.7
-231.01	2.97	7.27E+12	0.0187	0	1.00	5.89E+09	3.36E+12	16.7
-230.91	2.98	7.28E+12	0.0190	0	1.00	5.90E+09	3.36E+12	16.7
-230.80	2.98	7.29E+12	0.0191	0	1.00	5.90E+09	3.37E+12	16.7
-230.70	2.99	7.30E+12	0.0191	0	1.00	5.90E+09	3.37E+12	16.7
-230.60	2.99	7.30E+12	0.0192	0	1.00	5.90E+09	3.37E+12	16.7
-230.50	2.99	7.31E+12	0.0192	0	1.00	5.91E+09	3.37E+12	16.8
-230.49	3.00	7.01E+12	0.0182	0	1.00	5.89E+09	3.35E+12	16.8
-230.47	3.00	7.02E+12	0.0163	0	0.99	5.86E+09	3.30E+12	16.8
-230.46	3.00	7.02E+12	0.0156	0	0.99	5.85E+09	3.28E+12	16.8
-230.44	3.01	7.03E+12	0.0152	0	0.99	5.84E+09	3.27E+12	16.8
-230.41	3.02	7.05E+12	0.0145	0	0.98	5.82E+09	3.25E+12	16.8
-230.38	3.03	7.06E+12	0.0142	0	0.98	5.82E+09	3.24E+12	16.8
-230.35	3.04	7.08E+12	0.0142	0	0.98	5.82E+09	3.24E+12	16.8
-230.31	3.05	7.10E+12	0.0143	0	0.98	5.82E+09	3.24E+12	16.8
-230.26	3.06	7.12E+12	0.0145	0	0.98	5.82E+09	3.25E+12	16.9
-230.21	3.07	7.14E+12	0.0148	0	0.98	5.83E+09	3.26E+12	16.9
-230.15	3.08	7.16E+12	0.0150	0	0.98	5.84E+09	3.27E+12	16.9
-230.10	3.09	7.17E+12	0.0152	0	0.99	5.84E+09	3.27E+12	16.9
-230.00	3.11	7.19E+12	0.0155	0	0.99	5.85E+09	3.28E+12	16.9
-229.91	3.12	7.21E+12	0.0157	0	0.99	5.85E+09	3.29E+12	16.9
-229.81	3.12	7.22E+12	0.0159	0	0.99	5.86E+09	3.29E+12	16.9
-229.72	3.13	7.23E+12	0.0160	0	0.99	5.86E+09	3.30E+12	17.0
-229.62	3.13	7.23E+12	0.0160	0	0.99	5.86E+09	3.30E+12	17.0
-229.45	3.14	7.21E+12	0.0156	0	0.99	5.86E+09	3.29E+12	17.0
-229.27	3.15	7.22E+12	0.0154	0	0.99	5.86E+09	3.29E+12	17.0
-229.10	3.16	7.23E+12	0.0155	0	0.99	5.86E+09	3.29E+12	17.0
-228.92	3.17	7.24E+12	0.0156	0	0.99	5.87E+09	3.30E+12	17.0
-228.74	3.17	7.24E+12	0.0155	0	0.99	5.87E+09	3.30E+12	17.0
-228.55	3.17	7.25E+12	0.0154	0	0.99	5.87E+09	3.30E+12	17.0
-228.36	3.18	7.22E+12	0.0149	0	0.99	5.87E+09	3.29E+12	17.0
-228.17	3.19	7.23E+12	0.0147	0	0.99	5.87E+09	3.28E+12	17.1
-227.98	3.20	7.24E+12	0.0147	0	0.99	5.87E+09	3.28E+12	17.1
-227.79	3.20	7.24E+12	0.0148	0	0.99	5.87E+09	3.29E+12	17.1
-227.57	3.20	7.25E+12	0.0147	0	0.99	5.88E+09	3.29E+12	17.1
-227.35	3.22	7.24E+12	0.0144	0	0.99	5.88E+09	3.28E+12	17.1
-227.13	3.23	7.26E+12	0.0145	0	0.99	5.88E+09	3.29E+12	17.1
-226.91	3.25	7.28E+12	0.0146	0	0.99	5.89E+09	3.29E+12	17.2
-226.64	3.26	7.29E+12	0.0146	0	0.99	5.89E+09	3.30E+12	17.2
-226.37	3.26	7.27E+12	0.0143	0	0.99	5.89E+09	3.29E+12	17.2
-226.10	3.27	7.29E+12	0.0141	0	0.99	5.89E+09	3.29E+12	17.2
-225.82	3.28	7.29E+12	0.0141	0	0.99	5.90E+09	3.29E+12	17.2
-225.53	3.28	7.30E+12	0.0140	0	0.99	5.90E+09	3.29E+12	17.2
-225.24	3.29	7.29E+12	0.0137	0	0.99	5.90E+09	3.29E+12	17.2
-224.95	3.30	7.30E+12	0.0136	0	0.99	5.90E+09	3.29E+12	17.2
-224.66	3.30	7.30E+12	0.0135	0	0.99	5.90E+09	3.29E+12	17.3
-224.28	3.31	7.29E+12	0.0132	0	0.99	5.90E+09	3.28E+12	17.3
-223.91	3.32	7.30E+12	0.0131	0	0.99	5.90E+09	3.28E+12	17.3
-223.53	3.32	7.31E+12	0.0130	0	1.00	5.91E+09	3.28E+12	17.3
-223.15	3.33	7.29E+12	0.0127	0	0.99	5.91E+09	3.28E+12	17.3
-222.74	3.33	7.30E+12	0.0126	0	0.99	5.91E+09	3.28E+12	17.3
-222.33	3.35	7.32E+12	0.0126	0	1.00	5.92E+09	3.28E+12	17.3
-221.92	3.37	7.35E+12</						

-206.76	3.39	7.47E+12	0.0108	0	1.01	6.01E+09	3.31E+12	17.6
-206.25	3.38	7.43E+12	0.0104	0	1.01	6.00E+09	3.29E+12	17.6
-205.74	3.37	7.42E+12	0.0102	0	1.01	5.99E+09	3.29E+12	17.6
-205.23	3.38	7.38E+12	0.0098	0	1.00	5.98E+09	3.27E+12	17.6
-204.73	3.38	7.40E+12	0.0099	0	1.00	5.98E+09	3.27E+12	17.6
-204.22	3.40	7.36E+12	0.0095	0	1.00	5.97E+09	3.26E+12	17.6
-203.71	3.41	7.38E+12	0.0095	0	1.00	5.97E+09	3.26E+12	17.7
-203.51	3.41	7.39E+12	0.0096	0	1.00	5.97E+09	3.26E+12	17.7
-203.31	3.41	7.32E+12	0.0091	0	1.00	5.95E+09	3.24E+12	17.7
-203.14	3.41	7.32E+12	0.0089	0	1.00	5.95E+09	3.23E+12	17.7
-202.98	3.41	7.32E+12	0.0089	0	1.00	5.94E+09	3.23E+12	17.7
-202.81	3.41	7.32E+12	0.0089	0	1.00	5.95E+09	3.23E+12	17.7
-202.58	3.41	7.32E+12	0.0089	0	1.00	5.95E+09	3.23E+12	17.7
-202.35	3.42	7.27E+12	0.0084	0	0.99	5.93E+09	3.21E+12	17.7
-202.16	3.43	7.28E+12	0.0083	0	0.99	5.92E+09	3.20E+12	17.7
-201.98	3.44	7.29E+12	0.0084	0	0.99	5.93E+09	3.21E+12	17.7
-201.80	3.44	7.30E+12	0.0085	0	0.99	5.93E+09	3.21E+12	17.7
-201.61	3.44	7.30E+12	0.0085	0	0.99	5.93E+09	3.21E+12	17.7
-201.54	3.44	7.31E+12	0.0085	0	0.99	5.93E+09	3.21E+12	17.7
-201.52	3.44	7.31E+12	0.0085	0	0.99	5.93E+09	3.21E+12	17.7
-201.50	3.44	7.21E+12	0.0085	0	0.99	5.93E+09	3.21E+12	17.7
-201.47	3.44	7.21E+12	0.0080	0	0.99	5.91E+09	3.18E+12	17.7
-201.41	3.44	7.21E+12	0.0078	0	0.99	5.90E+09	3.18E+12	17.7
-201.36	3.44	7.22E+12	0.0077	0	0.99	5.90E+09	3.17E+12	17.7
-201.30	3.45	7.22E+12	0.0077	0	0.99	5.90E+09	3.17E+12	17.7
-201.19	3.45	7.23E+12	0.0077	0	0.99	5.90E+09	3.17E+12	17.7
-201.09	3.45	7.23E+12	0.0078	0	0.99	5.90E+09	3.17E+12	17.7
-200.98	3.45	7.23E+12	0.0078	0	0.99	5.90E+09	3.17E+12	17.8
-200.79	3.45	7.24E+12	0.0078	0	0.99	5.90E+09	3.17E+12	17.8
-200.60	3.45	7.24E+12	0.0078	0	0.99	5.90E+09	3.18E+12	17.8
-200.53	3.45	7.24E+12	0.0078	0	0.99	5.90E+09	3.18E+12	17.8
-200.51	3.45	7.24E+12	0.0078	0	0.99	5.90E+09	3.18E+12	17.8
-200.49	3.45	7.14E+12	0.0078	0	0.99	5.90E+09	3.18E+12	17.8
-200.46	3.46	7.15E+12	0.0073	0	0.98	5.88E+09	3.15E+12	17.8
-200.41	3.46	7.16E+12	0.0072	0	0.98	5.88E+09	3.14E+12	17.8
-200.35	3.47	7.17E+12	0.0072	0	0.98	5.87E+09	3.14E+12	17.8
-200.30	3.47	7.17E+12	0.0072	0	0.98	5.87E+09	3.14E+12	17.8
-200.19	3.48	7.18E+12	0.0072	0	0.98	5.88E+09	3.14E+12	17.8
-200.08	3.48	7.19E+12	0.0073	0	0.98	5.88E+09	3.15E+12	17.8
-199.98	3.49	7.20E+12	0.0073	0	0.98	5.88E+09	3.15E+12	17.8
-199.78	3.49	7.21E+12	0.0074	0	0.99	5.89E+09	3.15E+12	17.8
-199.59	3.50	7.21E+12	0.0074	0	0.99	5.89E+09	3.15E+12	17.8
-199.52	3.50	7.21E+12	0.0074	0	0.99	5.89E+09	3.15E+12	17.8
-199.50	3.50	7.12E+12	0.0072	0	0.98	5.88E+09	3.14E+12	17.8
-199.48	3.50	7.12E+12	0.0069	0	0.98	5.87E+09	3.13E+12	17.8
-199.45	3.50	7.13E+12	0.0069	0	0.98	5.86E+09	3.12E+12	17.8
-199.39	3.51	7.14E+12	0.0068	0	0.98	5.86E+09	3.12E+12	17.8
-199.33	3.52	7.15E+12	0.0068	0	0.98	5.86E+09	3.12E+12	17.9
-199.27	3.52	7.15E+12	0.0068	0	0.98	5.86E+09	3.12E+12	17.9
-199.22	3.52	7.16E+12	0.0068	0	0.98	5.86E+09	3.12E+12	17.9
-199.09	3.53	7.17E+12	0.0069	0	0.98	5.87E+09	3.13E+12	17.9
-198.97	3.54	7.18E+12	0.0070	0	0.98	5.87E+09	3.13E+12	17.9
-198.84	3.54	7.19E+12	0.0070	0	0.98	5.87E+09	3.13E+12	17.9
-198.72	3.54	7.19E+12	0.0070	0	0.98	5.87E+09	3.13E+12	17.9
-198.56	3.54	7.19E+12	0.0070	0	0.98	5.87E+09	3.14E+12	17.9
-198.50	3.54	7.20E+12	0.0070	0	0.98	5.87E+09	3.14E+12	17.9
-198.46	3.55	7.10E+12	0.0067	0	0.98	5.86E+09	3.12E+12	17.9
-198.42	3.55	7.11E+12	0.0065	0	0.98	5.85E+09	3.10E+12	17.9
-198.38	3.56	7.12E+12	0.0065	0	0.98	5.84E+09	3.10E+12	17.9
-198.31	3.56	7.13E+12	0.0064	0	0.98	5.84E+09	3.10E+12	17.9
-198.24	3.57	7.14E+12	0.0065	0	0.98	5.84E+09	3.10E+12	17.9
-198.18	3.58	7.14E+12	0.0065	0	0.98	5.85E+09	3.10E+12	17.9
-198.11	3.58	7.15E+12	0.0066	0	0.98	5.85E+09	3.11E+12	17.9
-197.94	3.59	7.16E+12	0.0066	0	0.98	5.85E+09	3.11E+12	18.0
-197.76	3.59	7.17E+12	0.0066	0	0.98	5.86E+09	3.11E+12	18.0
-197.59	3.60	7.17E+12	0.0067	0	0.98	5.86E+09	3.12E+12	18.0
-197.41	3.61	7.09E+12	0.0062	0	0.98	5.84E+09	3.09E+12	18.0
-197.28	3.62	7.11E+12	0.0061	0	0.98	5.83E+09	3.08E+12	18.0
-197.14	3.63	7.13E+12	0.0060	0	0.97	5.83E+09	3.08E+12	18.0
-197.01	3.64	7.14E+12	0.0062	0	0.98	5.84E+09	3.09E+12	18.0
-196.84	3.64	7.14E+12	0.0062	0	0.98	5.84E+09	3.09E+12	18.0
-196.67	3.65	7.15E+12	0.0063	0	0.98	5.85E+09	3.09E+12	18.0
-196.50	3.65	7.16E+12	0.0063	0	0.98	5.85E+09	3.10E+12	18.1
-196.47	3.65	7.05E+12	0.0060	0	0.98	5.83E+09	3.08E+12	18.1
-196.45	3.66	7.05E+12	0.0058	0	0.97	5.82E+09	3.06E+12	18.1
-196.42	3.66	7.06E+12	0.0057	0	0.97	5.81E+09	3.06E+12	18.1
-196.37	3.67	7.07E+12</						

-194.33	3.82	6.97E+12	0.0048	0	0.96	5.77E+09	3.00E+12	18.3
-194.24	3.83	6.98E+12	0.0046	0	0.96	5.76E+09	2.98E+12	18.3
-194.16	3.84	6.99E+12	0.0046	0	0.96	5.76E+09	2.98E+12	18.3
-194.08	3.85	7.00E+12	0.0047	0	0.96	5.76E+09	2.99E+12	18.3
-193.99	3.85	7.00E+12	0.0047	0	0.96	5.76E+09	2.99E+12	18.3
-193.91	3.86	7.01E+12	0.0047	0	0.96	5.77E+09	2.99E+12	18.3
-193.78	3.86	7.02E+12	0.0047	0	0.96	5.77E+09	2.99E+12	18.3
-193.64	3.87	7.02E+12	0.0047	0	0.96	5.77E+09	3.00E+12	18.3
-193.50	3.87	7.03E+12	0.0047	0	0.96	5.77E+09	3.00E+12	18.3
-193.39	3.88	6.90E+12	0.0043	0	0.96	5.74E+09	2.96E+12	18.4
-193.30	3.90	6.92E+12	0.0042	0	0.96	5.73E+09	2.95E+12	18.4
-193.20	3.91	6.94E+12	0.0042	0	0.96	5.73E+09	2.95E+12	18.4
-193.11	3.92	6.95E+12	0.0042	0	0.96	5.73E+09	2.95E+12	18.4
-192.98	3.93	6.97E+12	0.0043	0	0.96	5.74E+09	2.96E+12	18.4
-192.84	3.95	6.98E+12	0.0043	0	0.96	5.74E+09	2.96E+12	18.4
-192.71	3.95	6.99E+12	0.0043	0	0.96	5.75E+09	2.97E+12	18.4
-192.55	3.96	6.99E+12	0.0043	0	0.96	5.75E+09	2.97E+12	18.5
-192.51	3.96	7.00E+12	0.0043	0	0.96	5.75E+09	2.97E+12	18.5
-192.49	3.96	6.87E+12	0.0042	0	0.96	5.74E+09	2.96E+12	18.5
-192.47	3.96	6.87E+12	0.0041	0	0.96	5.73E+09	2.94E+12	18.5
-192.46	3.97	6.88E+12	0.0040	0	0.95	5.72E+09	2.93E+12	18.5
-192.42	3.97	6.88E+12	0.0039	0	0.95	5.71E+09	2.93E+12	18.5
-192.39	3.98	6.89E+12	0.0039	0	0.95	5.71E+09	2.92E+12	18.5
-192.36	3.99	6.90E+12	0.0038	0	0.95	5.71E+09	2.92E+12	18.5
-192.28	4.00	6.91E+12	0.0039	0	0.95	5.71E+09	2.92E+12	18.5
-192.21	4.01	6.92E+12	0.0039	0	0.95	5.71E+09	2.93E+12	18.5
-192.14	4.01	6.93E+12	0.0039	0	0.95	5.72E+09	2.93E+12	18.5
-191.99	4.03	6.95E+12	0.0040	0	0.96	5.72E+09	2.94E+12	18.5
-191.84	4.04	6.96E+12	0.0040	0	0.96	5.73E+09	2.94E+12	18.6
-191.69	4.05	6.97E+12	0.0040	0	0.96	5.73E+09	2.94E+12	18.6
-191.54	4.05	6.98E+12	0.0040	0	0.96	5.74E+09	2.95E+12	18.6
-191.43	4.07	6.86E+12	0.0037	0	0.95	5.71E+09	2.91E+12	18.6
-191.33	4.08	6.88E+12	0.0036	0	0.95	5.70E+09	2.90E+12	18.6
-191.23	4.10	6.89E+12	0.0036	0	0.95	5.70E+09	2.90E+12	18.6
-191.13	4.11	6.91E+12	0.0036	0	0.95	5.70E+09	2.90E+12	18.6
-190.98	4.12	6.92E+12	0.0036	0	0.95	5.71E+09	2.91E+12	18.7
-190.82	4.13	6.94E+12	0.0037	0	0.95	5.71E+09	2.91E+12	18.7
-190.67	4.14	6.95E+12	0.0037	0	0.95	5.72E+09	2.92E+12	18.7
-190.53	4.15	6.95E+12	0.0037	0	0.95	5.72E+09	2.92E+12	18.7
-190.51	4.15	6.95E+12	0.0037	0	0.95	5.72E+09	2.92E+12	18.7
-190.50	4.15	6.95E+12	0.0037	0	0.95	5.72E+09	2.92E+12	18.7
-190.49	4.15	6.70E+12	0.0037	0	0.95	5.72E+09	2.92E+12	18.7
-190.48	4.16	6.70E+12	0.0034	0	0.95	5.69E+09	2.88E+12	18.7
-190.46	4.16	6.71E+12	0.0031	0	0.94	5.66E+09	2.86E+12	18.7
-190.43	4.17	6.72E+12	0.0030	0	0.94	5.64E+09	2.84E+12	18.7
-190.40	4.18	6.73E+12	0.0029	0	0.94	5.63E+09	2.82E+12	18.7
-190.36	4.20	6.75E+12	0.0029	0	0.94	5.63E+09	2.82E+12	18.7
-190.32	4.21	6.76E+12	0.0029	0	0.94	5.63E+09	2.83E+12	18.8
-190.28	4.22	6.77E+12	0.0029	0	0.94	5.63E+09	2.83E+12	18.8
-190.24	4.23	6.79E+12	0.0029	0	0.94	5.64E+09	2.83E+12	18.8
-190.16	4.25	6.81E+12	0.0030	0	0.94	5.64E+09	2.84E+12	18.8
-190.07	4.27	6.83E+12	0.0031	0	0.94	5.65E+09	2.85E+12	18.8
-189.98	4.29	6.84E+12	0.0031	0	0.94	5.66E+09	2.85E+12	18.8
-189.90	4.30	6.86E+12	0.0031	0	0.94	5.66E+09	2.86E+12	18.8
-189.71	4.32	6.88E+12	0.0032	0	0.95	5.67E+09	2.86E+12	18.9
-189.53	4.34	6.89E+12	0.0032	0	0.95	5.68E+09	2.87E+12	18.9
-189.35	4.35	6.86E+12	0.0032	0	0.95	5.68E+09	2.87E+12	18.9
-189.17	4.39	6.91E+12	0.0031	0	0.95	5.68E+09	2.87E+12	18.9
-188.95	4.41	6.93E+12	0.0032	0	0.95	5.69E+09	2.88E+12	19.0
-188.72	4.42	6.94E+12	0.0032	0	0.95	5.69E+09	2.88E+12	19.0
-188.50	4.42	6.99E+12	0.0033	0	0.95	5.71E+09	2.90E+12	19.0
-188.27	4.42	6.99E+12	0.0033	0	0.95	5.72E+09	2.90E+12	19.0
-188.05	4.42	6.99E+12	0.0033	0	0.95	5.72E+09	2.90E+12	19.0
-187.77	4.42	6.99E+12	0.0032	0	0.95	5.72E+09	2.90E+12	19.0
-187.56	4.42	6.99E+12	0.0032	0	0.95	5.72E+09	2.90E+12	19.0
-187.48	4.42	7.05E+12	0.0033	0	0.96	5.74E+09	2.92E+12	19.0
-187.41	4.42	7.06E+12	0.0035	0	0.96	5.75E+09	2.93E+12	19.0
-187.33	4.42	7.06E+12	0.0035	0	0.96	5.75E+09	2.93E+12	19.0
-187.20	4.42	7.05E+12	0.0034	0	0.96	5.75E+09	2.93E+12	19.0
-187.08	4.42	7.05E+12	0.0034	0	0.96	5.75E+09	2.92E+12	19.0
-186.95	4.42	7.06E+12	0.0034	0	0.96	5.75E+09	2.93E+12	19.0
-186.83	4.42	7.06E+12	0.0034	0	0.96	5.75E+09	2.93E+12	19.0
-186.50	4.41	7.12E+12	0.0035	0	0.96	5.78E+09	2.95E+12	19.0
-186.24	4.39	7.10E+12	0.0035	0	0.96	5.78E+09	2.95E+12	19.0
-185.99	4.37	7.08E+12	0.0033	0	0.96	5.77E+09	2.94E+12	19.0
-185.73	4.37	7.08E+12	0.0033	0	0.96	5.77E+09	2.93E+12	19.0
-185.48	4.37	7.17E+12</						

-182.48	4.22	7.35E+12	0.0041	0	0.98	5.89E+09	3.05E+12	18.9
-182.44	4.22	7.35E+12	0.0043	0	0.99	5.90E+09	3.06E+12	18.9
-182.41	4.21	7.34E+12	0.0043	0	0.99	5.91E+09	3.07E+12	18.9
-182.34	4.21	7.33E+12	0.0043	0	0.99	5.91E+09	3.07E+12	18.9
-182.27	4.20	7.32E+12	0.0043	0	0.99	5.91E+09	3.07E+12	18.8
-182.21	4.19	7.32E+12	0.0042	0	0.98	5.90E+09	3.06E+12	18.8
-182.14	4.19	7.31E+12	0.0042	0	0.98	5.90E+09	3.06E+12	18.8
-181.97	4.17	7.30E+12	0.0041	0	0.98	5.90E+09	3.06E+12	18.8
-181.93	4.17	7.30E+12	0.0041	0	0.98	5.90E+09	3.06E+12	18.8
-181.88	4.17	7.29E+12	0.0041	0	0.98	5.90E+09	3.05E+12	18.8
-181.87	4.17	7.29E+12	0.0041	0	0.98	5.90E+09	3.05E+12	18.8
-181.87	4.17	7.29E+12	0.0041	0	0.98	5.90E+09	3.05E+12	18.8
-181.87	4.18	7.30E+12	0.0041	3.60E+13	0.98	5.90E+09	3.05E+12	18.8
-181.87	4.20	7.33E+12	0.0041	3.60E+13	0.98	5.90E+09	3.05E+12	18.8
-181.87	4.21	7.34E+12	0.0041	3.60E+13	0.98	5.90E+09	3.05E+12	18.9
-181.87	4.24	7.38E+12	0.0041	3.60E+13	0.98	5.90E+09	3.05E+12	18.9
-181.87	4.27	7.41E+12	0.0041	3.60E+13	0.98	5.90E+09	3.06E+12	18.9
-181.87	4.30	7.45E+12	0.0041	3.60E+13	0.98	5.90E+09	3.06E+12	19.0
-181.86	4.48	7.65E+12	0.0042	3.60E+13	0.99	5.90E+09	3.06E+12	19.1
-181.86	4.65	7.84E+12	0.0043	3.60E+13	0.99	5.91E+09	3.07E+12	19.3
-181.86	4.83	8.03E+12	0.0045	3.60E+13	0.99	5.93E+09	3.09E+12	19.5
-181.85	5.02	8.21E+12	0.0047	3.60E+13	0.99	5.94E+09	3.11E+12	19.6
-181.84	5.57	8.73E+12	0.0056	3.60E+13	1.00	6.01E+09	3.19E+12	20.1
-181.83	6.14	9.21E+12	0.0070	3.60E+13	1.02	6.09E+09	3.28E+12	20.5
-181.82	6.72	9.66E+12	0.0091	3.60E+13	1.04	6.19E+09	3.40E+12	20.9
-181.81	7.32	1.01E+13	0.0120	3.60E+13	1.06	6.28E+09	3.52E+12	21.3
-181.80	7.93	1.05E+13	0.0159	3.60E+13	1.08	6.37E+09	3.65E+12	21.6
-181.78	8.74	1.09E+13	0.0228	3.60E+13	1.10	6.47E+09	3.82E+12	22.0
-181.77	9.56	1.13E+13	0.0323	3.60E+13	1.13	6.55E+09	3.99E+12	22.4
-181.75	10.40	1.17E+13	0.0453	3.60E+13	1.15	6.60E+09	4.16E+12	22.8
-181.75	10.57	1.18E+13	0.0484	3.60E+13	1.15	6.61E+09	4.19E+12	22.8
-181.75	10.65	1.18E+13	0.0498	3.60E+13	1.16	6.61E+09	4.21E+12	22.9
-181.75	10.65	1.18E+13	0.0499	3.60E+13	1.16	6.61E+09	4.21E+12	22.9
-181.75	10.65	1.18E+13	0.0500	3.60E+13	1.16	6.61E+09	4.21E+12	22.9
-181.75	10.66	1.19E+13	0.0500	3.60E+13	1.16	6.61E+09	4.21E+12	22.9
-181.75	10.66	1.19E+13	0.0501	3.60E+13	1.16	6.61E+09	4.21E+12	22.9
-181.75	10.66	1.19E+13	0.0501	3.60E+13	1.16	6.61E+09	4.21E+12	22.9
-181.75	10.66	1.19E+13	0.0502	3.60E+13	1.16	6.61E+09	4.21E+12	22.9
-181.75	10.67	1.19E+13	0.0503	3.60E+13	1.16	6.61E+09	4.21E+12	22.9
-181.75	10.67	1.19E+13	0.0504	3.60E+13	1.16	6.61E+09	4.22E+12	22.9
-181.75	10.68	1.19E+13	0.0505	3.60E+13	1.16	6.61E+09	4.22E+12	22.9
-181.75	10.71	1.19E+13	0.0511	3.60E+13	1.16	6.61E+09	4.22E+12	22.9
-181.75	10.75	1.19E+13	0.0518	3.60E+13	1.16	6.61E+09	4.23E+12	22.9
-181.75	10.78	1.19E+13	0.0525	3.60E+13	1.16	6.61E+09	4.24E+12	22.9
-181.75	10.81	1.19E+13	0.0531	3.60E+13	1.16	6.61E+09	4.24E+12	22.9
-181.74	11.13	1.20E+13	0.0598	3.60E+13	1.17	6.62E+09	4.30E+12	23.1
-181.74	11.45	1.22E+13	0.0672	3.60E+13	1.18	6.61E+09	4.37E+12	23.2
-181.73	11.76	1.23E+13	0.0755	3.60E+13	1.19	6.60E+09	4.43E+12	23.3
-181.73	12.09	1.24E+13	0.0847	3.60E+13	1.19	6.58E+09	4.49E+12	23.4
-181.73	12.24	1.25E+13	0.0894	3.60E+13	1.20	6.57E+09	4.52E+12	23.5
-181.72	12.28	1.25E+13	0.0907	3.60E+13	1.20	6.56E+09	4.53E+12	23.5
-181.72	12.30	1.25E+13	0.0912	3.60E+13	1.20	6.56E+09	4.53E+12	23.5
-181.72	12.31	1.25E+13	0.0917	0	1.20	6.56E+09	4.53E+12	23.5
-181.72	12.29	1.25E+13	0.0921	0	1.20	6.56E+09	4.54E+12	23.5
-181.72	12.29	1.25E+13	0.0926	0	1.20	6.56E+09	4.54E+12	23.5
-181.72	12.29	1.25E+13	0.0931	0	1.20	6.56E+09	4.54E+12	23.5
-181.72	12.29	1.25E+13	0.0937	0	1.20	6.56E+09	4.55E+12	23.5
-181.72	12.29	1.25E+13	0.0944	0	1.20	6.55E+09	4.55E+12	23.5
-181.72	12.28	1.25E+13	0.0950	0	1.20	6.55E+09	4.55E+12	23.5
-181.72	12.27	1.25E+13	0.0956	0	1.20	6.55E+09	4.56E+12	23.5
-181.72	12.27	1.25E+13	0.0963	0	1.20	6.55E+09	4.56E+12	23.5
-181.72	12.25	1.25E+13	0.0989	0	1.21	6.54E+09	4.58E+12	23.5
-181.72	12.23	1.25E+13	0.1016	0	1.21	6.53E+09	4.59E+12	23.5
-181.72	12.22	1.25E+13	0.1043	0	1.21	6.52E+09	4.61E+12	23.5
-181.72	12.20	1.25E+13	0.1070	0	1.21	6.51E+09	4.62E+12	23.5
-181.71	12.08	1.24E+13	0.1251	0	1.22	6.44E+09	4.71E+12	23.4
-181.70	11.96	1.24E+13	0.1436	0	1.24	6.36E+09	4.80E+12	23.4
-181.69	11.84	1.24E+13	0.1624	0	1.25	6.28E+09	4.87E+12	23.3
-181.68	11.72	1.23E+13	0.1814	0	1.25	6.18E+09	4.95E+12	23.3
-181.67	11.50	1.23E+13	0.2184	0	1.27	5.98E+09	5.07E+12	23.2
-181.65	11.32	1.22E+13	0.2497	0	1.28	5.79E+09	5.17E+12	23.1
-181.65	11.28	1.22E+13	0.2565	0	1.29	5.75E+09	5.19E+12	23.1
-181.65	11.26	1.22E+13	0.2605	0	1.29	5.73E+09	5.20E+12	23.1

-181.54	9.41	1.16E+13	0.7328	0	1.44	2.32E+09	6.45E+12	22.3
-181.52	9.23	1.15E+13	0.7991	0	1.47	1.78E+09	6.68E+12	22.3
-181.52	9.09	1.15E+13	0.8451	0	1.50	1.39E+09	6.88E+12	22.2
-181.51	8.95	1.14E+13	0.8827	0	1.52	1.07E+09	7.09E+12	22.1
-181.50	8.80	1.14E+13	0.9121	0	1.54	8.16E+08	7.31E+12	22.1
-181.49	8.65	1.14E+13	0.9339	0	1.57	6.24E+08	7.51E+12	22.0
-181.48	8.51	1.13E+13	0.9493	0	1.59	4.85E+08	7.71E+12	21.9
-181.47	8.31	1.12E+13	0.9631	0	1.62	3.59E+08	7.94E+12	21.8
-181.46	8.11	1.10E+13	0.9712	0	1.64	2.84E+08	8.12E+12	21.7
-181.44	7.91	1.09E+13	0.9759	0	1.65	2.40E+08	8.26E+12	21.6
-181.43	7.71	1.07E+13	0.9786	0	1.67	2.15E+08	8.36E+12	21.5
-181.42	7.52	1.06E+13	0.9798	0	1.68	2.04E+08	8.42E+12	21.4
-181.40	7.25	1.04E+13	0.9798	0	1.68	2.05E+08	8.45E+12	21.2
-181.38	6.99	1.01E+13	0.9779	0	1.68	2.24E+08	8.41E+12	21.1
-181.36	6.75	9.88E+12	0.9741	0	1.68	2.62E+08	8.33E+12	20.9
-181.35	6.52	9.65E+12	0.9679	0	1.67	3.23E+08	8.20E+12	20.8
-181.33	6.31	9.42E+12	0.9581	0	1.66	4.18E+08	8.05E+12	20.6
-181.29	5.89	8.93E+12	0.9086	0	1.62	8.89E+08	7.57E+12	20.3
-181.27	5.78	8.80E+12	0.8795	0	1.60	1.16E+09	7.39E+12	20.2
-181.26	5.68	8.67E+12	0.8356	0	1.58	1.56E+09	7.18E+12	20.2
-181.25	5.59	8.55E+12	0.7659	0	1.55	2.19E+09	6.93E+12	20.1
-181.24	5.52	8.46E+12	0.6810	0	1.53	2.93E+09	6.69E+12	20.0
-181.23	5.47	8.39E+12	0.5803	0	1.50	3.79E+09	6.44E+12	20.0
-181.22	5.42	8.33E+12	0.4494	0	1.47	4.86E+09	6.15E+12	20.0
-181.22	5.38	8.28E+12	0.3050	0	1.43	5.96E+09	5.81E+12	19.9
-181.21	5.34	8.23E+12	0.1818	0	1.38	6.80E+09	5.45E+12	19.9
-181.20	5.30	8.19E+12	0.1018	0	1.34	7.23E+09	5.10E+12	19.9
-181.20	5.28	8.16E+12	0.0666	0	1.31	7.34E+09	4.87E+12	19.9
-181.19	5.26	8.13E+12	0.0444	0	1.28	7.35E+09	4.66E+12	19.8
-181.18	5.25	8.11E+12	0.0306	0	1.25	7.31E+09	4.48E+12	19.8
-181.18	5.23	8.09E+12	0.0218	0	1.23	7.24E+09	4.31E+12	19.8
-181.17	5.21	8.07E+12	0.0144	0	1.20	7.13E+09	4.12E+12	19.8
-181.16	5.19	8.04E+12	0.0102	0	1.18	7.02E+09	3.96E+12	19.8
-181.15	5.18	8.02E+12	0.0076	0	1.16	6.92E+09	3.83E+12	19.8
-181.15	5.16	8.01E+12	0.0059	0	1.14	6.83E+09	3.72E+12	19.8
-181.14	5.15	7.99E+12	0.0048	0	1.13	6.76E+09	3.63E+12	19.7
-181.12	5.13	7.96E+12	0.0034	0	1.11	6.63E+09	3.48E+12	19.7
-181.10	5.11	7.94E+12	0.0026	0	1.09	6.53E+09	3.38E+12	19.7
-181.09	5.09	7.92E+12	0.0022	0	1.08	6.46E+09	3.30E+12	19.7
-181.07	5.08	7.90E+12	0.0019	0	1.07	6.41E+09	3.25E+12	19.7
-181.05	5.06	7.89E+12	0.0018	0	1.06	6.38E+09	3.21E+12	19.7
-181.02	5.04	7.87E+12	0.0016	0	1.05	6.34E+09	3.17E+12	19.7
-180.99	5.03	7.84E+12	0.0015	0	1.05	6.30E+09	3.14E+12	19.6
-180.96	5.01	7.83E+12	0.0014	0	1.05	6.28E+09	3.12E+12	19.6
-180.93	4.99	7.81E+12	0.0014	0	1.04	6.28E+09	3.11E+12	19.6
-180.90	4.98	7.80E+12	0.0014	0	1.04	6.27E+09	3.11E+12	19.6
-180.83	4.96	7.77E+12	0.0013	0	1.04	6.26E+09	3.10E+12	19.6
-180.77	4.94	7.75E+12	0.0013	0	1.04	6.25E+09	3.09E+12	19.6
-180.70	4.92	7.73E+12	0.0013	0	1.04	6.24E+09	3.08E+12	19.5
-180.64	4.90	7.71E+12	0.0013	0	1.04	6.23E+09	3.07E+12	19.5
-180.57	4.89	7.70E+12	0.0013	0	1.04	6.22E+09	3.07E+12	19.5
-180.45	4.86	7.71E+12	0.0013	0	1.04	6.22E+09	3.07E+12	19.5
-180.32	4.83	7.69E+12	0.0013	0	1.04	6.22E+09	3.07E+12	19.5
-180.20	4.81	7.67E+12	0.0013	0	1.03	6.21E+09	3.07E+12	19.5
-180.08	4.79	7.65E+12	0.0013	0	1.03	6.20E+09	3.06E+12	19.4
-179.95	4.78	7.64E+12	0.0013	0	1.03	6.20E+09	3.06E+12	19.4
-179.78	4.76	7.63E+12	0.0014	0	1.03	6.19E+09	3.06E+12	19.4
-179.61	4.75	7.62E+12	0.0014	0	1.03	6.18E+09	3.06E+12	19.4
-179.44	4.74	7.64E+12	0.0014	0	1.03	6.18E+09	3.06E+12	19.4
-179.27	4.73	7.64E+12	0.0015	0	1.03	6.19E+09	3.07E+12	19.4
-179.10	4.73	7.65E+12	0.0015	0	1.03	6.18E+09	3.07E+12	19.4
-179.00	4.72	7.65E+12	0.0015	0	1.03	6.18E+09	3.07E+12	19.4

**Table S11: Response timescales.**

	Time relative LIP-CO <sub>2</sub> input		
Changing quantity/flux	onset of initial increase	maximum value/inflection point	complete return to pre perturbation value
Atmospheric CO <sub>2</sub>	n/a	146 kyr after initial input, immediately after final input	~2 Myrs
Silicate weathering	Instantaneous/one model time step	Concurrent with end of input	~2 Myrs
Ocean anoxic fraction	Incremental increase within 18 kyrs of first CO <sub>2</sub> input	Maximum value at 323 kys after last input, 487 kyrs after first	Falls below $f_{\text{anox}} = 0.01$ by ~ 570 kyrs after final input
Fe-adsorbed phosphate burial	Initial transient increase instantaneous with first input, subsequent decrease due to increasing anoxia within 133 kyrs of first input	Falls to below one order of magnitude of its pre-perturbation value within 226 kyrs of final input	~515 kyrs after final input
Marine organic carbon burial	Incremental increase within one model timestep of first input	469 kyrs after final input	Approximately 800 kyrs after final input
Marine phosphate reservoir	Incremental increase within one model timestep of first input	469kyrs after final input	